



TECHNISCHE
UNIVERSITÄT
WIEN

VIENNA
UNIVERSITY OF
TECHNOLOGY

DISSERTATION

On Visualization and Reconstruction from Non-uniform Point Sets

ausgeführt zum Zwecke der Erlangung des akademischen Grades eines
Doktors der technischen Wissenschaften unter der Leitung von

Ao.Univ.Prof. Dipl.-Ing. Dr.techn. Eduard Gröller
Institut für Computergraphik und Algorithmen
Abteilung für Computergraphik

eingereicht an der
Technischen Universität Wien,
bei der Fakultät für Informatik

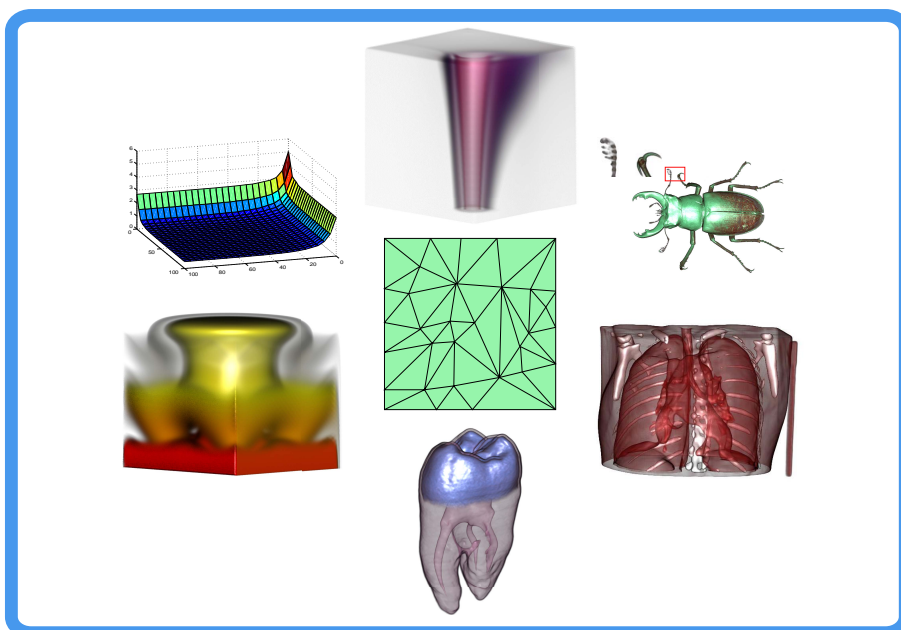
von

M.Sc. Erald Vuçini
Matrikelnummer 0728618
Metternichgasse 7/10
1030 Wien
Österreich

Wien, im Oktober 2009

On Visualization and Reconstruction from Non-uniform Point Sets

DISSERTATION



Erald VUÇINI

supervised by

Meister Eduard Gröller
Vienna University of Technology

and

Torsten Möller
Simon Fraser University

ABSTRACT

Technological and research advances in both acquisition and simulation devices provide continuously increasing high-resolution volumetric data that by far exceed today's graphical and display capabilities. Non-uniform representations offer a way of balancing this deluge of data by adaptively measuring (sampling) according to the importance (variance) of the data. Also, in many real-life situations the data are known only on a non-uniform representation.

Processing of non-uniform data is a non-trivial task and hence more difficult when compared to processing of regular data. Transforming from non-uniform to uniform representations is a well-accepted paradigm in the signal processing community. In this thesis we advocate such a concept. The main motivation for adopting this paradigm is that most of the techniques and methods related to signal processing, data mining and data exploration are well-defined and stable for Cartesian data, but generally are non-trivial to apply to non-uniform data. Among other things, this will allow us to better exploit the capabilities of modern GPUs.

In non-uniform representations sampling rates can vary drastically even by several orders of magnitude, making the decision on a target resolution a non-trivial trade-off between accuracy and efficiency. In several cases the points are spread non-uniformly with similar density across the volume, while in other cases the points have an enormous variance in distribution. In this thesis we present solutions to both cases. For the first case we suggest computing reconstructions of the same volume in different resolutions based on the level of detail we are interested in. The second case scenario is the main motivation for proposing a multi-resolution scheme, where the scale of reconstruction is decided adaptively based on the number of points in each subregion of the whole volume.

We introduce a novel framework for 3D reconstruction and visualization from non-uniform scalar and vector data. We adopt a variational reconstruction approach. In this method non-uniform point sets are transformed to a uniform representation consisting of B-spline coefficients that are attached to the grid. With these coefficients we can define a C^2 continuous function across the whole volume. Several testings were performed in order to analyze and fine-tune our framework. All the testings and the results of this thesis offer a view from a new and different perspective to the visualization and reconstruction from non-uniform point sets.

KURZFASSUNG

Der ständige Fortschritt in Forschung und Technik bei der Erfassung und der Simulation von Vorgängen führt zu immer größeren hochaufgelösten volumetrischen Daten. Die enormen Datenmengen übersteigen bei weitem die Kapazitäten heutiger Graphikkarten und Bildschirme. Die ungleichförmige Verteilung der Information in den Daten bietet eine Möglichkeit, die Datenmenge zu reduzieren. Durch adaptives Messen der Daten werden Bereiche mit hoher Wichtigkeit (Varianz) genauer gemessen und repräsentiert.

Im Vergleich zu regelmäßig repräsentierten Daten ist die Verarbeitung von unregelmäßigen Daten sehr viel aufwendiger. In der Signalverarbeitung ist aus diesem Grund die Transformation von unregelmäßigen zu regelmäßigen Daten ein häufig verwendetes Modell. In dieser Arbeit wird dieses Konzept ebenfalls verwendet. Der Hauptgrund für die Verwendung dieses Ansatzes ist die Anwendbarkeit von vorhandenen Techniken und Methoden der Signalverarbeitung, des Data-Minings und der Datenexploration für regelmäßige Daten. Diese Methoden sind für cartesische Daten wohldefiniert und stabil. Für unregelmäßige Daten ist die Anwendung dieser Techniken und Methoden hingegen nicht trivial.

In unregelmäßigen Daten kann die Datendichte in unterschiedlichen Regionen stark variieren. Dies erschwert, eine geeignete Auflösung für die Rekonstruktion in regelmäßige Daten festzulegen, welche einen Ausgleich zwischen Genauigkeit und Effizienz herstellt. In der Arbeit wird prinzipiell zwischen zwei Arten der Verteilung in unregelmäßigen Daten unterschieden: eine gleichförmige Verteilung der Daten und eine Verteilung mit starken Konzentrationen von Daten in kleinen Teilbereichen des Datenraums. Für die erste Art der Verteilung wird in der Arbeit eine Rekonstruktion in verschiedenen Auflösungen vorgeschlagen, die auf dem gewünschten Detailgrad basieren. Die zweite Art der Verteilung wird mit Hilfe eines adaptiven Auflösungschemas behandelt. Die genaue Auflösung der Rekonstruktion wird dabei adaptiv in Abhängigkeit der Datendichte in jeder Region des Datenraums bestimmt.

Des Weiteren stellt die Arbeit ein komplettes System zur drei-dimensionalen Rekonstruktion und Visualisierung unregelmäßigen Skalar- und Vektordaten vor. Dabei wird ein Rekonstruktionsansatz mittels Variantenrechnung angewendet. Mit dieser Methode werden unregelmäßige Daten in regelmäßige Daten umgewandelt indem Koeffizienten einer B-Spline-Repräsentation in einer Gitterstruktur gespeichert werden. Mit diesen Koeffizienten ist es möglich, eine C^2 stetige Funktion über das gesamte Volumen zu definieren. Für die Analyse und Feinabstimmung des vorgestellten Systems wurde auch eine Reihe von Tests durchgeführt. All diese Tests und die Resultate der Arbeit bieten einen neuartigen Blickwinkel auf die Visualisierung und Rekonstruktion von unregelmäßigen Datensätzen.

CONTENTS

Abstract	iii
Kurzfassung	v
Contents	viii
Preface	ix
1 Introduction	3
1.1 Data Representations	4
1.2 Non-uniform Data Encoding and Visualization Techniques . . .	5
1.3 Datasets	9
1.4 Evaluation Metrics	12
1.5 Thesis Scope and Outline	12
2 Variational Reconstruction	17
2.1 Sampling and Reconstruction	19
2.2 B-splines	20
2.3 Variational Reconstruction: Theory	21
2.4 Block-based Reconstruction	24
2.5 Results	26
3 Single-Resolution Reconstruction	35
3.1 Resolution Selection	37
3.2 Improving Regularization	37
3.3 Results	38

4 Multi-Resolution Reconstruction	53
4.1 Bottom-up Multi-resolution Pyramid	54
4.2 Adaptive Multi-resolution Reconstruction	55
4.3 Results	56
5 Vector Reconstruction	65
5.1 Problem Formulation and Metrics	66
5.2 Component-wise Reconstruction	66
6 Optimal Threshold	79
6.1 Thresholding the Laplacian	79
6.2 Iterative Point Selection	83
7 Summary and Conclusions	87
Bibliography	89
Curriculum Vitae	101

The reasonable man adapts himself to the world, while the unreasonable one persists in trying to adapt the world to himself. Therefore, all progress depends on the unreasonable man.

George Bernard Shaw

PREFACE

Completing a PhD degree is a difficult but rewarding experience which leaves a mark in the path of one's life. I am thankful to many people who made this path much easier and enjoyable. I was lucky to have two unique supervisors, Meister Eduard Gröller and Torsten Möller, during these years of research. With their continuous support and guidance my PhD experience was very colourful. I want to thank the head of our institute, Werner Purgathofer, for helping me in so many situations and for letting me win so many times in Darts.

I want to thank my colleagues of the Vis-group in Vienna and all around the globe including Stefan Bruckner, Raphael Fuchs, Martin Haidacher, Peter Kohlmann, Muhammad Muddassir Malik, Matej Mlejnek, Philipp Muigg, Daniel Patel, Peter Rautek, Maurice Termeer, and Ivan Viola. I wish the Vis-group keeps the same joy and vitality that characterized it during these three beautiful years I spent as its member.

In particular, special thanks go to my parents who never stopped pushing me forward, my sister, my brother in-law, my wonderful niece Dorothea, and my inspiring muse Dora.

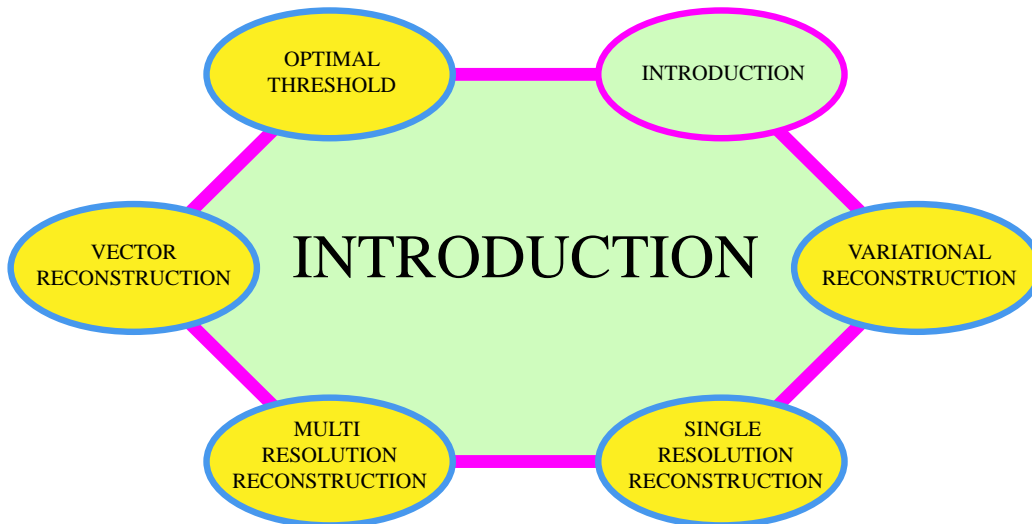
Faleminderit! Without you I would not have achieved this. I dedicate this thesis to you all!

The work presented in this thesis was carried out as part of the Point-based Volume Graphics project supported by the Austrian Science Fund (FWF) grant no. P18547, and partially funded by the National Science and Engineering Research Council of Canada.

Vienna, Austria, October 2009

Erald VUÇINI

Man's understanding of every field of life is often through non-uniform observations in space or time. Indeed, most of the readers of this thesis may sample out the introduction, the conclusion, and possibly a few sections and then try to figure out the rest by reconstruction!



With recent technological advances, non-uniform representations are becoming a crucial factor in acquisition and simulation devices and as such the development of better and more reliable reconstruction and visualization schemes is a necessity. After presenting the motivation of this work, in this chapter we give a general information about the data representations and the existing techniques applied for processing and visualizing non-uniform data. After introducing the datasets and criteria used for evaluating the work, we present the scope and outline of the thesis.

CHAPTER 1

INTRODUCTION

Visualization is focused on enabling and conveying a better and deeper insight about data and processes. In the last decades, unprecedented technological growth and development have contributed to the overall improvement of the visualization pipeline, in particular for the processes of data acquisition and data enhancement. In practical applications over a wide field of studies, one often faces the problem of reconstructing an unknown function f from a finite set of discrete data. These data consist of data sites and data values, and the reconstruction has to approximate the data values at the data sites. In other words, a function F is sought that either interpolates or at least approximates the data. The latter case is in particular important if the data contain noise.

The traditional sources of volumetric data are simulations as well as data acquisition devices. The majority of these devices acquire data on uniform (Cartesian) lattices. In an effort to study larger and more complex problems, there has been a move toward non-uniform data representations, since they offer a way of adapting the measure location (or sample points) according to the importance (variance) of the data. Examples include: a) simple data loss during data communication in sensor networks [99], b) Doppler measurements or other novel acquisition models (polar or spiral) for tomography and magnetic resonance imaging [10], c) adaptive and moving mesh approaches in mathematical simulations in the physical sciences [50], d) particle simulations [70], and e) data from general fields such as astronomy, spectroscopy and signal processing [14].

While the acquisition of data on non-uniform grids has become wide-spread, the available tools for processing, filtering, analysis, and rendering of data are most efficient for uniform representations. There are two competing efforts to deal with non-uniform data: (1) create novel and efficient tools that directly work on them, or (2) convert the non-uniform representation into an efficient intermediate uniform

representation and apply standard tools. Both approaches have advantages and disadvantages. In this thesis we make a contribution towards the latter approach. Among other things, this will allow us to better exploit the capabilities of modern GPUs. A simple illustration of the general paradigm of the thesis is shown in Figure 1.1. The continuous representations are derived from the reconstructed uniform lattices.

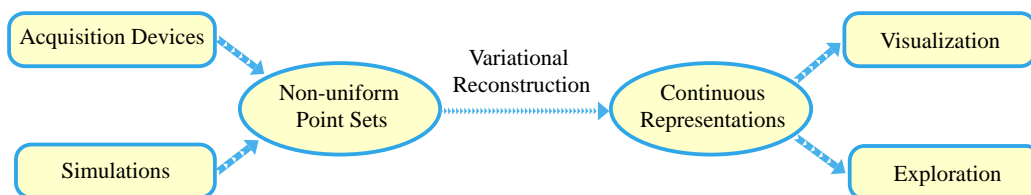


Figure 1.1: Abstraction of the general work-flow of the thesis.

In order to find the best way to transform the non-uniform data onto a uniform grid, we first need to analyze the nature of the given data. One reason for non-uniformity is the ability to capture different scales of information density (e.g. mathematical simulation of shock waves). Another reason for non-uniform data representations could come from imprecise or alternative measurements (e.g. Doppler measurements) or sparse representations (e.g. compressive sensing). While in the former case multi-resolution representations might be most suitable, in the latter case a single resolution representation might be all what is needed. In this thesis we present a framework to adapt to each scenario.

1.1 Data Representations

Three-dimensional (3D) acquisition and simulation devices provide us with a variety of data representations. Depending on the organization of the points (voxels in volumes, or cells in finite element analysis) the data can be classified as regular (Figure 1.2(a)), rectilinear (Figure 1.2(b)), curvilinear (Figure 1.2(c)), and non-uniform (Figure 1.2(d)). The sampling positions in Figure 1.2 are considered to be the line intersections. The first three data representations can be classified as structured, because the 3D point positions (coordinates) can be derived from the implicit structure. Non-uniform grids, also known as unstructured or irregular, are considered in our work as point sets. Hence they do not provide any neighborhood information about the elements (in our case 3D points) in the data. In order to be able to access any single element, we have to explicitly save each point's coordinates along with its respective value. Thus, for storing the same amount

of non-uniform 3D points we need four times more storage than the amount of storage required for the regular (uniform) counterpart. In Figure 1.2(d) the non-uniform representation is shown just for display purposes as being triangulated, since triangles are one of the simplest forms of display primitives.

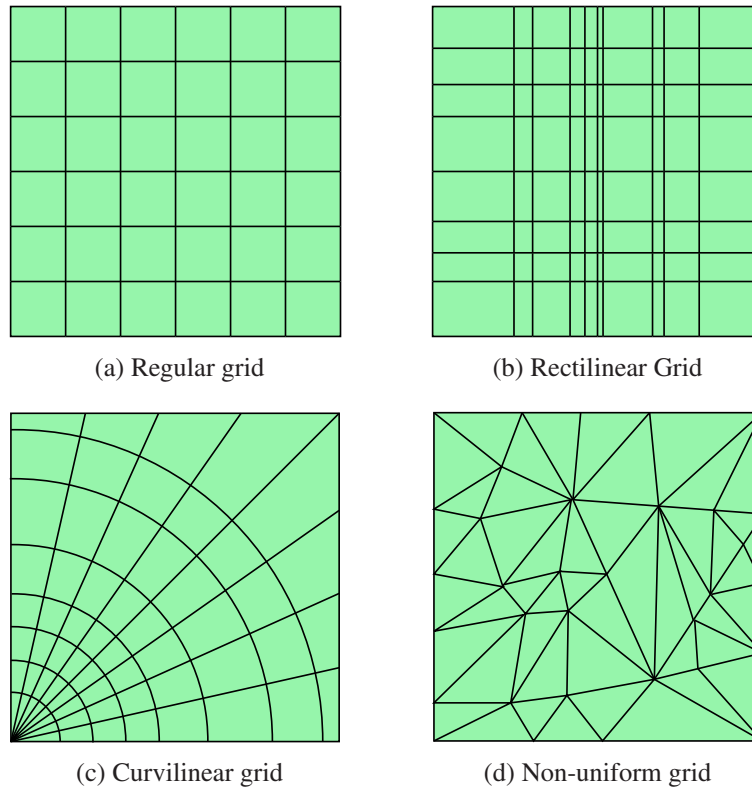


Figure 1.2: Grid Structures.

1.2 Non-uniform Data Encoding and Visualization Techniques

Our thesis brings together concepts from reconstruction and sampling theory, signal processing, multi-resolution analysis, visualization and rendering. As such the citation of all prominent related work in one section would be difficult. Hence, in this section we give a general overview of the most well-known non-uniform data encoding and visualization techniques.

Depending on the underlying data structure and source of acquisition different, techniques have been developed for the visualization and representation of

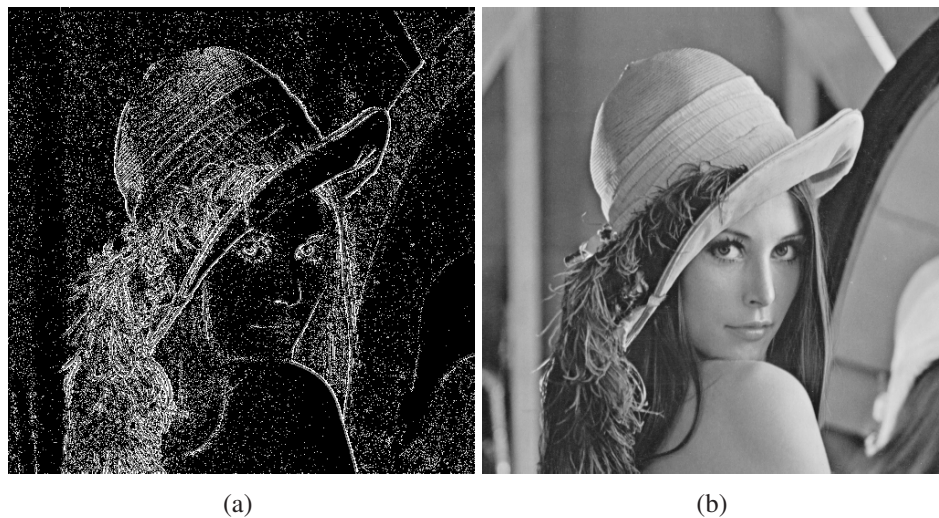


Figure 1.3: *Reconstruction of an image (b) from a given non-uniform point set (a).*

non-uniform data. The early works in this field are extensions of 2D encoding techniques to 3D, especially those with regard to functional approximation and scattered data interpolation [37, 38, 77, 76]. In Figure 1.3 we show an image where 80% of the points were removed, and the respective reconstruction from this non-uniform representation.

A usual approach to the rendering of non-uniform points, in a finite element style, is by first polyhedralizing the point set and then rendering the new structures. There is a considerable body of literature on the rendering of non-uniform data based on finite element analysis (see e.g., [23, 53, 60, 69, 86, 87, 92, 95, 96, 115, 119]). While there are very good reasons to adapt such an approach for rendering, we postulate here that an intermediate transformation onto a regular data structure opens up the possibilities for much more sophisticated data processing in general and henceforth focus on such a pipeline. The main problems here are that the data has first to be subdivided into polyhedra and a correct and fast visibility ordering has to be computed. These problems were tackled by Silva et al. [96], Krishnan et al. [53] and Callahan et al. [23]. Weiler et al. [115] and Schreiner and Scheidegger [92] propose a GPU-based raycasting of tetrahedra with minimized discontinuities between structures. Rössl et al. [87] propose reconstruction of non-discrete uniform tetrahedra partitions via quasi-interpolating quadratic super splines. In Figure 1.4 are shown examples of visualizing non-uniform point sets through finite element analysis. Although there is a continuously increasing number of techniques applied to finite element structures, they cannot match the performance and quality of uniform representations, since they cannot be efficiently implemented in hardware as their uniform counterpart.

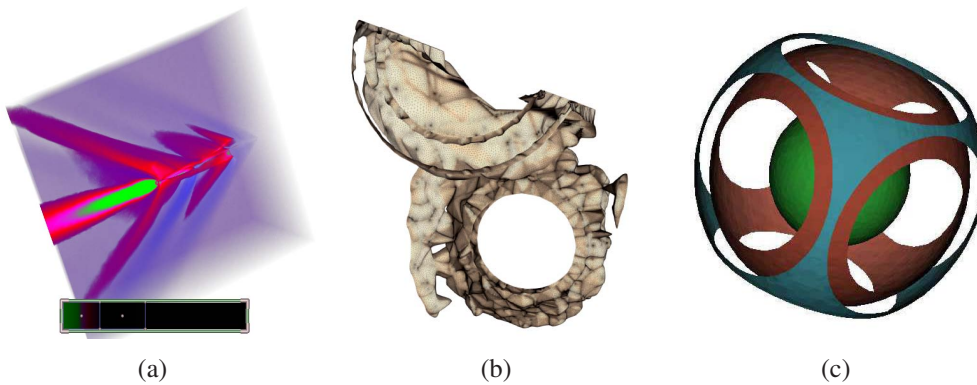


Figure 1.4: Visualization of non-uniform point sets through finite element analysis: a) hardware-assisted visibility sorting [23], b) extraction of isosurfaces from irregular grids [92], and c) hardware-based ray casting for tetrahedral meshes [115].

Data approximation through basis functions is another common approach for encoding non-uniform point sets. The majority of these methods tries to efficiently reconstruct surface and shape from non-uniform point clouds acquired by 3D scanning devices [6, 7, 16, 24, 28, 42, 79, 80, 90, 103, 122]. Radially symmetric functions or radial basis functions (RBFs) were extensively used in most of these approaches. Alexa et al. [6] propose a moving least squares approximation for evaluating local maps. Ohtake et al. [80] propose the approximation of point sets over a piecewise smooth surface by specifying the centers and local support of RBFs according to point density and surface geometry. Zwicker et al. [121] propose the usage of an elliptical average filter for the direct rendering of opaque and transparent surfaces. Some rendering examples from surface visualization using RBFs are given in Figure 1.5.

Radial basis functions have also been applied for the approximation of volumetric data [47, 48, 117, 121]. Extensive research was conducted into the acceleration of the approximation process and the elimination of the visual artifacts from the non-compactness of the basis functions. In Figure 1.6 results are shown from previous work where radial and ellipsoidal basis functions are used for the volume fitting process. Further details will be given in Chapter 3.

Particle systems have received special attention in recent years [1, 61, 70, 71, 72]. While most of the methods of this category are used for conventional isosurface visualization techniques, special interest is drawn on how these methods can be applied to volumetric reconstruction/fitting. The basic concepts of these approaches is that the particles can be distributed adaptively or evenly to accommodate world-space features (in this case the surface). This provides compact, efficient and accurate representations [72]. Examples from visualization methods using particle systems are shown in Figure 1.7

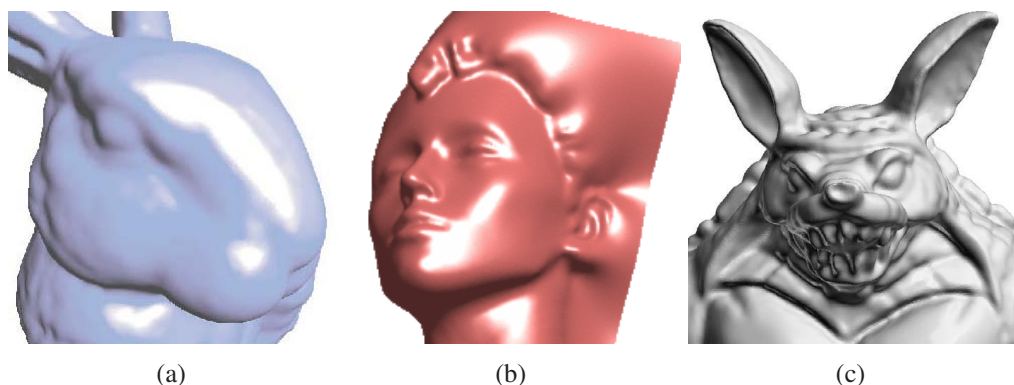


Figure 1.5: Surface reconstruction through basis function representations: a) surface approximation with moving least squares [6], b) surface fitting with RBFs [24], and c) data approximation with compactly supported RBFs [80]

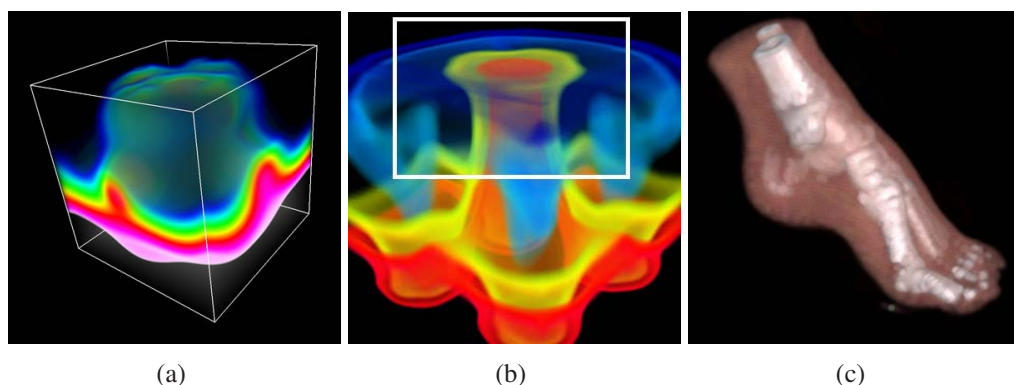


Figure 1.6: Volumetric reconstruction through basis function representations: a) rendering using spherical Gaussian basis functions [48], b) rendering using elliptical Gaussian basis functions [47], and c) rendering using Gabor wavelets [117].

All the above mentioned approaches offer solutions to a specific type of data under special constraints. Recently, there has been some effort in combining rendering techniques for structured and unstructured grids in unified frameworks [51, 58, 74]. Figure 1.8(a) shows a rendering of astronomy data, where the regular grid ray casting has been merged with point sprites obtained from the non-uniform representation. In Figure 1.8(b) the Blunt Fin dataset is rendered using a moving least square (MLS) approximation fitted to an uniform and non-uniform grid displayed using raycasting.

In this thesis we offer a framework converting non-uniform point sets onto a uniform representation either through single- or multi-resolution reconstruction.

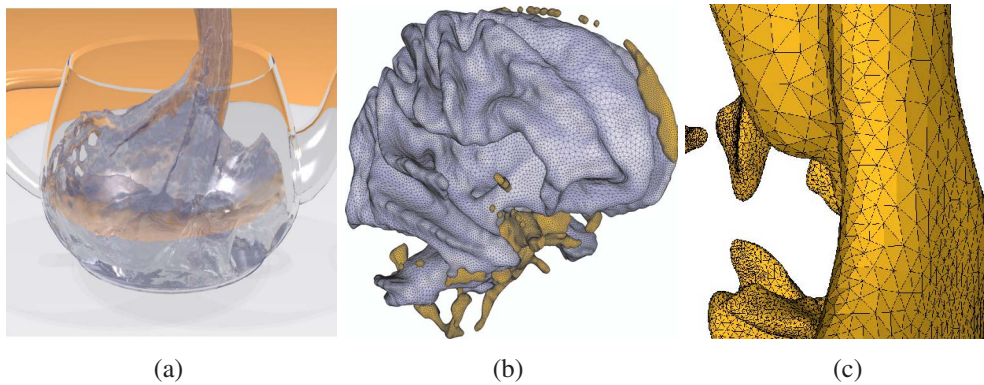


Figure 1.7: Particle systems for the visualization of non-uniform point sets: a) adaptively sampled particle fluids [1], b) particle-based processing of multi-material volumes [72], and c) particle-based meshing of CT data [70].



Figure 1.8: Visualization of non-uniform point sets with hybrid approaches: a) astronomic data rendered with a hybrid ray caster [51], and b) simulation data rendered with a ray caster adopted to MLS [58].

1.3 Datasets

Most of the visualization techniques are fitted to data acquired from specific sources. We tested our framework on several data either obtained by scanning devices, simulation devices, or synthetic simulations. Following is a description of these datasets.

1.3.1 Scalar Datasets

The Oil Reservoir dataset was computed by the Center for Subsurface Modeling at the University of Texas at Austin. This data represents a simulation of a black-oil reservoir model used to analyze the placement of injection and production wells in order to minimize oil explorations. The non-uniform point set consists of 29,094

points containing water pressure values for the injection well.

The Natural Convection dataset consists of several timesteps of temperatures generated from a natural convection simulation of a non-Newtonian fluid in a box. The domain is heated from below, cooled from above, and has a fixed linear temperature profile imposed on the sidewalls. The simulation was developed by the Computational Fluid Dynamics Laboratory at the University of Texas at Austin and consists of 68,921 points organized in hexahedral bricks. Temperature values were encoded as they accurately represent the structures that emerge during the convection process.

The Synthetic Chirp dataset is a synthetic radial sinusoidal wave with spatial frequency that decreases from center to the edges as defined in Equation 1.1:

$$Chirp(x, y, z) = \frac{1 - \sin(z \cdot \pi/2) + b \cdot 0.5 \cdot \left(1 + \cos\left(\frac{w_0 \cdot r \cdot 180}{(r+r_0) \cdot \pi}\right)\right)}{2 + b} \quad (1.1)$$

where r_0 controls how close we go to infinity as we approach the center, w_0 controls the number of maxima between the center and the edges, b is a normalization term, $r = \sqrt{2(x^2 + y^2)}$, $x, y \in [-0.5, 0.5]$ and $z \in [0, 1]$. In our testing scenario we set $r_0 = 5$, $w_0 = 4$ and $b = 0.5$. We create a non-uniform point set by evaluating the Chirp function for 75,000 random points (x, y, z) .

The Bypass dataset is a simulation performed at the department of Mechanics at the Royal Institute of Technology in Stockholm [91]. It consists of 421 timesteps of a simulation from a laminar-turbulent transition in a boundary layer that is subject to free stream turbulence. The dataset consists of 7,929,856 non-uniform points in a curvilinear grid with uniform spacing across the x and z axes and non-uniform spacing along the y axis. Laminar flow is characterized by low momentum convection, pressure, and velocity independent of time. Turbulent flow is characterized by chaotic and stochastic property changes and tends to produce vortices. The breakdown to turbulent flow in a flat-plate boundary layer is dominated by the exponential growth of (unstable) Tollmien-Schlichting (TS) waves, which form typical Lambda-shaped vortices. The visualization of this simulation is of great importance to better analyze how the "bypass" of TS waves develops.

The X38 Vehicle dataset consists of 323,192 non-uniform points computed from an inviscid finite element calculation on a tetrahedral grid. The grid was computed using an advancing front method and was generated from a geometric representation emulating the X38 Crew Return Vehicle. The geometry and the simulation were computed at the Engineering Research Center at Mississippi State University by the Simulation and Design Center. This data set represents a single time step in the reentry process of the vehicle into the atmosphere. During the reentry process, interesting shock structures emerge and dissipate and these

structures have a significant impact on the stability of the vehicle. It is a typical non-uniform dataset where 99% of its points are concentrated in about 5% of the volume.

With the exception of the Synthetic Chirp dataset, all the other datasets are defined as a cloud of points concentrated only at specific positions in the object space. Hence, there is no possibility to exactly measure the accuracy of a reconstruction or visualization method at positions not known apriori. In order to better understand this behavior we created non-uniformly sampled data from regular data sets by adaptively sampling them. For the adaptive sampling of the data we used a 3D Laplacian kernel defined as follows:

$$\text{Laplacian}(V) = \frac{\partial^2 V}{\partial x^2} + \frac{\partial^2 V}{\partial y^2} + \frac{\partial^2 V}{\partial z^2} \quad (1.2)$$

where V represents the volume given as a 3D regular grid. After convolving the data with this 3D filter we sorted the point values according to their magnitudes and retain only those points that have the biggest absolute values (i.e., 20% of all points in our experiments). We denominate these datasets as **Laplacian** dataset. Other filters could have been used, but since the idea of non-uniformly sampled datasets is to represent higher frequency regions with more points, convolution with a Laplacian filter would result in a similar effect. The uniform datasets used in this thesis can be found at <http://www.volvis.org>.

1.3.2 Vector Datasets

The Flow Transport dataset was generated at AVL List GmbH in order to evaluate computational fluid dynamics for fire simulation. It contains flow as well as heat transport solutions. The non-uniform point set consists of 17,120 points containing the 3D velocity field components of the flow data.

The Cooling Jacket dataset was generated at AVL List GmbH in order to evaluate a cooling jacket design for a four cylinder diesel engine. This stationary flow simulation incorporates a heat transport solution in order to predict critical temperature regions within the engine. The original dataset is specified on an unstructured grid composed of different cell types such as hexahedra, four sided pyramids, three sided prisms and tetrahedra. The non-uniform point set consists of 1,537,898 points containing the 3D velocity field components of the flow data.

The Fuel Injection dataset was computed by the Institute for Internal Combustion Engines and Thermodynamics at The Graz University of Technology. This data represents a simulation of fuel injection into a simple piston shape. It consists of 25,190 non-uniform points giving the 3D velocity field components of the fuel simulation.

In order to create non-uniformly sampled vector data, where we know the uniform ground truth, we used the gradients computed from uniform data sets and adaptively sampled them. For the estimation of the gradients we used the central difference operator. For the adaptive sampling of the gradient data we used the 3D Laplacian kernel as described in Section 1.3.1. Inputs to the kernel are the amplitudes of the vector field \mathbf{v} , $\|\mathbf{v}\| = \sqrt{u^2 + v^2 + w^2}$. After convolving the gradient amplitudes with this 3D filter, we sorted the values according to their magnitudes and retain only the points that have the biggest absolute values. We denote these datasets as **Laplacian-Gradient** datasets.

All the vector data is normalized so that the maximum amplitude across the vector field is 1.0.

1.4 Evaluation Metrics

We have tested our method with a variety of datasets and with different parameter settings. An important task of any reconstruction or approximation technique is the reporting of the reconstruction errors and the metrics used for this.

In order to evaluate the quality of our reconstruction, we use the Root Mean Square error (RMS) defined as follows:

$$RMS = \sqrt{\frac{\sum_i^M (F(x_i, y_i, z_i) - f_i)^2}{M}} \times \frac{100}{MaxValue} \quad (1.3)$$

where F is the approximating function, f are the given values, $MaxValue$ is the maximum value in the given point set and M is the number of points. For the error estimation in Laplacian datasets we will use also RMS_g which gives the global RMS in all regular points (including the points not retained in the Laplacian dataset).

Our testing platform is an Intel Dual Core 2.70 GHz processor machine with 8GB of RAM. Since our program is single threaded we are using only one dedicated processor during the reconstruction process.

1.5 Thesis Scope and Outline

The scope of this thesis is to provide an alternative framework to the visualization of non-uniform point sets. The main difficulty of such representations, the lack of neighborhood information, is avoided by providing an efficient method for the reconstruction for 3D scalar and vector data. In this chapter we mentioned some of the most important categories of techniques that deal with non-uniform point sets.

Chapter 2 presents the mathematical background and knowledge of existing reconstruction techniques with special focus on the variational approach. The basis of the variational approach is given. A block-based method is proposed for solving the memory and efficiency problems encountered when adapting the variational approach to the reconstruction of large non-uniform 3D point sets.

Reconstruction from non-uniform point sets is a non-trivial process especially regarding the specification of an optimal reconstruction resolution. We define as optimal reconstruction resolution the lowest resolution which ensures minimal reconstruction error and no visual artifacts. In Chapter 3 we introduce a statistical-based concept for selecting an optimal reconstruction resolution. Furthermore, a new regularization functional is proposed to reduce the reconstruction errors.

Whereas selecting a single resolution can give solutions to cases when the data has an even distribution of points across the volume, a multi-resolution approach is required for the cases when this distribution is not even. In Chapter 4 we present two multi-resolution reconstruction approaches that attack the latter problem from different perspectives.

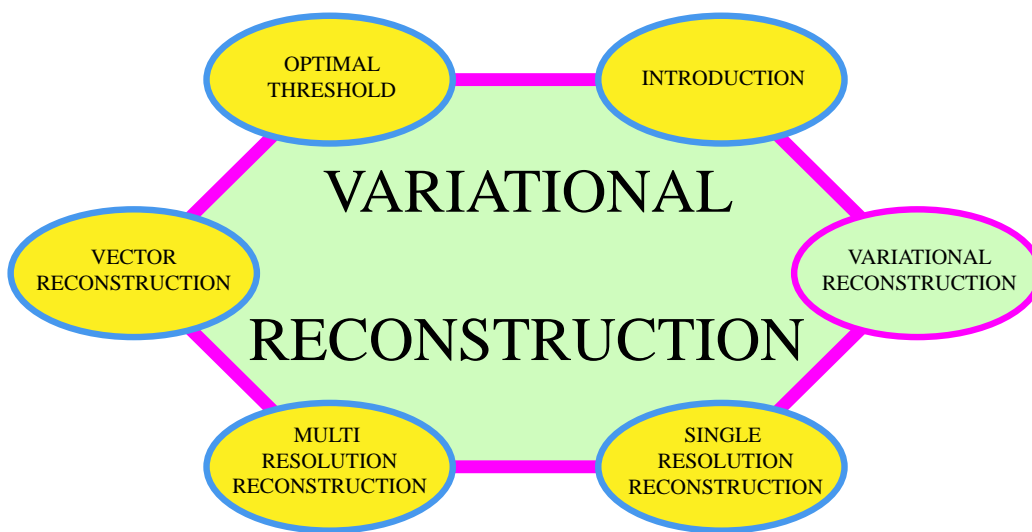
While the main motivation of this thesis is dedicated to the reconstruction from scalar non-uniform point sets, in Chapter 5 we apply our approach to non-uniform vector data. We initially present a straightforward approach obtained by doing component-wise reconstruction of vector data. The method is applied to non-uniform vector datasets obtained either from simulations or from thresholding gradients of uniform datasets. By means of error estimation and vector visualization we show the behavior of our proposed reconstruction technique.

We build Chapter 6 upon statistical data interpretation in an attempt to create a basis for the criterion of selecting an optimal percentage of the Laplacian points. Optimal here refers to the minimal percentage of points selected in a way that the reconstruction errors are lower than a user-defined threshold. An iterative selection method is presented in an effort to find the non-uniform point set, which will yield a reconstruction with minimal error.

Finally, Chapter 7 presents a summary of the thesis and after conclusions are drawn, the ideas for future work are presented.

Do not worry about your problems with mathematics, I assure you mine are far greater.

Albert Einstein



Several mathematical concepts exist in relation to reconstruction from non-uniform data in shift-invariant spaces. Generally, if there is no restriction on the distribution of the samples, the reconstruction is not uniquely defined and hence is ill-posed. In such cases a variational approach is used and the reconstruction routine is formulated as a minimization of two terms: *a*) the sum of squared errors, and *b*) the regularization term that controls the smoothness of the solution. In this chapter we introduce the mathematical background for the variational approach, the argumentation that supports the selection of B-splines as basis functions for the variational approach, and a proposed method for improving the efficiency in terms of memory and time.

CHAPTER 2

VARIATIONAL RECONSTRUCTION

Non-uniform data reconstruction (approximation) is a recent, fast growing research area. It deals with the problem of reconstructing an unknown function from given non-uniform data. A considerable number of approaches has been proposed for the reconstruction of non-uniformly sampled scalar data, especially for one- and two-dimensional signals [33, 34, 39, 59, 67, 89, 94, 120]. The non-uniform reconstruction techniques can be classified as:

- Global fitting methods [33, 34, 39, 89, 100, 120]
- Distance-weighted methods [94]
- Moving least-squares (MLS) methods [32, 35]
- Shift-invariant methods [2, 4, 25, 63]
- Mesh-based methods [54, 65]
- Variational methods [10, 59, 75, 111, 112]
- Radial basis function (RBF) methods [22, 57, 66, 73]

Most of the methods are based on the reconstruction of the data by solving large systems of equations, hence suffering from long computational times [33, 34, 39]. Feichtinger et al. [33] propose a reconstruction algorithm by using adaptive weights, conjugate gradients, and Toeplitz systems to reduce computational effort. Grishin and Strohmer [39] extend this work by using Toeplitz and Hankel matrices with a Neumann boundary condition to improve the reconstruction speed and quality with piecewise trigonometric polynomials. While they provide

good reconstruction results, most of these approaches are based on global reconstruction techniques, since they use basis functions with infinite support. This makes them impractical to use for real-time visualization applications, where finite support reconstruction kernels are desired. Park et al. [82] have presented an efficient discretization of Sibson's natural-neighbor interpolation for 2D and 3D data fitting. While ensuring C^1 continuity, they fail to report experiments for real non-uniform point sets. Nielson [76] has presented an overview of several approximation techniques for non-uniform point sets. While each technique performs best only in particular cases, the use of local compact operators is considered the fastest approach.

A major part of the literature related to non-uniform reconstruction starts from the general assumption that the underlying continuous function is band-limited, hence constraining the space of possible results. Unser [105, 109] suggests to replace the concept of band-limitedness by minimum-error projection on a space of shift-invariant functions. A more general overview on modern non-uniform reconstruction techniques in shift-invariant spaces has been summarized by Aldroubi and Gröchenig [4]. Perhaps the most popular shift-invariant spaces are based on Radial Basis Functions (RBFs).

When choosing a reconstruction method there are several features that should be taken into account, as:

- **Explicit expression:** except the MLS and the mesh-based methods all the other methods can be formulated through explicit mathematical formulations.
- **Ability to handle large sampling gaps:** variational and RBF methods are the best ones in handling large sampling gaps. The least efficient ones are the global-fitting and shift-invariant methods, since they require a minimum density to ensure the convergence of the solution. Mesh-based and MLS methods handle the gaps moderately well.
- **Reconstruction quality:** variational methods are usually believed to be the best in terms of reconstruction errors and smooth visual results. Global fitting and Shepard's method yield the worst quality.
- **Computational complexity:** global fitting, variational and RBF methods have the highest computational complexity, since they require solving a dense system of linear equations. Among the local ones, mesh-based methods also have a complexity that is comparable to the global ones, especially in the presence of regularization.
- **Robustness to noise:** methods that use regularization, as the variational

method, are robust to noise. The RBF methods can be considered to be in the next best techniques with regard to robustness to noise.

2.1 Sampling and Reconstruction

Sampling and reconstruction are two closely related processes. Apriori knowledge of the sampling process on the acquisition device can lead to better reconstruction results. Modern digital data processing of signals (in our case volumes) use a discretized version of the original signal f that is obtained by sampling f on a discrete set. The natural question that arises is whether and how can f be recovered from its samples. Sampling theorems guarantee a perfect reconstruction under specific mathematical conditions. Shannon's theorem provides a method to perfectly reconstruct band-limited signals from their equidistant samples [93]. A function f is band-limited if its energy is finite (in L^2 -space) and its Fourier transform vanishes outside a specific interval. The reconstruction formula for one-dimensional signals that derives from Shannon's theorem is:

$$f(x) = \sum_{k \in Z} f(k) \frac{\sin \pi(x - k)}{\pi(x - k)} \quad (2.1)$$

where $f(k) : k \in Z$ are the discrete samples of the band-limited function.

In 1977, Papoulis [81] introduced an extension of Shannon's sampling theory, showing that a band-limited signal can be exactly reconstructed from the samples of the responses of m linear-shift invariant systems sampled at $1/m^{th}$ of the Nyquist rate [78]. The main contribution of Papoulis is the idea that there are many ways of extracting data for a complete characterization of the sampled function [109]. However these theorems require the signals to be band-limited and to have an infinite number of samples. Real world signals are never exactly band-limited and the number of samples is finite. There is no such device as an ideal low-pass to produce a perfectly band-limited signal. Furthermore, Shannon's reconstruction formula is rarely used due to the very slow decay and finite support of the *sinc* function. In order to deal with those problems, there is a more recent trend that approaches sampling from the perspective of approximation. The goal is to obtain a solution that is as close as possible to the original signal according to some criterion, e.g., in a least squares sense. These methods try to give a solution to the consistent sampling problem [46], using more realistic non-bandlimited functions as reconstruction bases. Unser and Aldroubi [106] further investigated such signals and proposed the use of consistency criteria for the sampling process.

Similar ideas have been extended to the domain of non-uniform sampling and reconstruction. Special interest has been dedicated to the reconstruction of signals

in shift-invariant spaces. However, a lower bound on the minimal distance between two sampling positions has to be assured. For general shift-invariant spaces a Beurling density $D \geq 1$ is necessary for a stable and perfect reconstruction [3]. From the shift-invariant spaces a logical connection can be done to the reconstruction with splines, and in particular with B-splines [104]. With their shift-invariance, compact support and approximation properties they assure the best conditions for the reconstruction process.

2.2 B-splines

Interpolation can be defined as a model-based recovery of continuous data from discrete data within a known range of abscissa [101]. The general form of interpolation is:

$$F(\mathbf{x}) = \sum_{k \in Z^d} c_k \varphi_k(\mathbf{x}) \quad (2.2)$$

where \mathbf{x} is a d-dimensional vector, $\varphi_k(\mathbf{x})$ are the basis functions used in the reconstruction process and c_k are the unknown coefficients associated with each basis function. In the classical form of interpolation, the coefficients c_k are the values of the input samples. The usage of the general form offers new possibilities in choosing a wider range of attractive basis functions.

In our framework we use B-splines as basis functions in the reconstruction process. B-splines, with their shift-invariance and compact support, offer optimal conditions for faster and more accurate reconstruction results. Their symbolic representation is β^n , where $n \in N$ is the degree of the spline. B-splines are piecewise polynomials of degree n , they are symmetric and have a C^{n-1} continuity. They can be formulated as:

$$\beta^0(x) = \begin{cases} 1 & |x| < \frac{1}{2} \\ \frac{1}{2} & |x| = \frac{1}{2} \\ 0 & |x| > \frac{1}{2} \end{cases} \quad (2.3)$$

and

$$\beta^n(x) = \sum_{k=0}^{n+1} \frac{(-1)^k (n+1)}{(n+1-k)! k!} \left(\frac{n+1}{2} + x - k \right)_+^n \quad (2.4)$$

where $(x)_+^n = (\max(0, x))^n$ and n is a positive integer.

As described by Thévenaz et al. [101] and by Unser et al. [107, 108], B-splines have several properties which make them very suitable for signal approximation. We mention properties such as easy analytical manipulation, several recursion relations, minimal curvature, easy extension to quasi interpolation and simplicity

of their parametrization. One basic feature, which makes B-splines very suitable in applications related to signal approximation, is that they enjoy the maximal order of approximation for a given integer support, providing the best quality for a given computational cost [102]. B-splines of degree higher than one do not enjoy the interpolating property, but this is not required in most of the applications that deal with noisy samples. If such a feature would be required, it can be achieved through an additional digital filtering step [104], which in turn would introduce extra computational effort.

2.3 Variational Reconstruction: Theory

In approximation theory, if there is no restriction on the distribution of the samples, the reconstruction problem is not uniquely defined and hence ill-posed. The variational approach gives a solution to the general ill-posed reconstruction problem expressed by Equation 2.2. In such cases the reconstruction routine is formulated as a minimization of two terms: (1) the sum of squared errors, and (2) the regularization term that controls the smoothness of the solution. The first part guarantees that the solution is close to the sample points, while the second part ensures that there are no discontinuities in the reconstruction. In variational theory the best results with regard to approximation accuracy are given by RBFs, and particularly by a specific class of basis functions known as thin plate splines [22]. While thin-plate splines are one of the preferred approaches to deal with multi-dimensional non-uniform data, they tend to be computationally expensive when the number of points increases significantly. To overcome this problem Arigovindan et al. [10] propose to discretize the thin-plate splines using uniform B-splines attached to the reconstruction grid. While the discretization process holds mathematically for one dimensional signal reconstruction, for higher dimensions there are no compactly supported B-splines that span the same space as the thin-plate splines. However cubic B-splines are very good candidates for the reconstruction process. Cubic B-splines can be formulated as:

$$\beta^3(x) = \begin{cases} \frac{2}{3} - \frac{1}{2}|x|^2(2 - |x|) & 0 \leq |x| < 1 \\ \frac{1}{6}(2 - |x|)^3 & 1 \leq |x| < 2 \\ 0 & 2 \leq |x| \end{cases} \quad (2.5)$$

Given a set of sample points, $p_i = (x_i, y_i, z_i)$, $i = 1, 2, \dots, M$, let f_i be the scalar value associated with p_i . We define the B-spline approximation through the form:

$$F(x, y, z) = \sum_{k=0}^{N_x-1} \sum_{l=0}^{N_y-1} \sum_{m=0}^{N_z-1} c_{k,l,m} \beta^3(x - k) \beta^3(y - l) \beta^3(z - m) \quad (2.6)$$

where $\beta^3(x)$ is the cubic B-spline basis function and $c_{k,l,m}$ the B-spline coefficients. In order to determine the coefficients the following cost function is minimized:

$$C(F) = \sum_{i=0}^{M-1} \|F(x, y, z) - f_i\|^2 + \lambda \int \int \int \|D^p F\|^2 dx dy dz \quad (2.7)$$

where λ is a parameter that controls the smoothness and the second term is the regularization term that uses Duchon's seminorms. $D^p F$ can be formulated as follows:

$$\int \int \int \|D^p F\|^2 dx dy dz = \sum_{q_1+q_2+q_3=p} \binom{p}{q_1} \binom{p-q_1}{q_2} D_{q_1, q_2, q_3} \quad (2.8)$$

with

$$D_{q_1, q_2, q_3} = \int \int \int \left(\frac{\partial^p F}{\partial x^{q_1} \partial y^{q_2} \partial z^{q_3}} \right)^2 dx dy dz \quad (2.9)$$

The crucial part of the variational technique is to express the second term in Equation 2.7 by means of the first term. This can be achieved using Duchon's semi-norms which are a combination of the sum of partial derivatives of a degree chosen respectively to the reconstruction technique and spline degree (p should be smaller than the spline degree [30]). In our framework we use $p = 2$.

2.3.1 Matrix formulation

We can express Equation 2.7 with a simpler formulation using the following matrix representations:

$$\begin{cases} c = [c_{0,0,0} \dots, c_{N_x-1,0,0}, \dots, c_{N_x-1, N_y-1, N_z-1}] \\ f = [\dots f_i \dots] \\ F_{i, N_x N_y m + N_x l + k} = \beta^3(x_i - k) \beta^3(y_i - l) \beta^3(z_i - m) \end{cases} \quad (2.10)$$

The cost function can now be rewritten as:

$$C(F) = \|f - Fc\|^2 + \lambda c^T R c \quad (2.11)$$

where R is a block-circulant filter that corresponds to a regularization filter which is derived from the Duchon's semi-norm. By applying the Euler-Langrange functional equation for variable c we have:

$$[F^T F + \lambda R]c = F^T f \quad (2.12)$$

We denote $A = F^T F + \lambda R$ and $b = F^T f$ for the sake of simplicity. Then Equation 2.12 takes the form $Ac = b$. We solve this system of linear equations by using a multi-grid V-cycle method [20, 44]. In each cycle the solution is refined through a Gauss-Seidel iteration operator [43].

2.3.2 B-spline Interscale Relation

One of the most important properties of B-splines of odd degree is the interscale (two-scale) relation:

$$\beta^n\left(\frac{x}{2^j}\right) = \sum h(k)\beta^n\left(\frac{x}{2^{j-1}} - k\right) \quad (2.13)$$

where $h(k)$ is the binomial filter [12].

Being based on the basic feature of the two-scale relation of odd degree B-splines Arigovindan et al. [10] propose a multigrid iteration algorithm for finding the solution to the cost minimization problem. Considering the reconstruction at different scales, we specify 2^j as the scale size and we have:

$$F^{(j)}(x, y, z) = \sum_{k=0}^{\frac{N_x-1}{2^j}} \sum_{l=0}^{\frac{N_y-1}{2^j}} \sum_{m=0}^{\frac{N_z-1}{2^j}} c_{k,l,m}^{(j)} \beta^3\left(\frac{x}{2^j} - k\right) \beta^3\left(\frac{y}{2^j} - l\right) \beta^3\left(\frac{z}{2^j} - m\right) \quad (2.14)$$

For $j = 0$ the reconstruction is at its finest resolution ($N_x \times N_y \times N_z$) and for $j = 1$ each dimension is divided by two. Once we specify the desired resolution level, we can make use of the downsampling and upsampling of the signal related to the two-scale relation of B-splines. The idea is to downsample the signal to a coarser resolution, solve Equation 2.12 iteratively and then upsample the signal for getting a finer resolution. The upsampled signal will serve as initialization for the B-spline coefficients at a finer level of resolution. At each level of resolution an error refinement scheme is applied. The multigrid scheme ensures the fast convergence of Equation 2.7 to its solution in each dimension. At the end this scheme will give our desired reconstructed signal. The resolution coarsening can be defined through the following equations:

$$\begin{cases} A_{j+1} = U_j^T A_j U_j \\ R_{j+1} = U_j^T R_j U_j \\ b_{j+1} = U_j^T b_j \end{cases} \quad (2.15)$$

where U_j is a matrix representing the upsampling operation which is achieved by convolving the signal with a circulant matrix corresponding to the filter kernel of the B-spline two-scale relation formula ([83] and [110]). The adjoint operation is the downsampling operation D_j where $D_j = U_j^T$. Once a coarser resolution signal is obtained the equation 2.12 is solved through a Gauss-Seidel iterator. The advantage of this multigrid interscale technique is that the solution in the lower resolution is more efficient and faster. The upsampling and error refinement is applied several times until we obtain the target resolution.

2.4 Block-based Reconstruction

A custom solution to the variational method with thin-plate splines as basis functions would require the calculation of the weights as well as the centers of the basis functions. The linear system to find such a solution is mostly ill-posed and has a poor numerical behavior. For solving such a system, when M non-uniformly sampled points are given, we have to deal with an $\mathcal{O}(M)$ complexity. Once the weights are specified, the next step would be to resample the thin-plate splines on a regular grid. This would require an additional $\mathcal{O}(MN^3)$ operations where N^3 is the resolution of the dataset [9].

The method adopted in our framework has several advantages over the thin-plate spline solution. Since B-splines have a compact support the system is better conditioned. Thanks to the multigrid interscale relation the solution of the system is very efficient and the complexity is reduced to $\mathcal{O}(N^3)$. Furthermore, there is no need for a resampling step since the samples at the grid positions can be obtained by a simple filtering of the B-spline coefficients. Hence, the reconstruction time is dependent not on the number of non-uniform points but on the size of the uniform grid.

One of the main problems of the variational method is memory requirements. For each grid position we estimate the B-spline basis functions $(\beta^3(x), \beta^3(y), \beta^3(z))$, that vary in accordance with the point coordinates. Each coefficient is affecting four positions by its value along each dimension (due the support of cubic B-splines), hence we are dealing with $4N \times 4N \times 4N$ data. Assuming floating point numbers, for a dataset of size $256 \times 256 \times 256$ we will need 4GB of memory.

This bottleneck brought us to the idea of reconstructing the point set in block-wise fashion. One important issue we faced in the straightforward implementation of block-based reconstruction was the discontinuity problem between neighboring blocks (Figure 2.1(b)). To overcome this problem we decided to extend the blocks in each direction by a certain number of voxels. Taking into consideration the local support of a cubic B-spline and also the reconstruction results, we extended each block by two voxels in each direction, having thus a 4-voxel overlap between blocks. In Figure 2.1 we show the rendering of the CT-Head dataset with and without block-overlap. No visual discontinuities are present when we apply a 4-voxel block overlap (Figure 2.1(c)).

In order to improve performance, the implementation of the variational method is based on reconstruction of blocks with sizes that are a power of two. The size of the block influences the reconstruction times. The time needed for the reconstruction of a block of size $2^N \times 2^N \times 2^N$ is 8 times higher than the time required for reconstructing a block of size $2^{N-1} \times 2^{N-1} \times 2^{N-1}$. When we select a small block-size (e.g., 8, 16 or 32) the impact of overlap in reconstruction times is

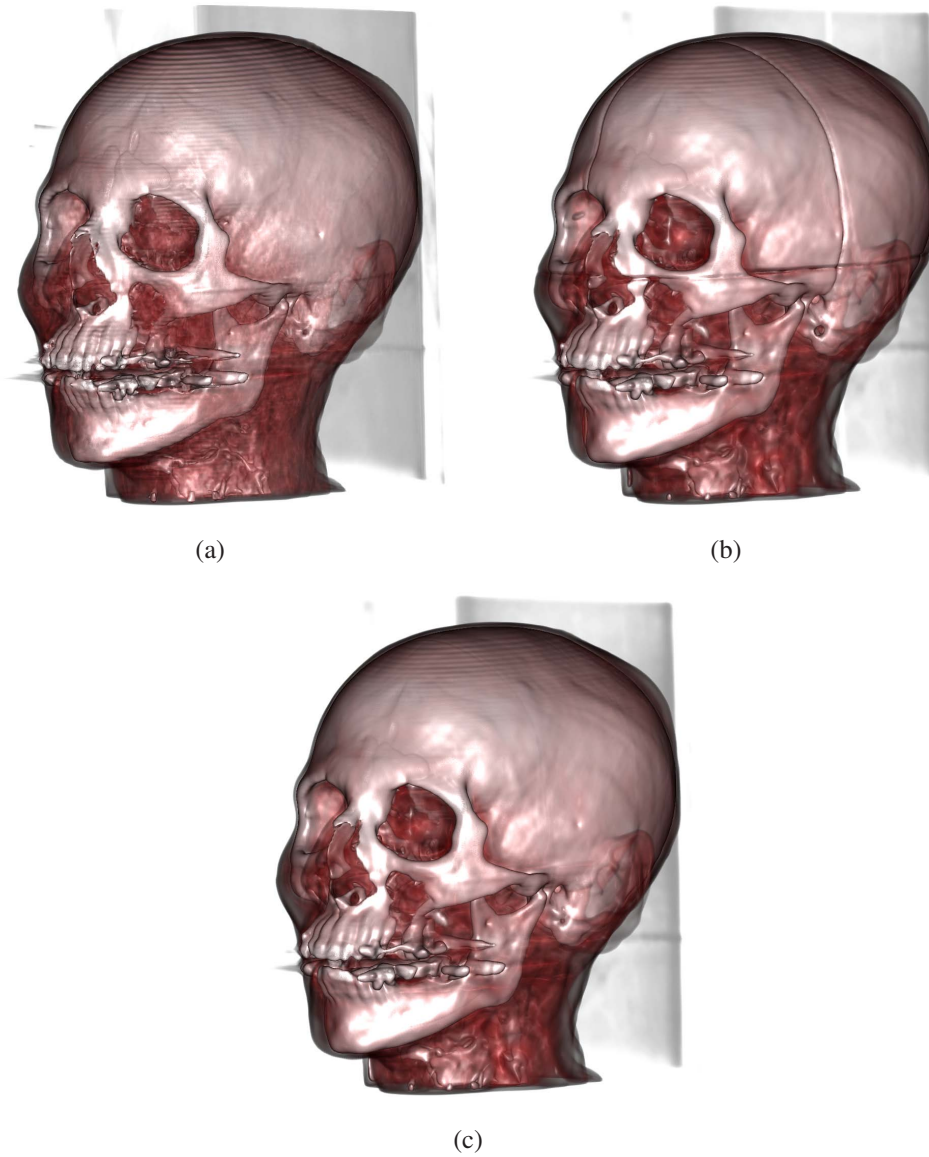


Figure 2.1: Rendering of the CT-Head dataset: a) original dataset, b) reconstructed dataset with no overlap between blocks, and c) reconstructed dataset with 4-voxel overlap between blocks. 20% of the original dataset points were used in b) and c). The block size used is $128 \times 128 \times 128$.

higher than in the case when blocks of a bigger size are used. The size of a block (optimal block-size) along each dimension for which the lowest reconstruction time is required can be found through the following reasoning. If we denote with N_x one of the dataset dimensions, e.g. its width, and with 2^Q the maximum block size dimension due to memory constraints, then the optimal block-size is 2^{Q-k}

where k minimizes the following function:

$$BlockSize(k) = \left\lceil \frac{N_x - L}{2^{Q-k} - L} \right\rceil \cdot 2^{-k} \quad (2.16)$$

where L is the overlap between blocks, $\lceil x \rceil$ is the smallest integer greater or equal to x and $(2^{Q-k} - L) > 1$. The expression in $\lceil \cdot \rceil$ gives the number of blocks to be used for dimension N_x . As the block-size (2^{Q-k}) increases the number of blocks decreases, but the time required for reconstructing each block increases by a two-order relation (hence the multiplication with 2^{-k}).

2.5 Results

We have tested our method with a variety of datasets and with different parameter settings. We obtained the non-uniform representation from a Cartesian (high-resolution) representation, by selecting the Laplacian points as explained in Section 1.3. Unless stated otherwise we use $\lambda = 1.0$ for all the results of this section.

First we tested various block sizes in order to find the optimal one. Here, optimal refers to minimal reconstruction error and best timing performance. In Table 2.1 we show the reconstruction timings and errors of several datasets for four different block sizes. As we found in our results, the variation of block size has a negligible effect on the reconstruction errors. However, timings are strongly dependent on the block size. According to these results and the mathematical concept introduced in the previous section, the optimal block size for most of the datasets is $64 \times 64 \times 64$. As we reduce the block size, the overlap portion becomes decisive in the timing performance. When $16 \times 16 \times 16$ blocks are used the reconstruction timings are almost twice the timings of the $64 \times 64 \times 64$ block-size cases.

The calculated errors for some well-known and widely used datasets are given in Table 2.2. For each dataset we take only 20% of the points from a Cartesian dataset after applying a Laplacian filter. Then we show the reconstruction error and the times (in minutes) required for reconstructing the whole dataset from the non-uniform point set. All the reported errors were computed with a block-based reconstruction, except for the Neghip and Hydrogen dataset, which have dimensions that allow non-block-based reconstructions.

For the rendering of the datasets we have used VolumeShop [21] which is an open source volume rendering platform. The volumes are rendered with a GPU-based raycaster with a sampling step of 0.25. For some of the datasets the rendered images are shown in Figures 2.2, 2.3 and 2.4.

In non-uniform reconstruction approaches which apply exact interpolation techniques, the number of points used for reconstruction highly affects the reconstruction error. In approximation approaches that use basis functions that are not inter-

Table 2.1: Reconstruction times (in minutes) and RMS_g errors for different block sizes applied to several datasets.

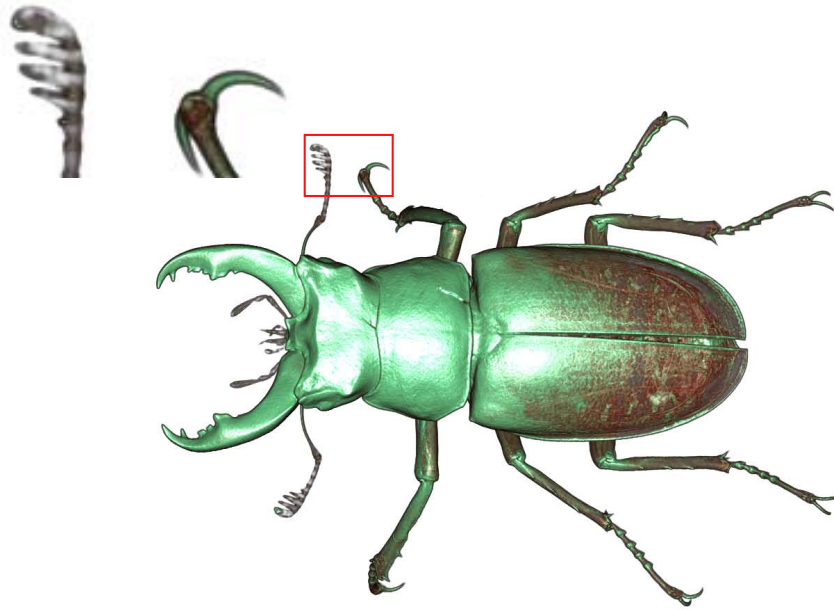
Dataset		RMS_g and Times (min)			
Name	Size	16x16x16	32x32x32	64x64x64	128x128x128
Engine	$256 \times 256 \times 128$	2.20 2.37	2.26 1.29	2.24 1.55	2.24 2.67
Tooth	$256 \times 256 \times 160$	0.24 3.75	0.23 2.12	0.23 1.88	0.23 3.22
CT-Head	$256 \times 256 \times 224$	3.04 4.74	2.92 2.83	2.93 2.60	2.93 3.40
Carp	$256 \times 256 \times 512$	0.57 11.48	0.55 6.23	0.50 5.73	0.55 8.36
CT-Chest	$394 \times 394 \times 240$	1.33 11.06	1.31 6.13	1.31 6.15	1.32 6.28
Christmas	$512 \times 499 \times 512$	0.50 42.14	0.50 24.94	0.50 17.94	0.50 24.08
Stag-Beetle	$832 \times 832 \times 494$	0.32 114.59	0.31 58.94	0.31 50.12	0.31 61.65

Table 2.2: Reconstruction times (in minutes) and RMS_g errors for the variational method. Each reconstruction is based on 20% of the points of the original dataset. An optimal block-size estimated using Equation 2.16 is used in the reconstruction process.

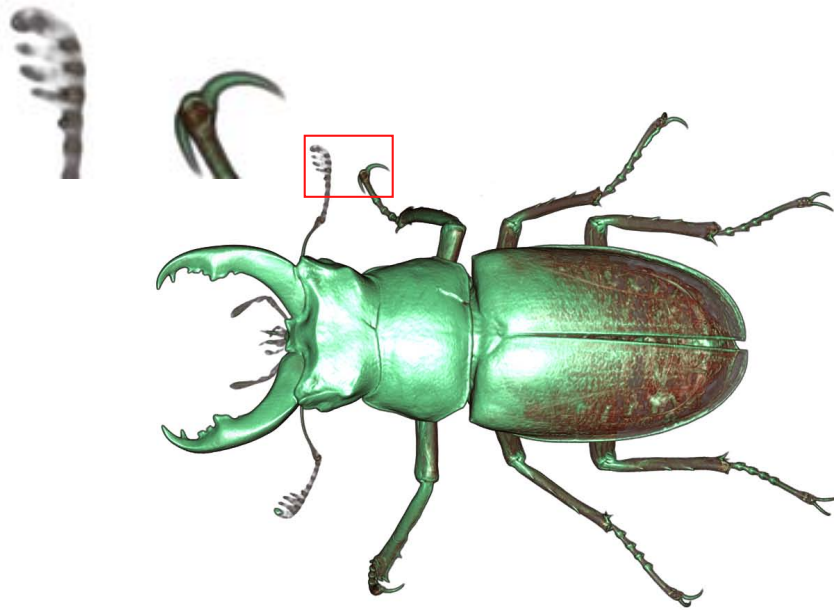
Dataset	Size	Block size	RMS_g	Times (min)
Neghip	$64 \times 64 \times 64$	$64 \times 64 \times 64$	2.14	0.02
Hydrogen	$128 \times 128 \times 128$	$128 \times 128 \times 128$	0.17	0.21
Lobster	$301 \times 324 \times 56$	$32 \times 128 \times 64$	1.21	0.83
Statue Leg	$341 \times 341 \times 93$	$128 \times 128 \times 128$	0.95	1.47
Engine	$256 \times 256 \times 128$	$64 \times 64 \times 32$	2.24	1.28
Tooth	$256 \times 256 \times 160$	$64 \times 64 \times 64$	0.23	1.88
CT-Head	$256 \times 256 \times 224$	$64 \times 64 \times 128$	2.93	2.60
Foot	$256 \times 256 \times 256$	$64 \times 64 \times 64$	2.16	3.10
Carp	$256 \times 256 \times 512$	$64 \times 64 \times 64$	0.50	5.73
CT-Chest	$394 \times 394 \times 240$	$64 \times 64 \times 128$	1.31	5.08
Christmas	$512 \times 499 \times 512$	$64 \times 64 \times 64$	0.50	17.94
Stag-Beetle	$832 \times 832 \times 494$	$64 \times 64 \times 64$	0.31	50.12

polating, as the variational method that we have presented here, there is always a certain limit where even if we increase the number of points the reconstruction error will remain stable. This is strongly connected to the regularization parameter which controls the smoothing. In our experiments we concluded that we can achieve a stable reconstruction rate when using 15%-25% of the points. In Chapter 6 we give further details for the behavior of the variational approach.

Smoothing is another factor that affects the reconstruction error. Smoothing



(a)



(b)

Figure 2.2: Rendering of the Stag Beetle dataset ($832 \times 832 \times 494$): a) original dataset, and b) reconstructed dataset using 20% of points. The RMS_g error is 0.31.

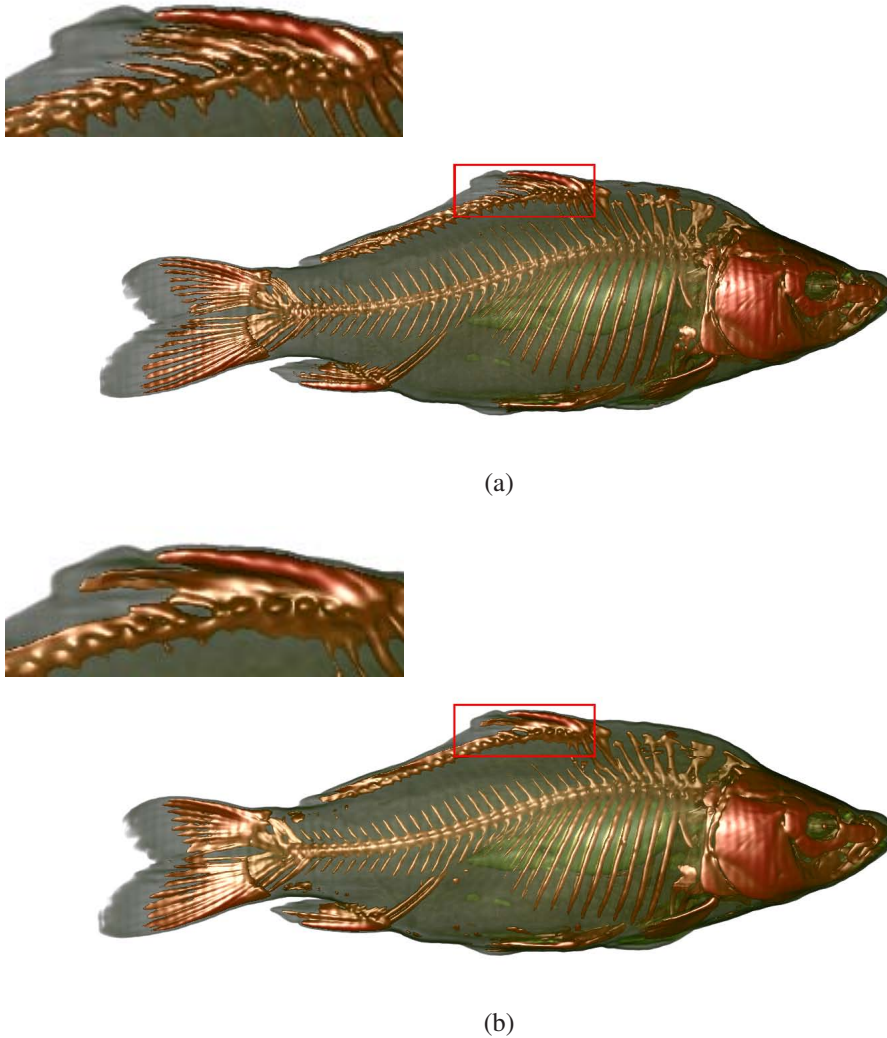


Figure 2.3: Rendering of the Carp dataset ($256 \times 256 \times 512$): a) original dataset, and b) reconstructed dataset using 20% of points. The RMS_g error is 0.5.

lowers the noise levels but it also eliminates details in the data. A compromise is required between accuracy and smoothness. In Figure 2.5 we display the CT-Chest dataset for different levels of smoothing. In Figure 2.5(b) there is too much visual noise due to low smoothing. In Figure 2.5(d) the high frequencies are removed due to the high smoothing operator.

The reconstruction from non-uniform point sets is very important also in communication theory where parts of a uniform signal often are lost during transmission, hence creating a non-uniform representation. We created a typical testing scenario for this case. We blurred a signal (uniform dataset) with white noise (with



(a)



(b)

Figure 2.4: Rendering of the Christmas dataset (512x499x512): a) original dataset, and b) reconstructed dataset using 20% of points. The RMS_g error is 0.50.

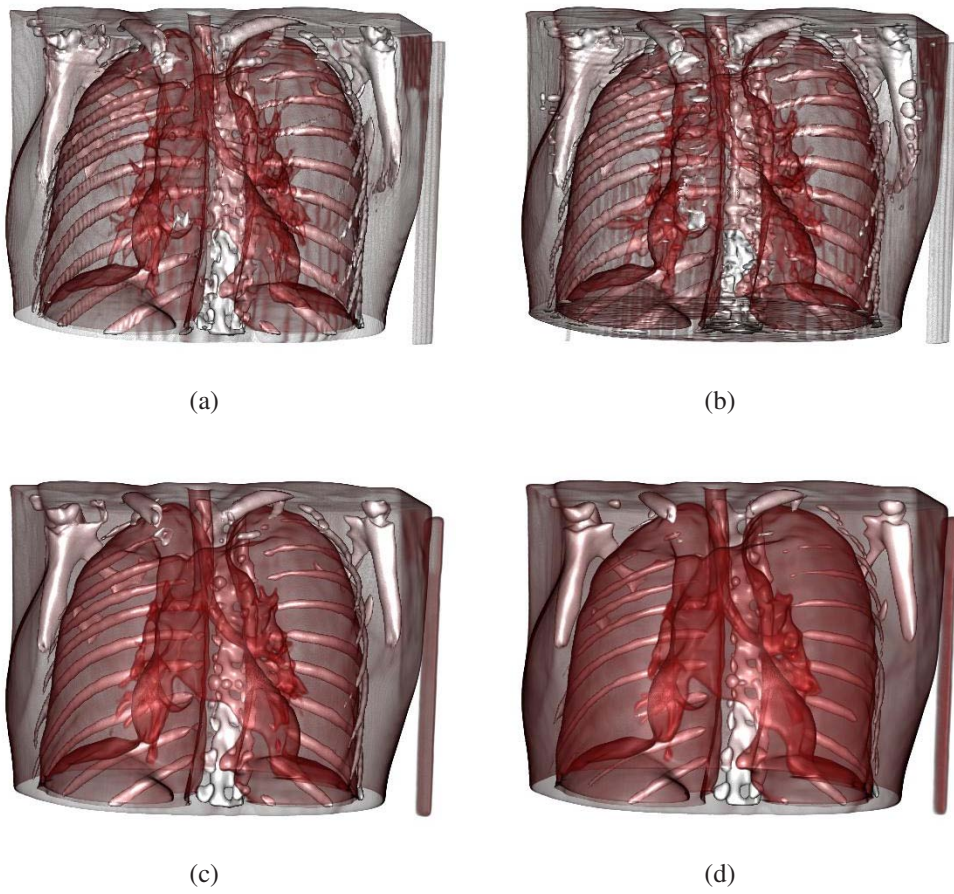


Figure 2.5: Examples of reconstructions using different levels of smoothing of the CT-Chest dataset ($394 \times 394 \times 240$): a) original dataset, b) reconstructed dataset with $\lambda = 0.5$, c) reconstructed dataset with $\lambda = 0.7$, and d) reconstructed dataset with $\lambda = 1.0$. The reconstruction errors (RMS_g) are, respectively, 2.43, 1.34 and 1.76. 20% of the Laplacian points were used.

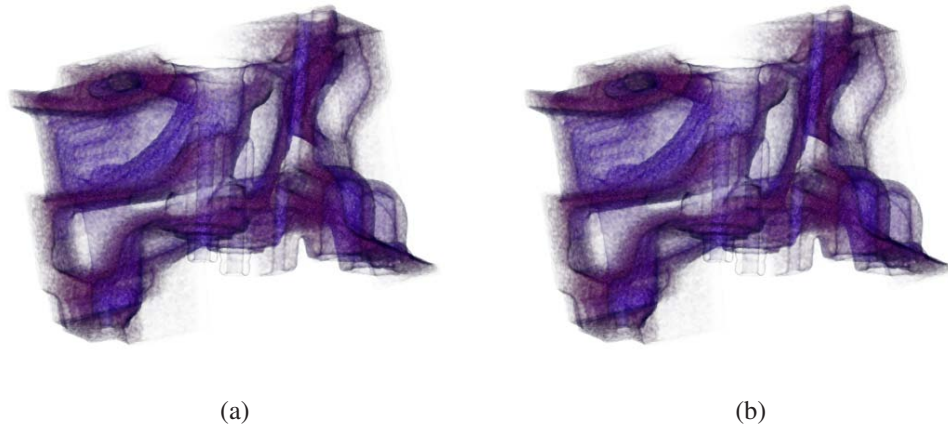


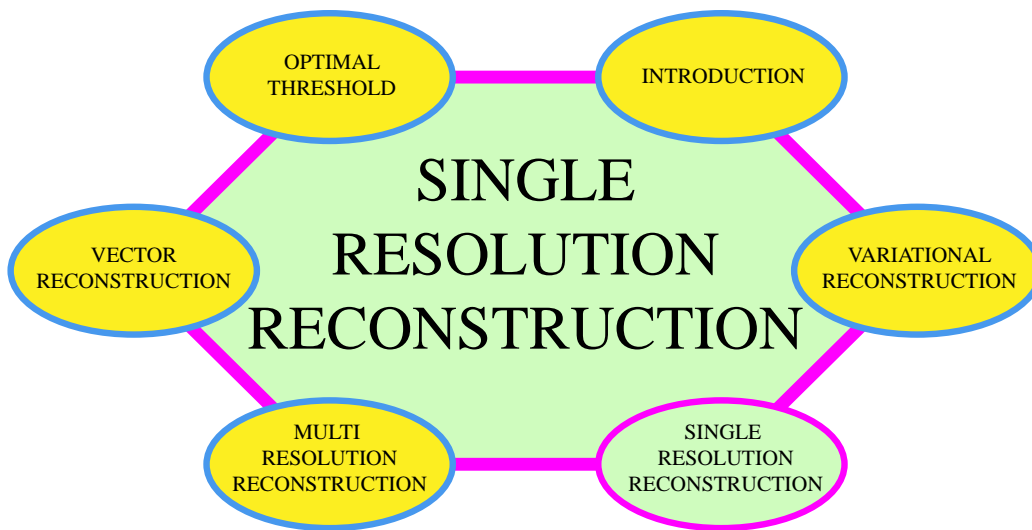
Figure 2.6: Renderings of the Engine dataset ($256 \times 256 \times 128$): a) uniform representation corrupted with 5dB white Gaussian noise, b) reconstruction of 2,516,582 non-uniform points taken randomly from the uniform representation corrupted with 5dB white Gaussian noise.

a signal to noise ratio of 5dB) and then discarded 70% of the samples randomly. In Figure 2.6(a) we show the rendering of the uniform dataset corrupted with noise. In Figure 2.6(b) we give a result of the reconstruction from the non-uniform data. The result shows that our method performs well also in the case where the signal is corrupted with noise.

Although we do not aim for a compression technique, our method achieves a reduction of up to 60% of the original dataset size when 20% of points are kept for reconstruction. We do not apply any compression technique, but just save the coordinates and values in a slice/row basis.

The truth is rarely pure and never simple!

Oscar Wilde



The key issue in resampling a non-uniform point set into a uniform representation is the selection of the proper resolution. This will be the central question we are trying to answer in this chapter. We first assume that we can only afford a single resolution and we make suggestions on how this resolution can be best obtained. This is applicable for non-uniform data, where the distribution of samples is even (in the sense of a discrepancy measure), e.g., ultrasound data or seismic data. Furthermore we introduce a new regularization functional and show its impact on the improvement of the reconstruction results.

CHAPTER 3

SINGLE-RESOLUTION RECONSTRUCTION

In the previous chapter we introduced the basics of the variational approach and how to adapt this technique for the usage in a block-wise fashion for large 3D non-uniform point sets. In this chapter we give more insight to two factors that affect the variational reconstruction process: (1) the optimal resolution selection, and (2) regularization. As we will show in the results section both these factors have a huge impact on the reconstruction quality. In Figure 3.1 we see such a relation showing the behaviour of our variational approach. If λ is small then there is less regularization, hence the reconstruction is closer to the input points. While this is positive for the reduction of the reconstruction error, the negative side effect is that our approach will show poor reconstruction in areas where big gaps are present. This is due to the low regularization and smoothing. We also notice that the higher the resolution of reconstruction the lower the RMS error. Of course a trade-off between memory requirements and reconstruction quality has to be made.

In Chapter 2, we stated that the variational and RBF-based approaches are considered the best with regard to reconstruction quality. For every reconstruction technique to be evaluated, comparison to state of the art techniques should be provided. Hence, in this chapter we give a detailed comparison of our method [112] to two methods introduced by Jang et al. [47, 48]. Jang et al.'s [48] method is formulated as an iterative algorithm for finding the centers and weights of the RBFs using a PCA-based clustering technique by applying truncated Gaussians as basis functions. This technique suffers from high-encoding times and is best suited for locally isotropic structures. Later they [47] adapt their technique to ellipsoidal basis functions (EBFs). The high computational cost is still the main bottleneck of this approach.

Welsh and Mueller [117] introduce a method for converting regular volumes to non-uniform spherical and ellipsoidal Gaussian RBFs and render them via splatting.

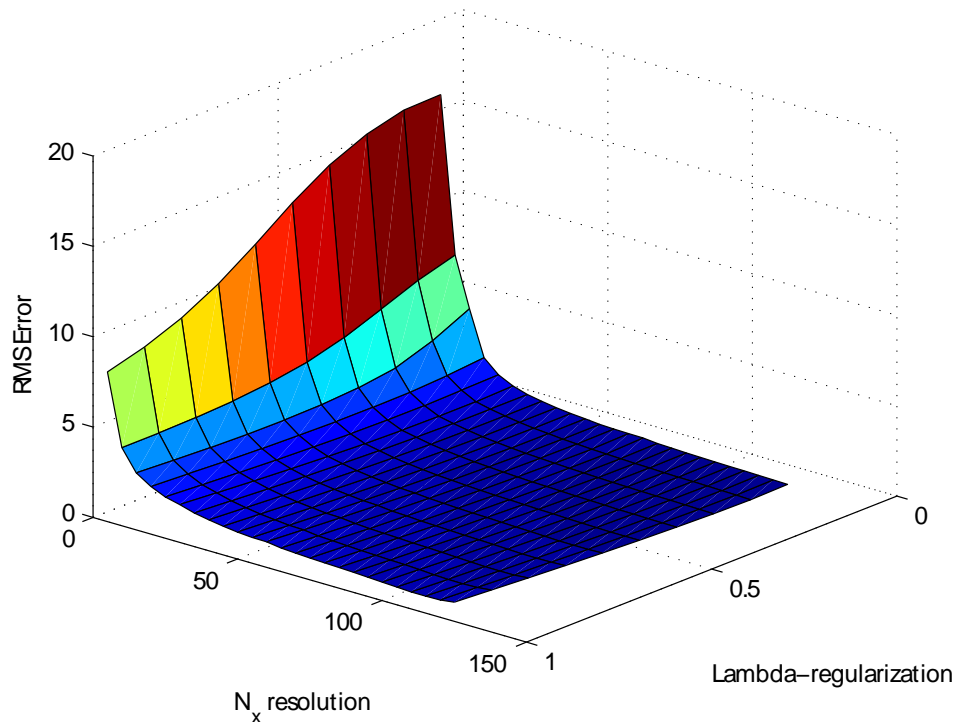


Figure 3.1: Graphs showing the RMS error according to the changes of the lambda regularization and resolution of reconstruction. The testing was performed with the Natural Convection dataset.

Juba and Varshney [49] propose the encoding of volumes with truncated Gaussian basis functions and rendering with a GPU-based ray caster. Zwicker et al. [121] propose direct volume rendering using a splatting approach to visualize volumes encoded with elliptical Gaussian kernels.

The non-uniform reconstruction techniques can be divided into two main groups according to the way the data was acquired [68, 118]. The techniques in the first group try to reconstruct a signal by considering the non-uniform points as part of a uniform grid where the missing point values have to be evaluated. The techniques of the second group consider the reconstruction of the point set at any desired resolution. All the above-mentioned approaches consider the resolution of reconstruction as known a priori. In this chapter we provide an insight on the selection of an optimal resolution.

3.1 Resolution Selection

The key issue in resampling a non-uniform point set into a uniform representation is the selection of the proper resolution. This will be the central question we are trying to answer in this section. We first assume that we can only afford a single resolution and we make suggestions on how this resolution can be best obtained. This is applicable for non-uniform data, where the distribution of samples is even (in the sense of a discrepancy measure), e.g., ultrasound data, seismic data, or data with missing samples.

Increasing the resolution results in a decrease of the error, since the oscillations in the data can be captured with more precision. Finding the optimal resolution ($N_x \times N_y \times N_z$), in terms of minimal reconstruction error, would therefore require estimating the error. We propose to do so by simply looking at the error within a single grid cell. If there are many non-uniform points inside a cell, and their standard deviation σ_k is large, the cell might be too large. Therefore, we propose to approximate the error by using the average standard deviation, defined as:

$$\sigma_{avg} = \frac{\sum_{k=0}^{N_{total}-1} \sigma_k}{N_{total}} \quad (3.1)$$

as an indicator for the proper uniform grid resolution. N_{total} is the number of cells in the volume, i.e., $N_{total} = N_x \cdot N_y \cdot N_z$. Empty cells are considered as cells with zero standard deviation.

We analyze a number of data sets in order to arrive at a reasonable threshold. Our idea is motivated by the strong correlation observed between the reconstruction error and the average standard deviation of point values.

3.2 Improving Regularization

Regularization provides a framework for converting ill-posed problems into well-posed ones by restricting the domain of possible solutions via smoothing constraints. Arigovindan et al. [10] suggest using Duchon's semi-norms ($D^p F$) for regularization. For $p = 1$ and $p = 2$ this norm yields a minimization of an energy functional associated with a membrane and a plate model respectively [30, 85]. Here, we propose a new regularization functional in order to reduce reconstruction errors for anisotropic signals. We denote it as Laplacian regularizer. The main motivation for this idea lies in the fact that cubic B-splines have a better response to high frequencies. These frequencies can be better detected and preserved by convolving the signal with a Laplacian regularization kernel [105]. Our proposed regularization functional consists of the sum of second degree derivatives if cubic B-splines are used as a basis function for reconstruction:

$$R_2(F, \lambda) = \lambda \int \int \int \left(\frac{\partial^2 F}{\partial x^2} \right)^2 + \left(\frac{\partial^2 F}{\partial y^2} \right)^2 + \left(\frac{\partial^2 F}{\partial z^2} \right)^2 dx dy dz \quad (3.2)$$

In order to deal with anisotropic characteristics we extend Equation 3.2, so that we can achieve a different regularization in each direction.

$$R_3(F, \lambda_x, \lambda_y, \lambda_z) = \int \int \int \lambda_x \left(\frac{\partial^2 F}{\partial x^2} \right)^2 + \lambda_y \left(\frac{\partial^2 F}{\partial y^2} \right)^2 + \lambda_z \left(\frac{\partial^2 F}{\partial z^2} \right)^2 dx dy dz \quad (3.3)$$

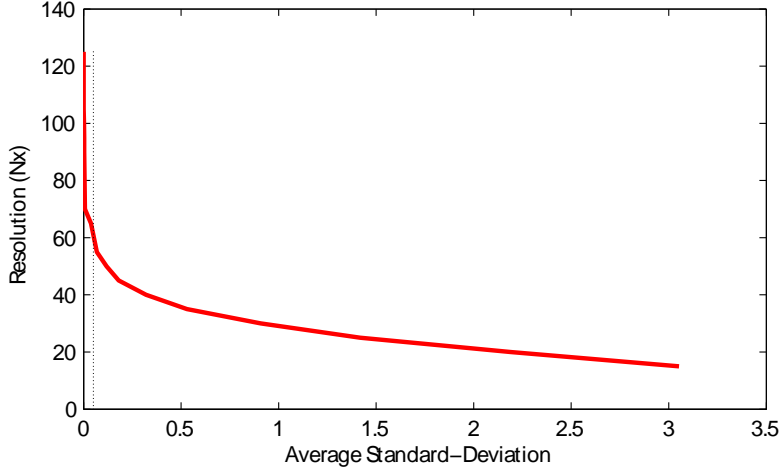
Equation 3.3 provides a very good application scenario in cases when we have apriori knowledge of the directional variance of the data we are reconstructing. A high variance in the x-direction for example, means we should set a lower λ_x and vice-versa. As opposed to Duchon's seminorms, the regularization terms introduced in Equation 3.2 and Equation 3.3 do not enjoy the rotational invariance property.

3.3 Results

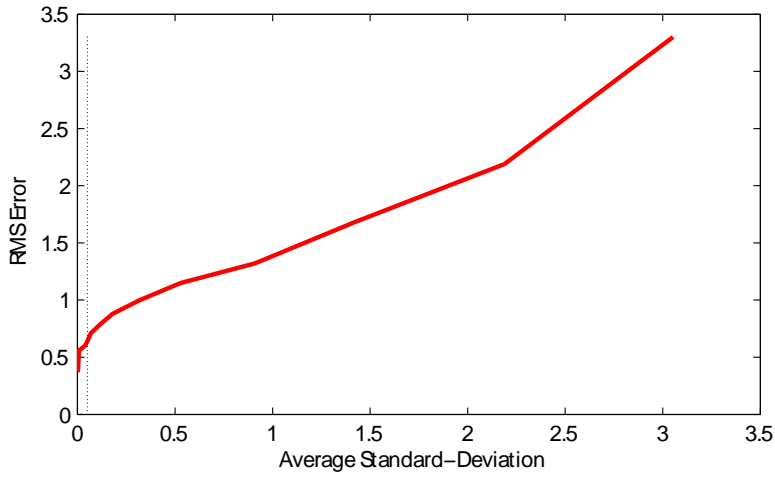
We tested our framework on several data either given from originally non-uniform data, or obtained by taking Laplacian points from a uniform dataset. A GPU-based raycaster is employed for single resolution rendering. The renderer is developed inside the VolumeShop platform [21]. The rendering integral is evaluated at each point along the ray by using Equation 2.6. On the fly gradient estimation is used by taking partial derivatives of the function defined in Equation 2.6 and applying the fact that the derivative of a B-spline of degree n is a B-spline of degree $n - 1$ [104]. It can be defined as follows:

$$\frac{\partial \beta^n(x)}{\partial x} = \beta^{n-1}\left(x + \frac{1}{2}\right) - \beta^{n-1}\left(x - \frac{1}{2}\right) \quad (3.4)$$

In order to determine an appropriate resolution for a uniform grid representation of our non-uniform data points, we would ideally vary the value of N_x , reconstruct using this resolution and measure the error. N_y and N_z are determined by the proper aspect ratio of our underlying axis-aligned bounding box enclosing the given non-uniform data points. Unfortunately, this is computationally infeasible, since we would have to explicitly reconstruct the data. However, in the search for a good heuristic, we did indeed reconstruct a number of test data sets under various resolutions. Then we measured the RMS error of the point set as well as the average variance of point values (as opposed to the reconstruction error) in



(a)



(b)

Figure 3.2: Graphs showing the correlation of σ_{avg} to the: a) resolution of reconstruction, and b) to the respective RMS error. A threshold of $\sigma_{avg} = 0.05$ is shown with a vertical line.

each cell, according to Equation 3.1. The resulting relationship for the Natural Convection dataset can be seen in Figure 3.2. We found a similar relationship in all test data sets. A complete listing can be found in the end of the section (see Figure 3.6 and Figure 3.7)

From Figure 3.2 we can analyze the behavior of σ_{avg} . When we increase the resolution, the number of non-uniform points per cell is decreased, hence decreasing the variance of the cell. A low cell-variance results in a better approximation

capability from the B-splines, hence a lower RMS error. Based on this analysis, we suggest, that a value of $\sigma_{avg} = 0.05$ yields a low RMS. In order to use this effectively for an unknown data set, we start from a low value of N_x and increase it until the value of σ_{avg} falls below the desired value. σ_{avg} monotonically decreases with the increase of resolution. Typically we double N_x in each step, using $N_x = 8$ as a starting resolution. Once σ_{avg} has a value lower than the specified threshold we refine the exact value of N_x with a binary-search method. Arigovindan et al. [10] suggested a heuristic such that the number of uniform points is 4-5 times the number of non-uniform points (i.e., $N_x \cdot N_y \cdot N_z \approx 5 \cdot M$). With our heuristic, on the other hand, we sometimes find $\approx 4 \cdot M$ to be good enough.

Table 3.1 compares the reconstruction results with our new regularization functional to the results obtained using the regularization based on Duchon’s semi-norms. We used uniform data, computed and thresholded their Laplacian to keep 20% of the original points and reconstructed the complete uniform data set from this sparse representation. While computational times remain the same, we observe a 20%-60% improvement in the reconstruction error compared to the results shown in Chapter 2. For our new regularization functional (Equation 3.2) we use $\lambda = 0.3$, while in the previous chapter the results are obtained by using Duchon’s regularization and $\lambda = 1.0$ (for consistency reasons with the results from our previous work [111]). The comparison of the behavior of our reconstruction method for the two different regularization functionals is given in Figure 3.3.

Table 3.1: RMS_g errors and computation times (in minutes) for different non-uniform datasets created by taking 20% of Laplacian points from their original uniform representation.

Dataset		RMS _g and Times (min)	
Name	Size	Laplacian Regularization	Duchon’s Regularization
Engine	256x256x128	0.94 1.28	2.24 1.28
Tooth	256x256x160	0.18 1.88	0.23 1.88
CT-Head	256x256x224	1.17 2.60	2.93 2.60
CT-Chest	394x394x240	0.60 5.08	1.31 5.08
Carp	256x256x512	0.25 5.73	0.50 5.73

Table 3.2 compares our method to the work presented by Jang et al. [47, 48]. Our method has lower reconstruction errors and improves computation times by several orders of magnitude. We show further visual comparison results at the end of the section in Figures 3.8, 3.9 and 3.10. Our approach makes it possible

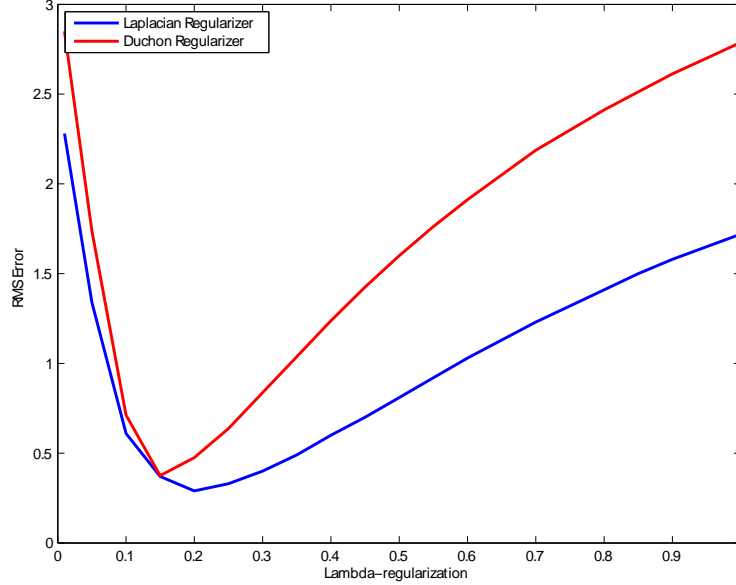


Figure 3.3: Performance of our reconstruction method for varying λ in two different regularization functional. The testing was performed with the Bypass dataset.

to render images of better quality and does not suffer from the blobby artifacts present in the images obtained using the RBF and EBF-based methods.

Table 3.2: RMS errors and computation times (in minutes) for different non-uniform datasets for our approach and the methods proposed from Jang et al. [47, 48]. The ratio column shows by how much percent the size of the dataset was reduced (compressed). The resolutions in our approach are selected based on the $\sigma_{avg} = 0.05$ threshold.

Dataset			RMS and Times (min)		
Name	Resolution	Ratio	Our method	RBF [48]	EBF [47]
Oil	38x40x38	50	0.19 0.07	1.02 1.10	1.08 0.21
Natural Convection	61x61x61	17	0.63 0.07	1.51 6.95	1.41 4.16
Synthetic Chirp	64x64x64	12	1.12 0.08	3.06 229	1.37 36.4
Bypass	766x92x192	57	0.61 6.40	3.38 3987	3.33 3889
Blunt-Fin	93x36x25	49	1.14 0.12	1.58 6.83	1.41 5.38

For all point sets in Table 3.2 we have computed the error only at the points used for the reconstruction (the input-points). However, an important measure is the

quality of the reconstruction at other locations as well. For the original non-uniform datasets the ground truth is not given, hence is difficult to evaluate. Instead we took a Laplacian dataset and reconstructed it on the original grid resolution. In Figure 3.4 we show such a scenario using the Laplacian points from the Tooth dataset. We compute the errors at the non-uniform points used for the reconstruction as well as at all the original uniform data points. While our approach has the same error rates in both cases, the techniques of Jang et al. [47, 48] exhibit a significant increase in the reconstruction error at the non-input points, which is quite visible.

In Figure 3.5 we show the original Synthetic Chirp dataset, our reconstruction with a regularization term as defined in Equation 3.2 and our reconstruction with a directional regularization term as defined in Equation 3.3. The function representing the Synthetic Chirp dataset is changing very fast in the xy plane (the screen plane), while it is changing very slowly along the z axis. In order to reduce the reconstruction error a lower smoothness control along the xy plane is required. All three cases were reconstructed on a $64 \times 64 \times 64$ grid, selected based on the $\sigma_{avg} = 0.05$ threshold. There is a clear improvement in the visual quality when directional regularization is used; the error is reduced by 54%.

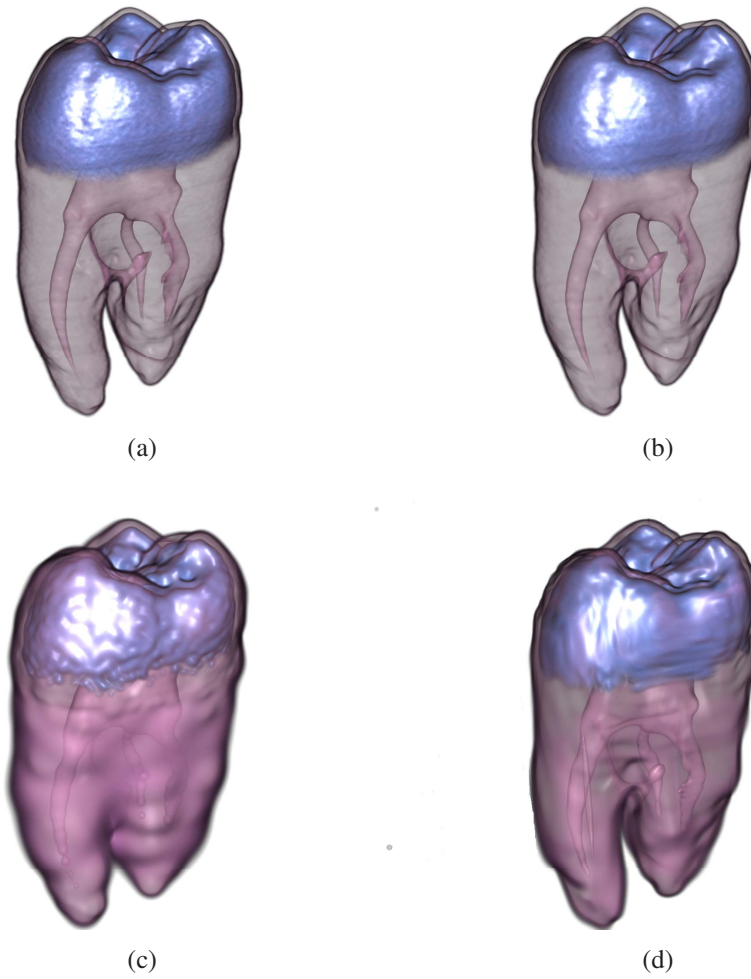


Figure 3.4: Renderings of the Tooth dataset: a) original uniform dataset, b) reconstruction from 2,110,259 non-uniform points using our method. The resolution of reconstruction is selected to be the same as in the original $256 \times 256 \times 160$ dataset. The RMS error is 0.19 at the input points, and 0.18 at the entire uniform volume, c) reconstruction from the same set of input points using RBFs. The RMS error is 1.26 at input points, and 2.87 for the entire volume, and d) reconstruction from the same set of input points using EBFs. The RMS error is 0.76 at input points, and 2.45 at the entire uniform volume.

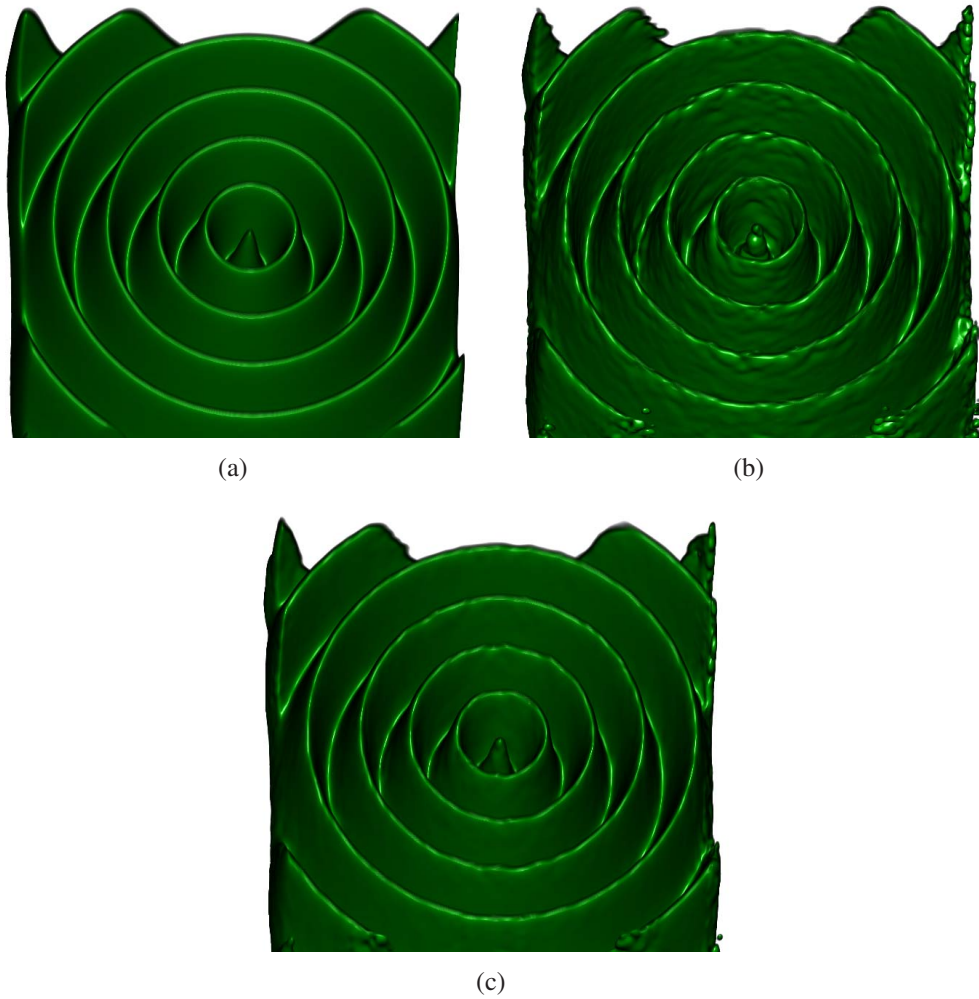


Figure 3.5: Renderings of the Chirp dataset: *a)* the original uniform data, *b)* reconstruction from 75,000 non-uniform points using regularization as defined in Equation 3.2 ($\lambda = 0.3$), RMS is 1.12 with a reconstruction time of 0.08 min, and *c)* reconstruction from 75,000 non-uniform points using regularization as defined in Equation 3.3 ($\lambda_x = \lambda_y = 0.3$, $\lambda_z = 1.0$), RMS is 0.51 with a reconstruction time of 0.08 min.

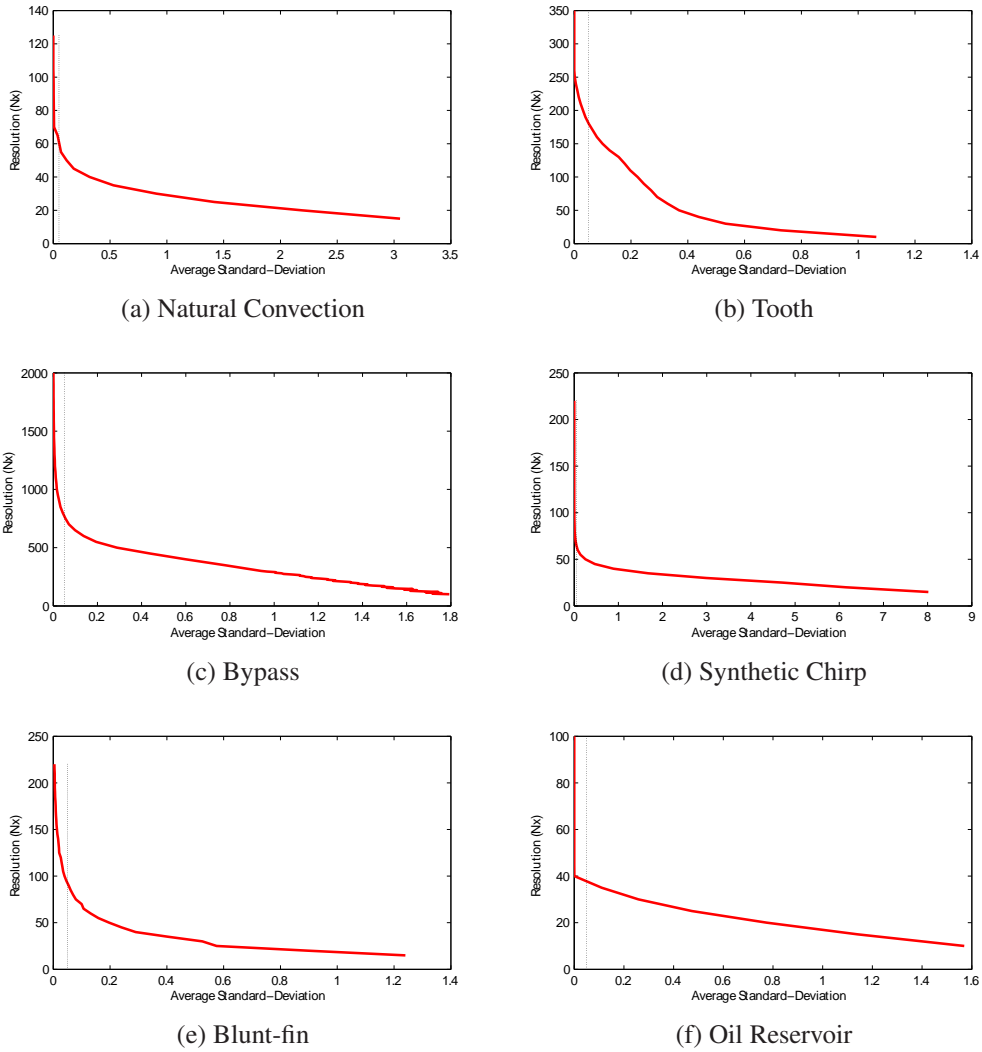


Figure 3.6: The relation of resolution of reconstruction vs. average standard deviation σ_{avg} as computed in Equation 3.1 for several non-uniform datasets. A threshold of $\sigma_{avg} = 0.05$ is shown with a vertical line.

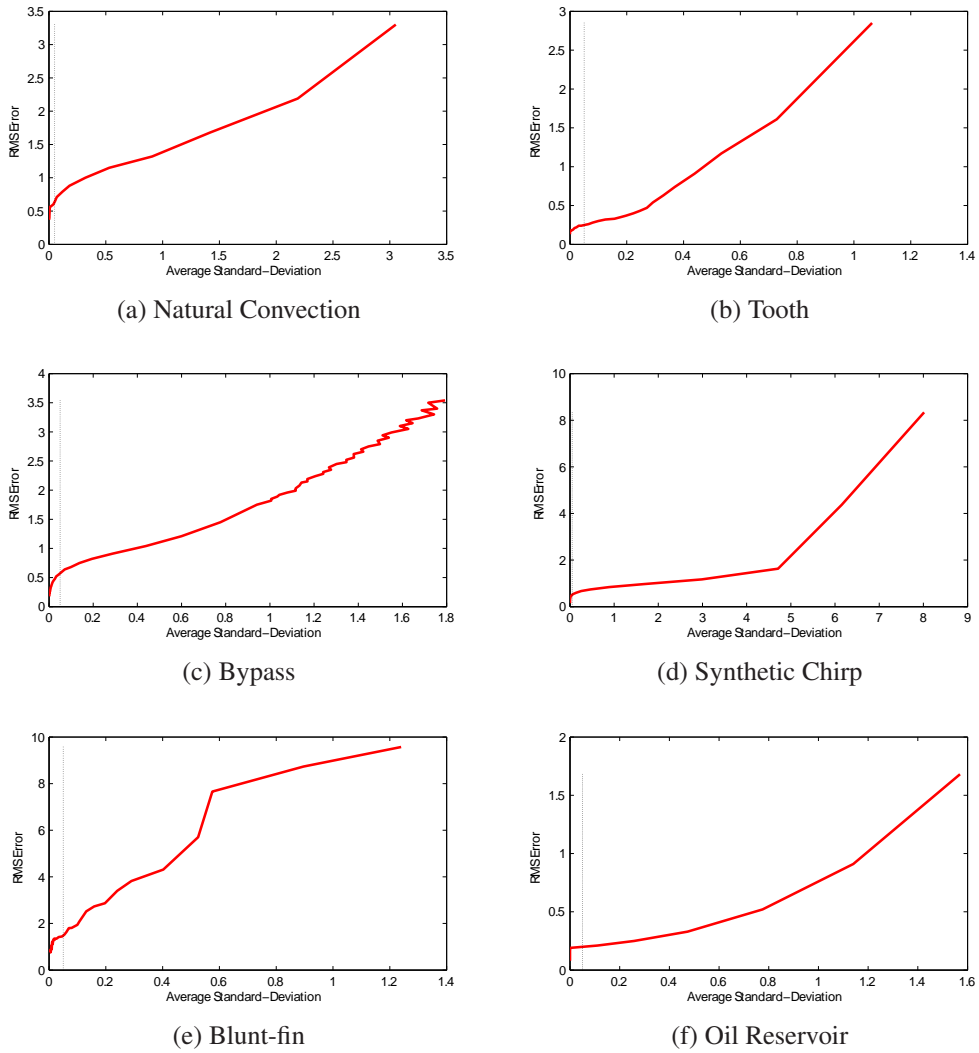


Figure 3.7: The relation of RMS as computed in Equation 1.3 vs. the average standard deviation σ_{avg} as computed in Equation 3.1 for several non-uniform datasets. A threshold of $\sigma_{avg} = 0.05$ is shown with a vertical line.

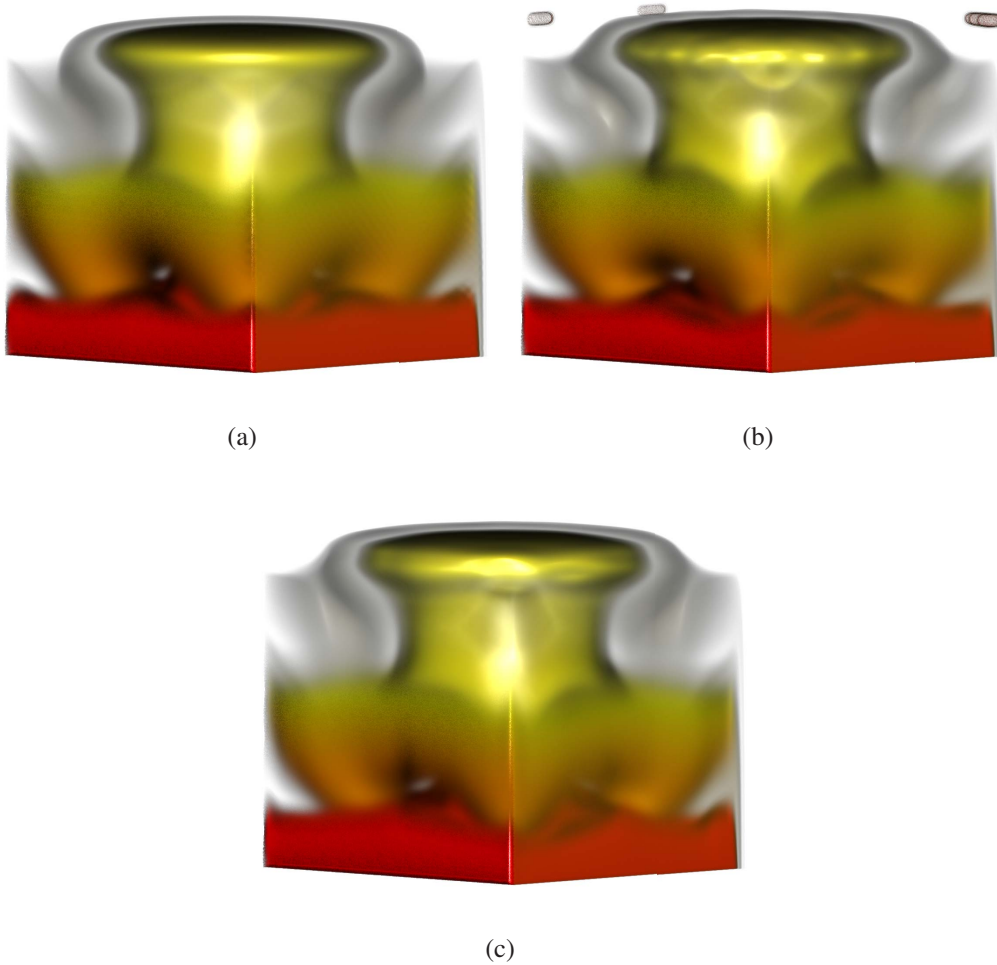


Figure 3.8: Renderings of the Natural Convection dataset: a) reconstruction using our method, RMS is 0.63, b) reconstruction using RBFs proposed by Jang et al. [48], RMS is 1.51, and c) reconstruction using EBFs proposed by Jang et al. [47], RMS is 1.41.

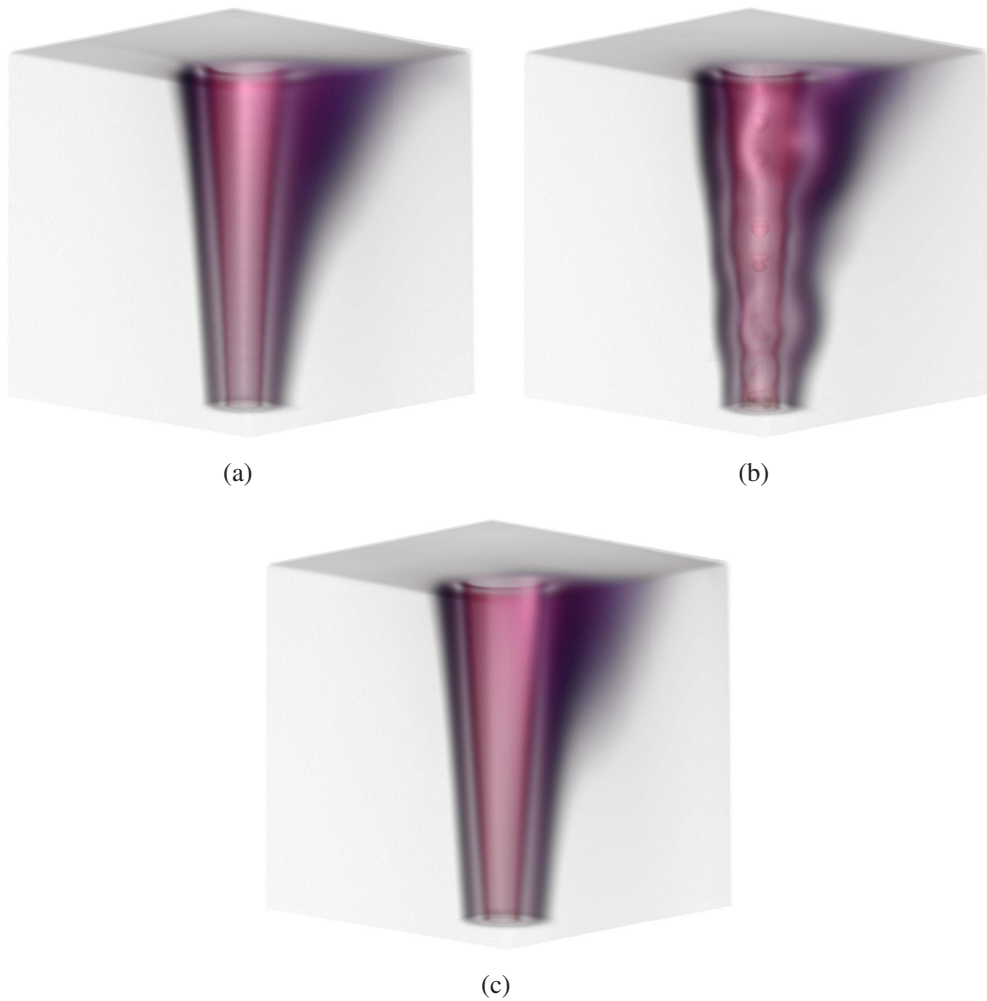


Figure 3.9: Renderings of the Oil Reservoir dataset: a) reconstruction using our method, RMS is 0.19, b) reconstruction using RBFs proposed by Jang et al. [48], RMS is 1.02, and c) reconstruction using EBFs proposed by Jang et al. [47], RMS is 1.08.

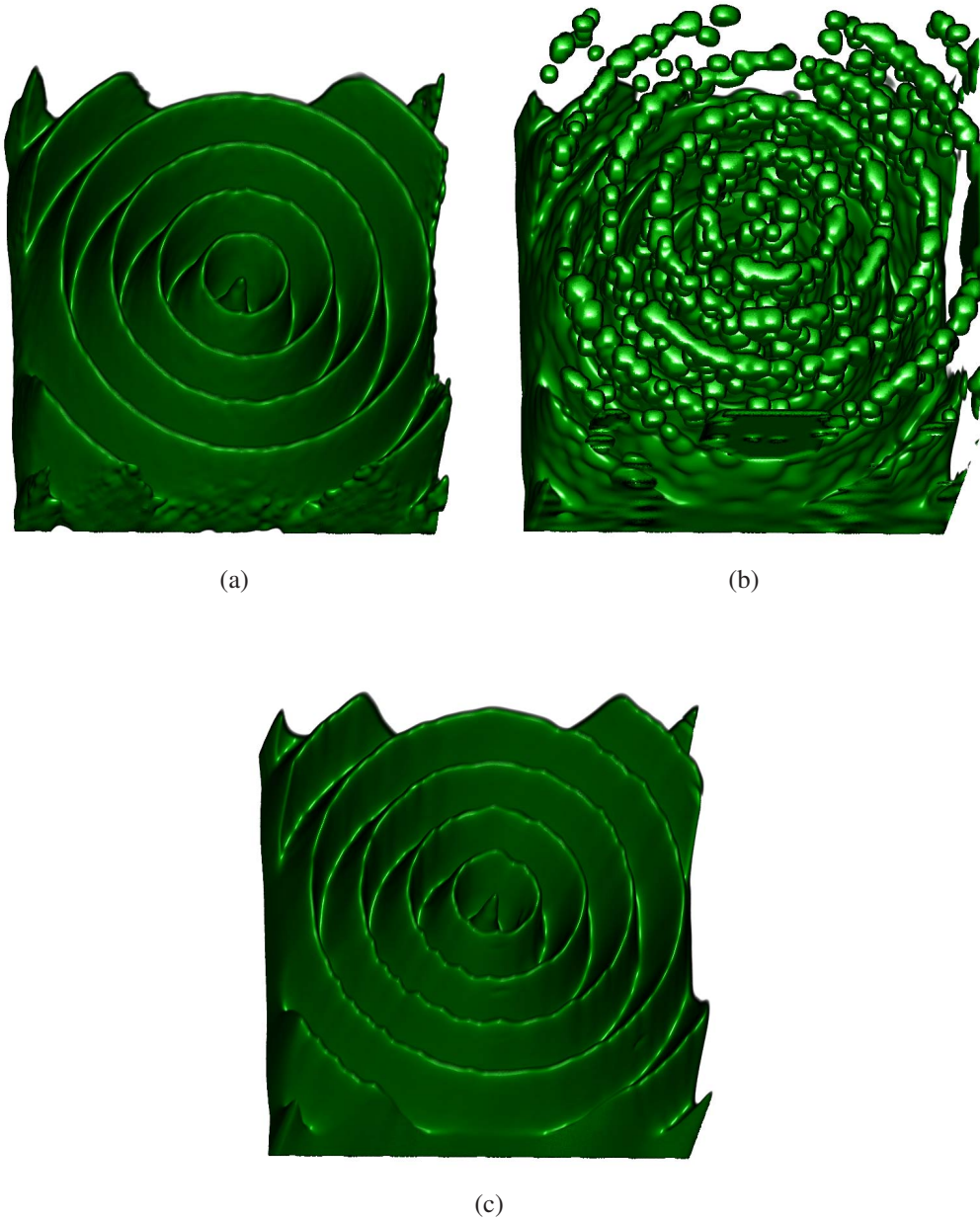
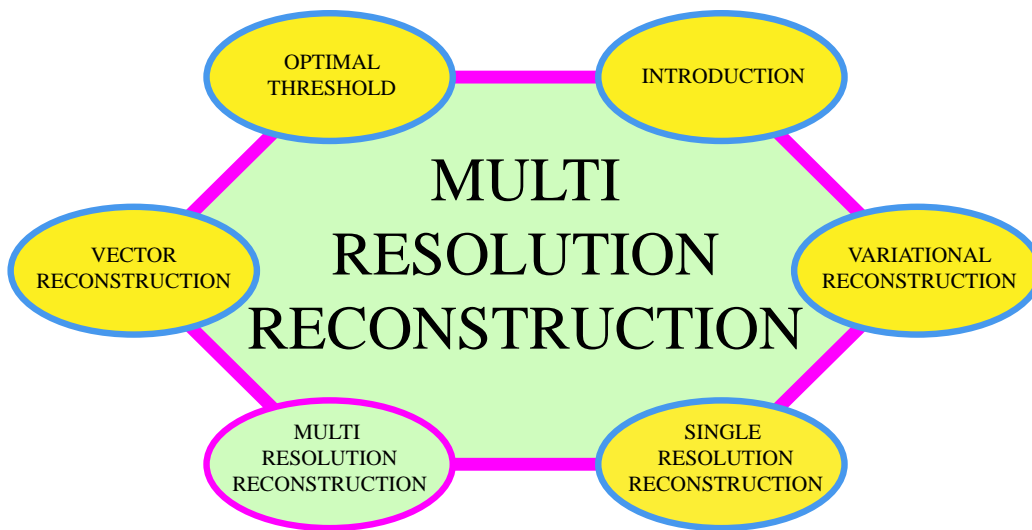


Figure 3.10: Renderings of the Synthetic Chirp dataset: a) reconstruction using our method, RMS is 1.12, b) reconstruction using RBFs proposed by Jang et al. [48], RMS is 3.06, and c) reconstruction using EBFs proposed by Jang et al. [47], RMS is 1.37.

It is possible to fail in many ways, while to succeed is possible only in one way.

Aristotle



There are many scenarios where we observe a large variance in the density of the data points. Hence, finding a single resolution to minimize the error in a uniform representation leads to very large data sets with lots of redundancy. In such a case, it is typical to encode the data with a multi-resolution representation. A multi-resolution function can generally be decomposed into a coarse resolution part, and into a collection of detail coefficients at different resolution levels, necessary to recover the original function. In this chapter we propose two multi-resolution schemes to tackle this problem.

CHAPTER 4

MULTI-RESOLUTION RECONSTRUCTION

One reason for non-uniformity is the ability to capture different scales of information density. There are many scenarios where we observe a large variance in the density of the data points. Hence, finding an optimal resolution, as proposed in Chapter 3, to minimize the error in a uniform representation would lead to very large data sets with lots of redundancy. In such a case, it is typical to represent the data in a multi-resolution pyramid. Our B-spline basis is anchored on a regular grid, preventing the need to store the grid geometry explicitly and opening the door for efficient multi-resolution representations. B-splines have been previously used for multi-resolution reconstruction of one- or two-dimensional signals in a wavelet style [26, 59].

Multi-resolution approaches have been introduced to improve the rendering speed as well as the quality of the data representation adaptively while minimizing the memory overhead [88]. Generally, the visual importance of the local data points is based on the distance to the viewer or other user-selected criteria. These criteria can be intrinsic properties such as temperature, pressure, velocity and so on. Cignoni et al. [27] propose a multi-resolution technique for rendering tetrahedral meshes with scattered vertices obtained from any 3D data. Lamar et al. [56] present an adaptive multi-resolution rendering technique based on a hierarchical octree scheme. Kähler et al. [52] adopted the multi-resolution octree scheme to adaptive mesh refinement trees. Linsen et al. [62] as well as Entezari et al. [31] propose a multi-resolution approach using wavelet concepts and alternate lattices. Wavelets provide a very suitable framework for multi-scale signal processing, hence many approaches related to wavelets are dedicated to multi-resolution analysis [5, 15, 98, 113].

The proper continuous interpolation between different octree levels has remained a challenge in multi-resolution volume rendering. Weiler et al. [116] as

well as Beyer et al. [17] minimize rendering artifacts between block-boundaries by overlapping data blocks. Ljung et al. [64] propose a multi-resolution interblock interpolation that permits extreme changes in resolution across block boundaries. Wang and Shen [114] present a level-of-detail (LOD) map for improving LOD quality by taking into account distortions and contributions from multi-resolution data blocks as a formulation of entropy. Several of the proposed approaches ensure only a C^0 continuity in their rendering algorithms [17, 64]. The multi-resolution function in our approach is a hierarchical sum of C^2 continuous functions, ensuring the C^2 continuity over the entire domain.

Based on the data structure, multi-resolution schemes can be divided into regular schemes [56] (e.g., octrees) and irregular schemes [52] (e.g., adaptively refined meshes). Regular schemes are desirable for fast rendering due to their explicit structure, but are not efficient in representing data when very different resolutions of refinement are required. Irregular schemes have higher data adaptivity but are less suitable for fast rendering. Staadt [97] presents a survey on irregular and regular schemes. We propose one regular scheme, namely bottom-up multi-resolution pyramid (BMRP), and one hybrid multi-resolution scheme, namely adaptive multi-resolution reconstruction (AMR), in an effort to reconstruct the non-uniform point sets efficiently and without losing details of the data. Our hybrid multi-resolution scheme adopts concepts from both classes. It is a multi-level hierarchy where the first level represents the coarse resolution and has a regular representation. Additional levels encode the errors and are refined adaptively. The structure of the refined cells is again regular.

4.1 Bottom-up Multi-resolution Pyramid

In research it is often needed to visualize the same data on different scales. In such cases it is typical to encode the data with a multi-resolution pyramid. One usually starts with the highest resolution and gradually finds coarser representations. To tackle this problem we propose a multi-resolution scheme based on the interscale relation of the B-splines of odd degree (see Section 2.3.2).

We consider a 3D signal approximated through the function $F^{(j)}$ at scale j and represented by a set of coefficients $c^{(j)}$ (see Equation 2.14). Using results from multi-resolution analysis, the same signal can be represented at a finer scale $(j - 1)$ by the coefficients $c^{(j-1)}$, which are obtained by first upsampling $c^{(j)}$ and then filtering with $h(k)$. In the same fashion, by using the inverse transform of Equation 2.13 we can filter and downsample the $c^{(j)}$ to get a projection of these coefficients to the space spanned by the coarser coefficients $c^{(j+1)}$. For a specific scale j we denote the upsampling and downsampling process by the matrices U_j and D_j respectively.

We initially estimate the coefficients at the finest resolution and then process them to create a top-down hierarchy of coarser resolutions. We obtain the coefficients of the coarser resolution ($j + 1$) by downsampling from the finer resolution (j): $c^{(j+1)} = D_j c^{(j)}$. Ignoring the finer resolution completely would create an error at scale (j), i.e., $e^{(j)} = c^{(j)} - U_j c^{(j+1)}$. By saving the coarser scale coefficients and also part of the error volumes (where the error is high) we can reconstruct the data at a finer resolution with little or no error.

For example, for a signal which we want to reconstruct with the finest resolution of $N_x \times N_y \times N_z$, using three levels of hierarchy, we first estimate the finest coefficients $c^{(0)}$ by minimizing Equation 2.7. Then, by using the interscale relation we estimate $c^{(1)}$ and $c^{(2)}$, as well as $e^{(0)}$ and $e^{(1)}$. In our scheme we save only $c^{(2)}$ and parts of $e^{(0)}$ and $e^{(1)}$, which we denote by $e_p^{(0)}$ and $e_p^{(1)}$. When visualizing the data, we can either use the coefficients $c^{(2)}$ for a coarse resolution representation, or the approximations $\tilde{c}^{(1)} = U_1 c^{(2)} + e_p^{(1)}$ or $\tilde{c}^{(0)} = U_0 \tilde{c}^{(1)} + e_p^{(0)}$ for a finer resolution representation.

Our bottom-up multi-resolution pyramid requires an explicit intermediate representation of the finest resolution, which might not be feasible computationally. Hence, we propose a novel algorithm to build an adaptive multi-resolution data structure.

4.2 Adaptive Multi-resolution Reconstruction

Whenever σ_{avg} demands a resolution that is too large to handle directly, we decide to create a multi-resolution representation starting from a coarse resolution first. This prevents us from having to compute the highest resolution explicitly and gives the opportunity to create an adaptive multi-resolution reconstruction algorithm.

Estimating a reasonable coarse resolution is typically tied to hardware constraints. One should not choose a very high resolution, such that it compromises real-time rendering or analysis performance, yet, it should not be too coarse to avoid storing too many levels in the hierarchy. We call this maximum resolution N_{max} . Next, we determine whether each cell of the coarse resolution should be subdivided or not, i.e., whether it is composite or not. This is done based on an error criterion. These steps applied recursively will create a multi-resolution hierarchy, that adapts to the variance in the data. What follows is pseudo-code outlining this algorithm as well as the procedure how to use the multi-resolution hierarchy to determine the value of the function. We will use the notation introduced in Chapter 2 and 3.

Algorithm 1 starts by determining the resolution of the volume V (line 1). This is done based on the σ_{avg} threshold. In order to create a balanced tree, the chosen resolution cannot exceed a maximum resolution N_{max} . Given a resolution we can

Algorithm 1: $c_V^{(j)} = \text{AMR}(\text{Volume } V, \text{ point set } P_V \text{ with values } f_V, \text{ level } j)$

```

1 determine the resolution N for volume V ( $\leq N_{\max}$ );
2 determine the B-spline representation  $F_V$  with coefficients  $c_V$ ;
3 forall cells U of grid V do
4   | estimate reconstruction error  $\epsilon_U = F_V - f_V$  of all points  $P_U$  inside the
   | cell U;
5   | if ( $\epsilon_U$  is too large) AND ( $|P_U| > \tilde{M}$ ) then
6   |   |  $c_U^{(j+1)} = \text{AMR}(U, P_U \text{ with values } \epsilon_U, \text{ level } j + 1)$ ;
7   | end
8 end

```

Algorithm 2: Evaluate Function F_V at (x, y, z) for Volume V

```

1 evaluate  $F_V(x, y, z)$  by using coefficients  $c_V$ ;
2 if  $(x, y, z)$  is in composite cell U then
3   | evaluate Function  $F_U$  at  $(x, y, z)$  for Volume U;
4   | return  $F_V(x, y, z) + F_U(x, y, z)$ ;
5 else
6   | return  $F_V(x, y, z)$ ;
7 end

```

then determine the B-spline coefficients c_V for this resolution using Equation 2.7 (line 2). For each cell of this resolution, we will determine whether we should recursively subdivide (line 5). This is based on the cell reconstruction error (computed in line 4) as well as whether the number of points in the cell is above a threshold \tilde{M} . \tilde{M} is used to prevent the algorithm from subdividing cells with a low number of points inside. Once we determine that we should subdivide the given cell, we only reconstruct the error function ($F_V - f_V$) in line 6.

Algorithm 2 is used during the raycasting process. It chooses the B-spline coefficients to use in Equation 2.6 accordingly. If the point is in a composite cell, it recursively adds the error estimation of each level of the hierarchy.

4.3 Results

In order to implement our BMRP scheme we need to find an error threshold, that determines which detail coefficients to keep. In our experiments we found that keeping 20% of the coefficients with the highest error in each level is a good trade-off between storage overhead and accuracy. Although these error coefficients can

be anywhere in the volume, they are still located on a uniform grid. Hence, using a run-length encoding data-structure [19], we found that for 20% of the points of a uniform dataset we need approximately 40% of the storage required for the entire uniform dataset.

In Figure 4.1 we show timestep 360 from the Bypass dataset (focusing on the "bypass" process, i.e., the creation of vortex-shape structures) reconstructed with our BMRP approach. There is a visible difference in the level of detail in the different resolutions. The file size for saving $c^{(2)}$, $e_p^{(0)}$, and $e_p^{(1)}$ altogether is 49% of the size of the non-uniform dataset. Analyzing the plot results of the relation of the RMS error to the percentages of $e^{(0)}$ and $e^{(1)}$, we observe a drastic change in the errors in the 20% region. In Figure 4.2 we show the relation of the RMS error to the percentages of $e^{(0)}$ and $e^{(1)}$, justifying to keep only 20% of the error coefficients in each level.

To visualize the multi-resolution hierarchy created from our AMR algorithm we have adapted our CPU-based raycaster to implement Algorithm 2, which takes all resolution levels into account during rendering.

One of our main concerns is the continuity or smoothness preservation through different levels of resolution. Since each level of the hierarchy is C^2 continuous and we are simply adding these levels, the final result remains a C^2 continuous function. In order to avoid discontinuities at the boundaries, we extend the borders of the cells in each direction by a specific number of voxels of value zero (here the voxel size depends on the resolution of the cell). We take into consideration the finite support of cubic B-splines. Extending by two voxels in each direction ensures that the function representing the cell smoothly goes to zero as it approaches these extended borders and is zero-valued everywhere beyond them.

Taking into consideration rendering performance a suitable choice of N_{\max} could be 8, 16, or 32. In fact, in our experiments we chose 32 for the initial level, but experimented with different N_{\max} for the subsequent levels. The decision whether a cell has to be refined is based on the reconstruction error of that cell (see line 5 in Algorithm 1). The RMS error threshold is always set to 1.0. In order to prevent the subdivision of cells with only few non-uniform points we set $\tilde{M} = 100$.

The X38 Vehicle dataset consists of 323,192 non-uniform points emulating the X38 Crew Return Vehicle. It is a typical non-uniform dataset where 99% of its points are concentrated in about 5% of the volume. In Figure 4.3 we show the dataset reconstructed with our multi-resolution scheme consisting of two levels. Due to the aspect ratio of the axis-aligned bounding box, the coarse resolution is $32 \times 23 \times 17$ with an RMS of 6.39.

Table 4.1 summarizes several scenarios we tested to analyze the behavior and performance of our AMR method. In all cases we specify the coarse resolution to be 32, i.e., for the X38 and Bypass data set this translates to an initial dataset of

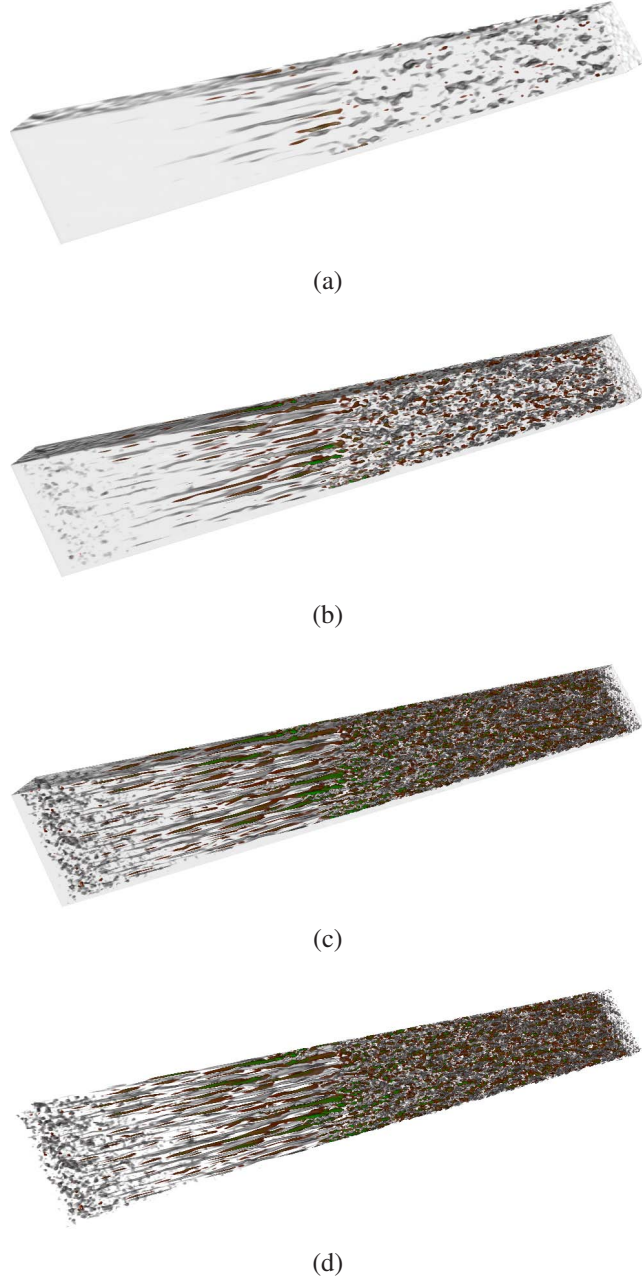


Figure 4.1: Renderings of the Bypass dataset reconstructed using our BMRP scheme (finest resolution $1024 \times 120 \times 256$): a) coarse representation reconstructed from $c^{(2)}$ coefficients, RMS is 4.55, b) finer representation reconstructed from $\tilde{c}^{(1)} = U_j c^{(2)} + e_p^{(1)}$, where we used 20% of the points from the $e^{(1)}$ error volume, RMS is 2.69, c) finest representation reconstructed from $\tilde{c}^{(0)} = U_j \tilde{c}^{(1)} + e_p^{(0)}$, where we used 20% of the points from the error volume $e^{(0)}$, RMS is 0.6, and d) finest representation reconstructed where we used 100% of the points from the error volumes $e^{(0)}$ and $e^{(1)}$, RMS is 0.4.

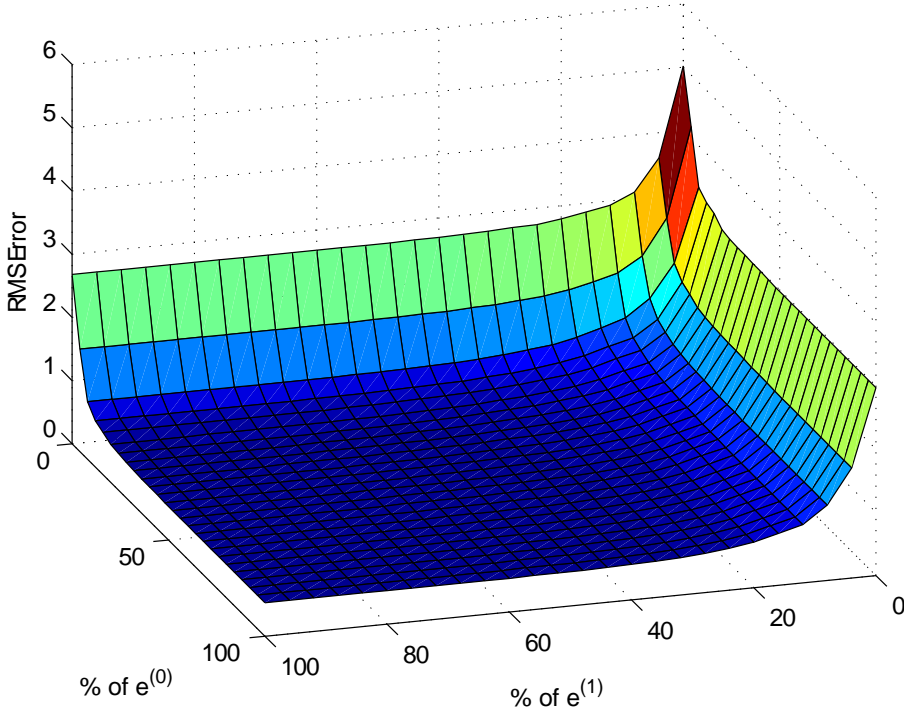


Figure 4.2: Graph showing relation of RMS to the percentages of $e^{(0)}$ and $e^{(1)}$ for the Bypass dataset.

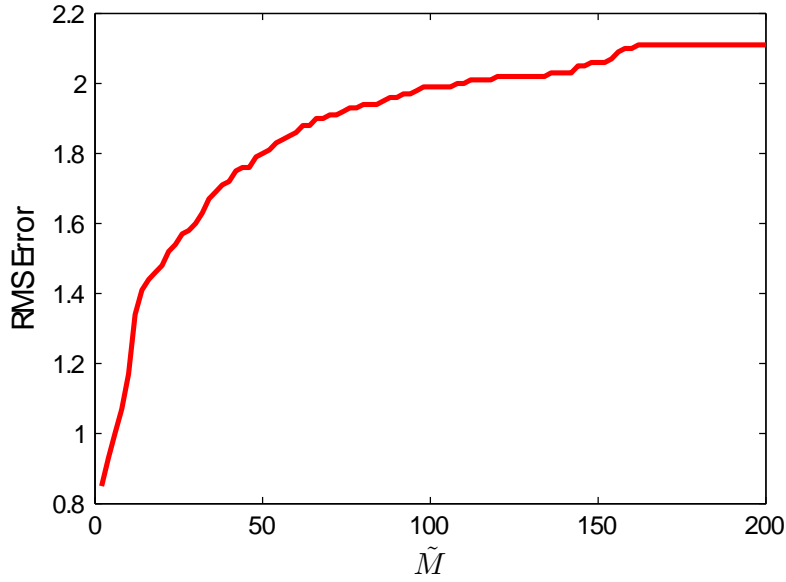
$32 \times 23 \times 17$ cells and $32 \times 5 \times 9$ cells, respectively. Level one represents the coarse data details, while the other levels represent the finer details. Since there is no subdivision in level one, the entries for Error, Times and Size in Table 4.1 are the same for the respective datasets. In the second and third level, we selected either $8 \times 8 \times 8$, $16 \times 16 \times 16$ or an adaptive resolution based on the $\sigma_{avg} = 0.05$ threshold, to subdivide (refine) the composite cells. The number of refined cells in level two depends on the threshold \tilde{M} . A small value of \tilde{M} results in more refined cells, and vice-versa. Using a resolution of 8^3 requires more levels in order to capture the data accurately, however, the storage per level is reduced. By using a resolution of 16^3 or an adaptive resolution we increase the storage requirement per level, but achieve a better approximation of the data. The number of cells that the data is subdivided when a $16 \times 16 \times 16$ or adaptive subdivision is used is greater than in the $8 \times 8 \times 8$ subdivision case. Furthermore, the number of cells that will qualify for refinement in the next level will be lower for the $16 \times 16 \times 16$ and adaptive case, since there will be fewer cells that have the number of points higher than \tilde{M} . When using the adaptive resolution the impact of the third or higher levels in the

reconstruction error is very small. For the Bypass dataset there is no refinement in level three for the $16 \times 16 \times 16$ and adaptive case, since no cell has an error and number of points higher than 1.0 and \tilde{M} , respectively.

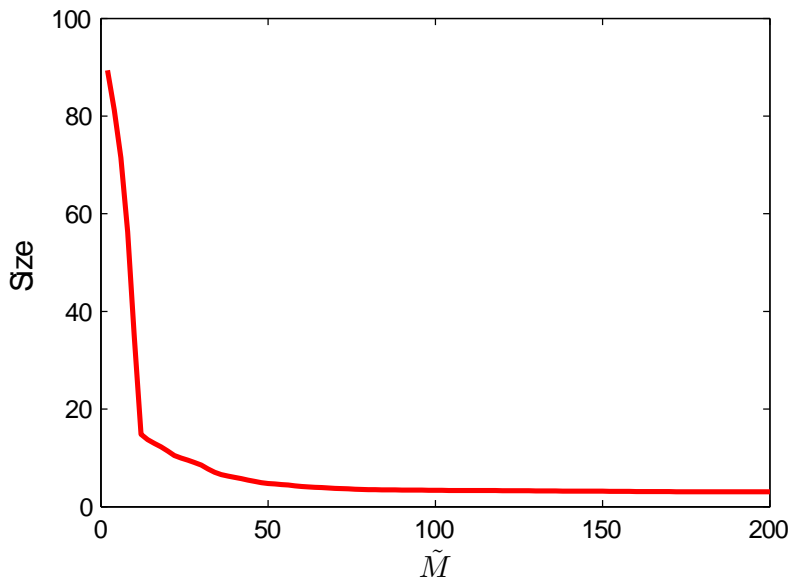


Figure 4.3: The X38 Vehicle dataset consisting of 323,192 non-uniform points rendered with our multi-resolution scheme using two levels of hierarchy.

In addition we also analyzed the impact of the threshold \tilde{M} . In Figure 4.4 we show graphs that give the relation of \tilde{M} to the reconstruction error and to the storage required for the multi-resolution hierarchy. Lowering the \tilde{M} threshold, lowers the error, but increases the storage requirements drastically. Driven also from the results of Figure 4.4, $\tilde{M} = 100$ is selected as a trade-off between accuracy and storage requirements.



(a)



(b)

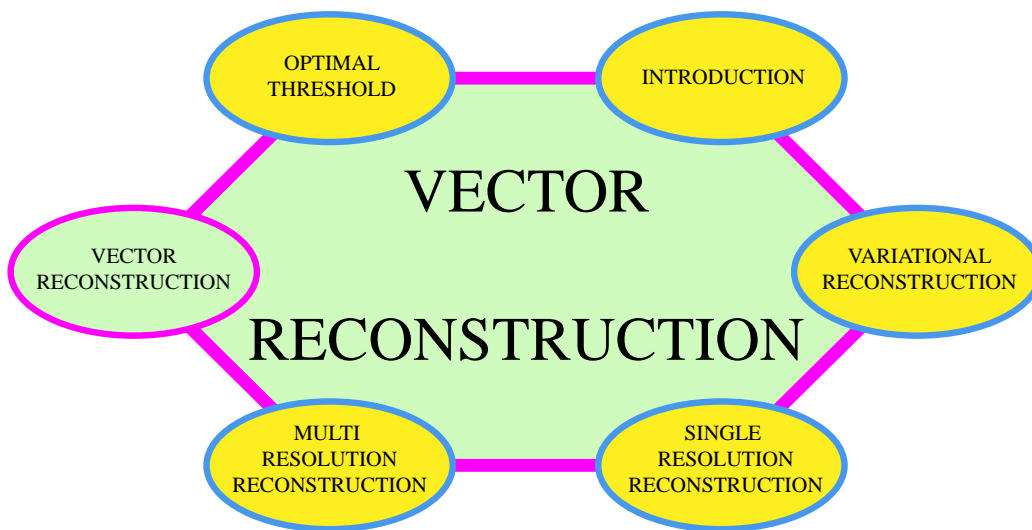
Figure 4.4: Graphs showing the impact of \tilde{M} on the: a) RMS error, and b) storage requirements for storing the multi-resolution hierarchy dataset (in MB). Testings are performed with X38 Vehicle dataset and an adaptive resolution is used for the subdivision of the cells in level two.

Table 4.1: AMR results for different datasets and settings. Size shows the storage requirements in MB, Sub shows the resolution of reconstruction of the composite cells (i.e., either fixed or selected adaptively (*adp*) based on the $\sigma_{avg} = 0.05$ threshold), \tilde{M} is the minimum number of points for which a cell can be subdivided, Cells is the number of composite cells in each level of the hierarchy and Times are in minutes.

		Dataset Name								
Level	Feature	X38			Bypass			X38		
	Size	5.11	5.11	5.11	121	121	121	5.11	5.11	5.11
	Sub	8^3	16^3	<i>adp</i>	8^3	16^3	<i>adp</i>	<i>adp</i>	<i>adp</i>	<i>adp</i>
	\tilde{M}	100	100	100	100	100	100	50	10	1
One	RMS	6.39	6.39	6.39	4.33	4.33	4.33	6.39	6.39	6.39
	Times	0.03	0.03	0.03	0.52	0.52	0.52	0.03	0.03	0.03
	Size	0.05	0.05	0.05	0.01	0.01	0.01	0.05	0.05	0.05
Two	Cells	136	136	136	938	938	938	183	427	787
	RMS	2.66	1.67	1.60	2.41	0.79	0.34	1.59	1.33	1.30
	Times	0.07	0.17	0.52	1.22	1.72	7.53	0.55	0.58	0.63
	Size	0.27	2.13	3.14	1.84	14.66	58.91	3.32	3.58	3.88
Three	Cells	1765	651	33	13270	-	-	292	7535	17948
	RMS	1.99	1.60	1.58	1.54	-	-	1.55	0.97	0.75
	Times	0.27	0.58	0.03	1.95	-	-	0.25	5.03	12.43
	Size	3.46	10.18	0.18	25.99	-	-	1.37	28.63	81.60

The most exciting phrase to hear in science, the one that heralds new discoveries, is not "Eureka!" but "That's funny ..."

Isaac Asimov



In this chapter we extend the concepts of the variational reconstruction to non-uniform vector data reconstruction. We introduce a component-wise vector reconstruction method. We test our algorithm with non-uniform vector datasets obtained either from simulations or from the gradients of uniform datasets. By means of error estimation and vector visualization we show the behavior of our proposed reconstruction technique. The usage of the reconstructed gradients for shading during the rendering process improves the smoothness of the images.

CHAPTER 5

VECTOR RECONSTRUCTION

Vector field reconstruction or simply vector reconstruction is a method of creating a vector field from experimental or computer generated data. A vector field associates a vector to every point in a subset of Euclidean space. Generally, the goal of vector reconstruction is to find a mathematical representation of the data. In turn, this representation can be used for the study and analysis of phenomena, especially in fields related to computational fluid dynamics (CFD).

Initially introduced for the study of magnetic fields in classical field theory, today, vector fields occur in subjects such as tomography, optics, quantum mechanics and medical imaging. Several techniques have been developed for the reconstruction of 2D and 3D vector fields with special focus in tomography reconstruction [13, 40, 41, 45, 84]. Variational methods have also been applied for the reconstruction of vector fields. Bookstein [18] introduces a component-based reconstruction for 2D vector fields. Amodei and Benbourhim [8] address 2D vector reconstruction by using a regularization functional based on the curl and divergence of the vector field. They carry out the reconstruction as a minimization in the second order Beppo-Levi space. Arigovindan et al. [11] present a variational method for the reconstruction of 2D vector fields acquired from Doppler measurements. They use a regularization functional based on Green's semi-norms for the curl and divergence of the vector field. Dodu and Rabut [29] present a variational method for reconstruction of 3D vector fields using radial-basis-like functions.

Laidlaw et al. [55] and Forsberg et al. [36] give a general overview and comparison of 2D and 3D vector field visualization techniques, respectively.

5.1 Problem Formulation and Metrics

The formulation of variational vector reconstruction is very similar to the scalar reconstruction problem introduced in Chapter 2. Given a set of sample positions, $\mathbf{p}_i = (x_i, y_i, z_i)$, $i = 1, 2, \dots, M$, let $\mathbf{f}_i = [f_{u_i} \ f_{v_i} \ f_{w_i}]^T$ be the vector field values associated with \mathbf{p}_i . We denote $\mathbf{v}(x, y, z) = [u(x, y, z) \ v(x, y, z) \ w(x, y, z)]^T$ to be the underlying function of the vector field which approximates the input data.

We want to find a vector field \mathbf{v} such that it best approximates the given vector point set. In order to evaluate the reconstructions obtained from our proposed technique we use different error metrics. In Equation 5.1 we compute the reconstruction error for the u component. The errors for the other two components can be formulated similarly.

$$RMS_u = 100 \cdot \sqrt{\frac{1}{M} \sum_{i=1}^M (u(x_i, y_i, z_i) - f_{u_i})^2} \quad (5.1)$$

While reconstructing vectors, we are interested not only in low RMS errors for the components of the vector, but especially in low RMS errors for the amplitude and the orientation of the vector. In order to estimate the errors for the amplitudes, Equation 5.1 can be reformulated as Equation 5.2. We recall that the vector components are normalized so that the maximum amplitude across the vector point set is 1.0. For the orientation we measure the angle γ between the reconstructed and the input vector as expressed in Equation 5.3. The angle is given in degrees and defined over the interval $[0^\circ, 180^\circ]$.

$$RMS_{\|\mathbf{v}\|} = 100 \cdot \sqrt{\frac{1}{M} \sum_{i=1}^M (\|\mathbf{v}(x_i, y_i, z_i)\| - \|\mathbf{f}_i\|)^2} \quad (5.2)$$

$$E_\gamma = \frac{180^\circ}{M \cdot \pi} \sum_{i=1}^M \cos^{-1} \left(\frac{\mathbf{v}(x_i, y_i, z_i) \cdot \mathbf{f}_i}{\|\mathbf{v}(x_i, y_i, z_i)\| \cdot \|\mathbf{f}_i\|} \right) \quad (5.3)$$

5.2 Component-wise Reconstruction

In the previous chapters we introduced the idea of variational reconstruction and applied it to non-uniform scalar data. In this chapter we apply our variational reconstruction scheme to vector data in a component-wise fashion. We search the solution in the space of uniform B-splines which can be formulated as follows:

$$u(x, y, z) = \sum_{k=0}^{N_x-1} \sum_{l=0}^{N_y-1} \sum_{m=0}^{N_z-1} c_{k,l,m}^u \beta^3(x-k) \beta^3(y-l) \beta^3(z-m) \quad (5.4)$$

where $c_{k,l,m}^u$ are the B-spline coefficients associated with the u component of the vector \mathbf{v} . The other two components are formulated in a similar way. In order to find the coefficients $\mathbf{c}_{k,l,m}$ the following cost function is minimized:

$$C(\mathbf{v}) = \sum_{i=1}^M \|\mathbf{v}(x_i, y_i, z_i) - \mathbf{f}_i\|^2 + \lambda R(\mathbf{v}) \quad (5.5)$$

It is important to note that this regularizer does not have any coupled terms, meaning that it does not enforce any special relationship between velocity components. As a regularization functional we use the Laplacian regularizer introduced in section 3.2 (see Equation 3.2).

In Table 5.1 we show the results from the reconstruction of Laplacian-Gradient datasets. We reconstruct the whole gradient field from 20% of input vector points. We give the reconstruction errors for each component (u , v , w) and for the amplitudes $\|\mathbf{v}\|$, as well as the average angle E_γ (in degrees) for the deviation of the reconstructed vector from the original one. The reconstruction times are given in minutes (min). The errors are computed only for the input points, i.e., if 20% of gradient points are used, then only those are used for estimating the errors. We have denoted the Laplacian-Gradient datasets with a G symbol next to the name of the scalar dataset.

In Table 5.2 we give the reconstruction errors and times for the same datasets as in Table 5.1, but the errors are computed over the whole dataset (including the points discarded from the thresholding process). The amplitude and angle errors are higher when computed over the whole dataset, since the vector field cannot be smoothly reconstructed. For the Engine $_G$ and CT-Chest $_G$ datasets we observe high reconstruction errors. We argue this behavior is based on two factors. First, the number of zero-amplitude vectors for the Engine $_G$ and CT-Chest $_G$ datasets is about 33% and 63% of the total number of vectors, respectively. Furthermore, the bounding box for the non-zero vector points in these two datasets has a resolution of $256 \times 256 \times 111$ and $352 \times 320 \times 240$, respectively. Since there are no input points for reconstructing the vector field in many slices, our reconstruction method has to extrapolate from the neighboring points, resulting in high reconstruction errors on these slices.

In Figure 5.1 we show 2D vector plots of a slice from the Neghip $_G$ dataset. The slice was taken parallel to $y - z$ plane. The displayed 2D projected vector field is the error between the reconstructed vector field and the input vector field. The

Table 5.1: Vector reconstruction errors given as RMS for each component (u , v , w) and for the amplitudes $\|\mathbf{v}\|$, as well as the average angle E_γ (in degrees) for the deviation of the reconstructed vectors from the original ones. Each component is reconstructed separately with $\lambda = 0.3$.

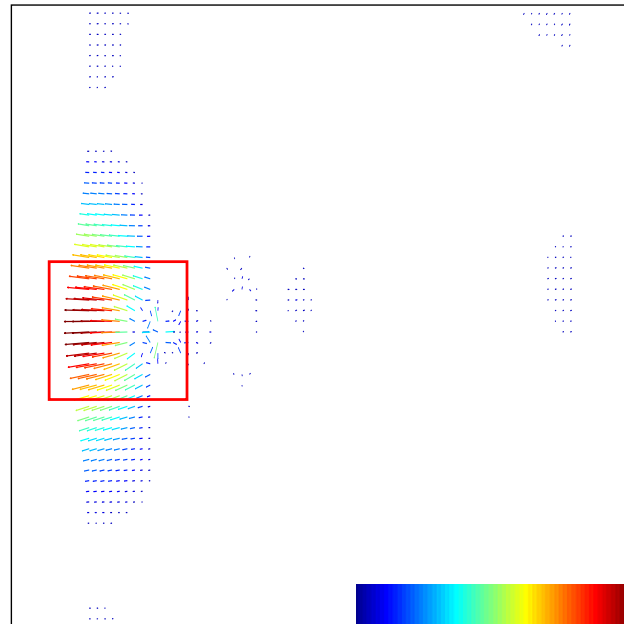
Dataset		Error and Times (min)					
Name	Resolution	u	v	w	$\ \mathbf{v}\ $	E_γ	Times
Neghip _G	64 × 64 × 64	1.65	1.54	1.71	2.31	4.33	0.57
Hydrogen _G	128 × 128 × 128	0.11	0.11	0.11	0.16	3.96	4.67
Engine _G	256 × 256 × 128	0.69	0.65	0.98	1.22	7.21	27.57
Tooth _G	256 × 256 × 160	0.83	0.85	0.82	1.20	13.75	41.93
CT-Head _G	256 × 256 × 224	0.67	0.69	0.61	0.95	6.98	57.68
Aneurism _G	256 × 256 × 256	1.13	1.12	1.10	1.63	1.42	66.23
Bonsai _G	256 × 256 × 256	0.84	0.86	0.64	1.13	7.26	70.83
CT-Chest _G	394 × 394 × 240	0.73	0.77	0.24	0.97	5.51	117.05

Table 5.2: Vector reconstruction errors given as RMS for each component (u , v , w) and for the amplitudes $\|\mathbf{v}\|$, as well as the average angle E_γ (in degrees) for the deviation of the reconstructed vectors from the original ones. Each component is reconstructed separately with $\lambda = 0.3$. The values are computed over the all the points, i.e., estimated at 100% of points.

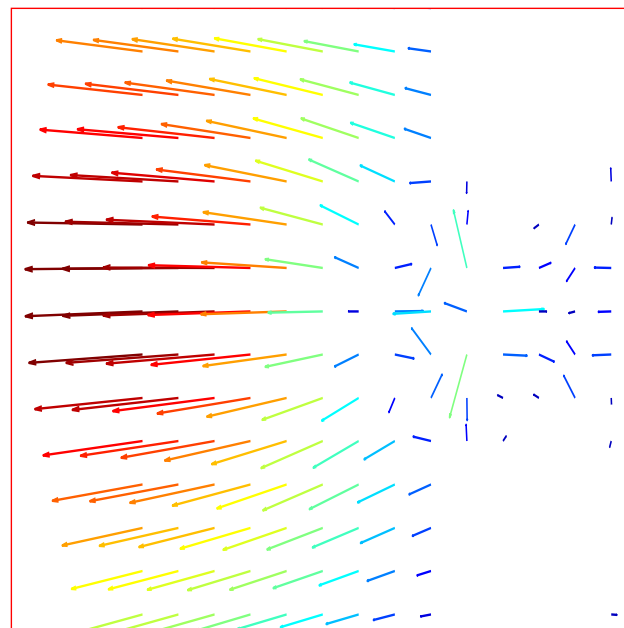
Dataset		Error and Times					
Name	Resolution	u	v	w	$\ \mathbf{v}\ $	E_γ	Times
Neghip _G	64 × 64 × 64	1.74	3.21	2.25	4.21	4.47	0.57
Hydrogen _G	128 × 128 × 128	0.85	2.01	2.00	2.96	3.32	4.67
Engine _G	256 × 256 × 128	1.07	1.05	22.84	22.87	31.64	27.57
Tooth _G	256 × 256 × 160	7.91	7.78	1.03	11.06	19.98	41.93
CT-Head _G	256 × 256 × 224	7.09	7.76	2.77	10.82	42.17	57.68
Aneurism _G	256 × 256 × 256	4.32	4.54	4.11	7.47	0.29	66.23
Bonsai _G	256 × 256 × 256	5.28	8.69	1.67	10.26	4.63	70.83
CT-Chest _G	394 × 394 × 240	20.36	12.92	0.81	24.09	6.55	117.05

vector amplitudes have been magnified 10 times. In Figure 5.1(a) we show only vectors that have an amplitude higher than a user-specified threshold. This was done for visualization purposes. In Figure 5.1(b) we show the selected area from Figure 5.1(b) with a higher resolution.

In Table 5.3 we give reconstruction results from non-uniform vector point sets acquired from simulations. The selection of the reconstruction resolution is based



(a)



(b)

Figure 5.1: 2D vector plot from the *Neghip_G* dataset: a) 2D slice, b) zoomed version of selected area of (a). Vectors with the smallest amplitudes are colored blue and those with largest amplitudes are colored red.

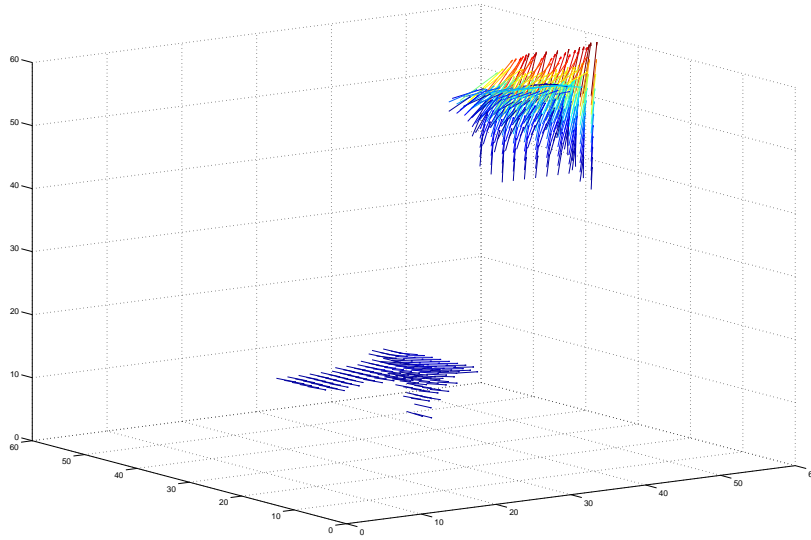
on the σ_{avg} assumption introduced in Section 3.1. In this case σ_{avg} is estimated for the amplitudes of the input vector point set, since the set consisting of the vector amplitudes can be considered as a scalar non-uniform point set.

Table 5.3: Vector reconstruction errors given as RMS for each component (u , v , w) and for the amplitudes $\|\mathbf{v}\|$, as well as the average angle E_γ (in degrees) for the deviation of the reconstructed vectors from the original ones.

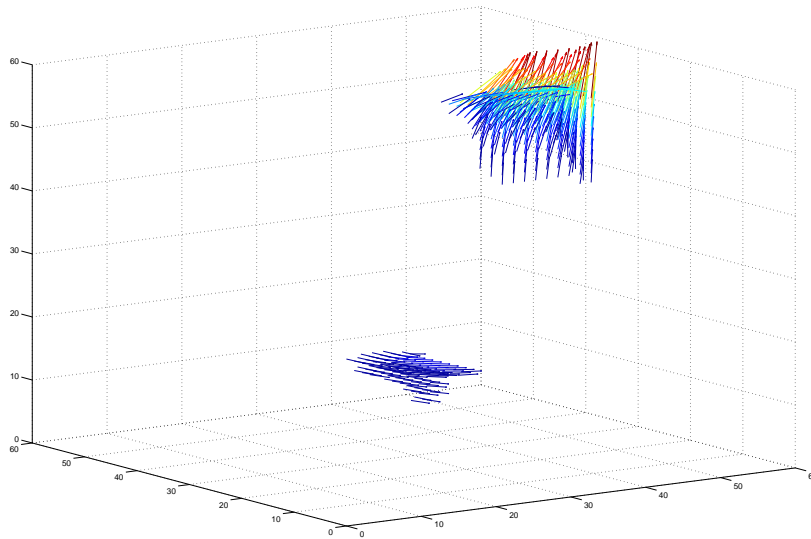
Dataset			Error and Times					
Name	Points	Resolution	u	v	w	$\ \mathbf{v}\ $	E_γ	Times
Flow Transport	17,120	$44 \times 58 \times 58$	0.26	0.70	0.34	0.64	0.91	0.48
Fuel Injection	25,190	$39 \times 51 \times 60$	0.36	0.65	0.62	0.62	0.42	0.50
Cooling Jacket	1,537,898	$222 \times 128 \times 122$	0.95	0.94	1.25	1.30	2.51	9.50

In Figure 5.2 we show the 3D vector plot of the non-uniform input vector point set and the reconstructed point set for the Flow Transport dataset. For visualization purposes we show only those vectors that have amplitudes higher than a user defined threshold and we magnify the amplitudes by 10 times. In Figure 5.3 we show the 3D vector plot of the difference vector field between the datasets shown in Figure 5.2. The amplitudes are 30 times magnified. In Figure 5.4 we show two visualizations from the Flow Transport and Fuel Injection Dataset. We used glyphs and streamlines to visualize the vector fields.

To understand the visual quality of the reconstructions from the Laplacian-Gradient datasets we used them in the rendering process for shading. In Figures 5.5 and 5.6 we show renderings for the Neghip and Engine datasets. In each Figure we have used for shading the gradients computed from the scalar data during the rendering process (Figures 5.5(a) and 5.6(a)), and the gradients reconstructed from the respective Laplacian-Gradient datasets (Figures 5.5(b) and 5.6(b)). The usage of the reconstructed gradients for shading during the rendering process improves the smoothness of the images. By reconstructing the Laplacian-Gradient datasets we assure that the underlying gradient field used for the shading is represented by a C^2 continuous function, hence ensuring visually better looking images.



(a)



(b)

Figure 5.2: 3D vector plot of the Flow Transport dataset: a) input dataset, and b) reconstructed dataset. Vector points are shown in a $44 \times 58 \times 58$ resolution. Vectors with the smallest amplitudes are colored blue and those with largest amplitudes are colored red.

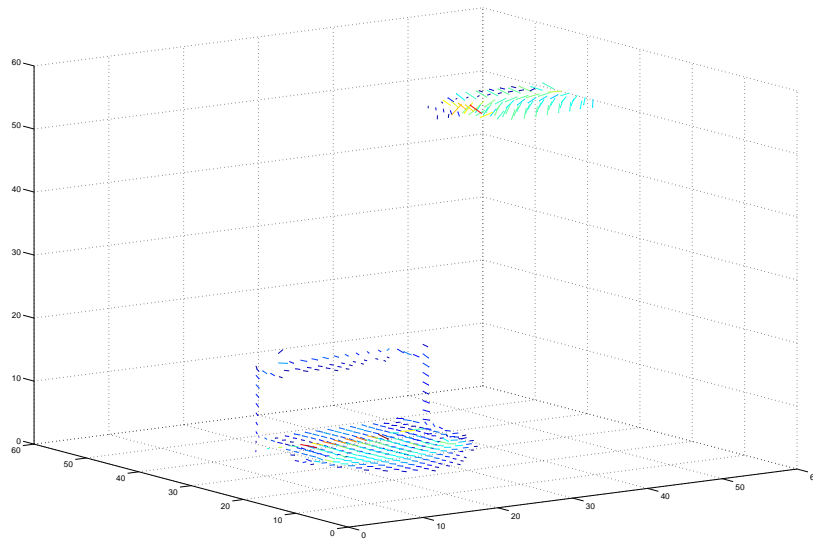
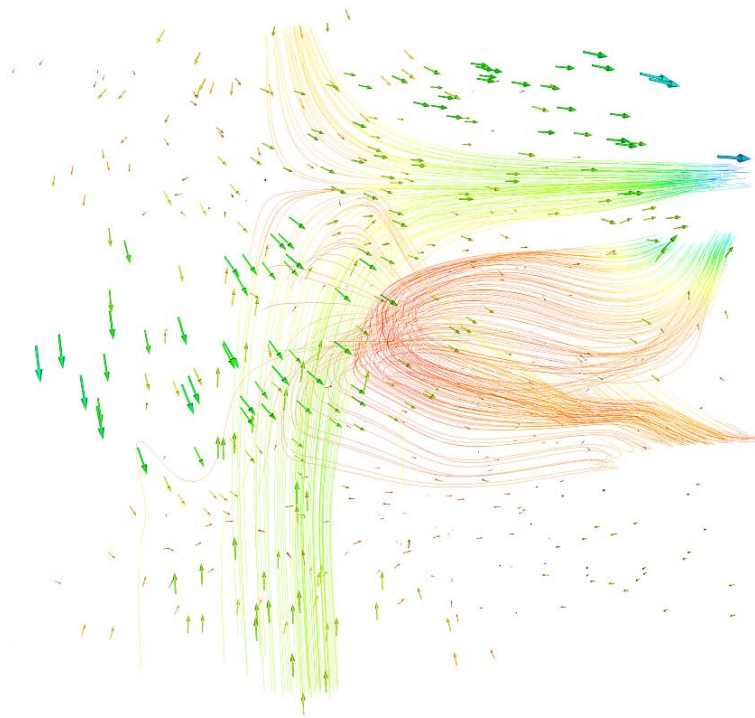
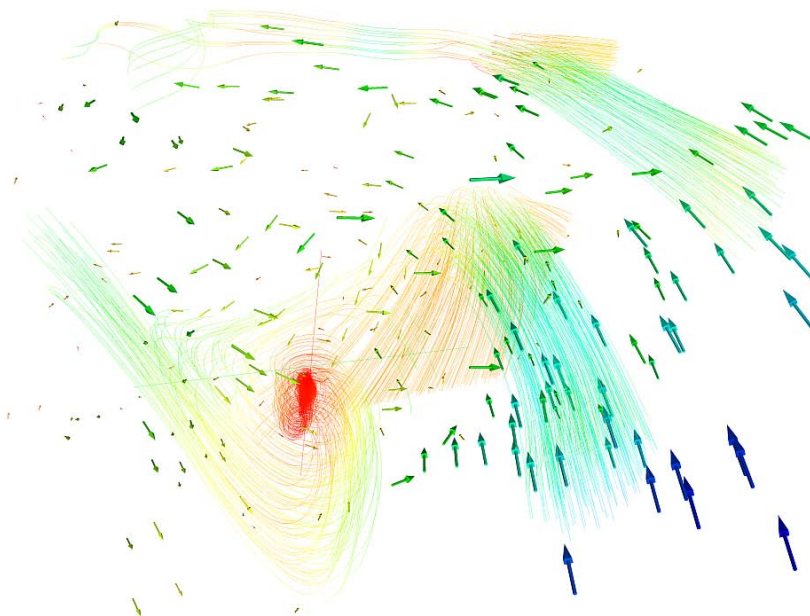


Figure 5.3: 3D vector plot showing the error vector field between the reconstructed and input vector point set for the Flow Transport dataset. Vectors with the smallest amplitudes are colored blue and those with largest amplitudes are colored red.

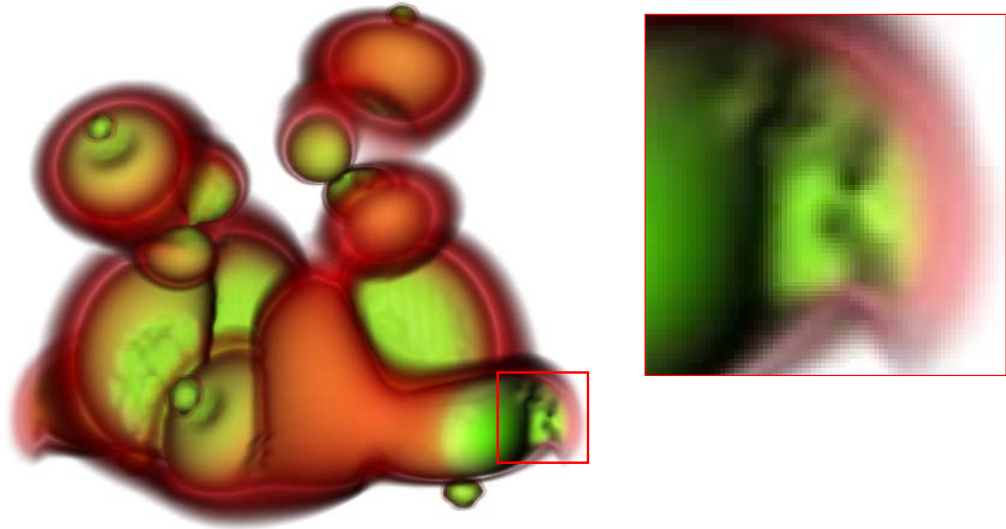


(a)

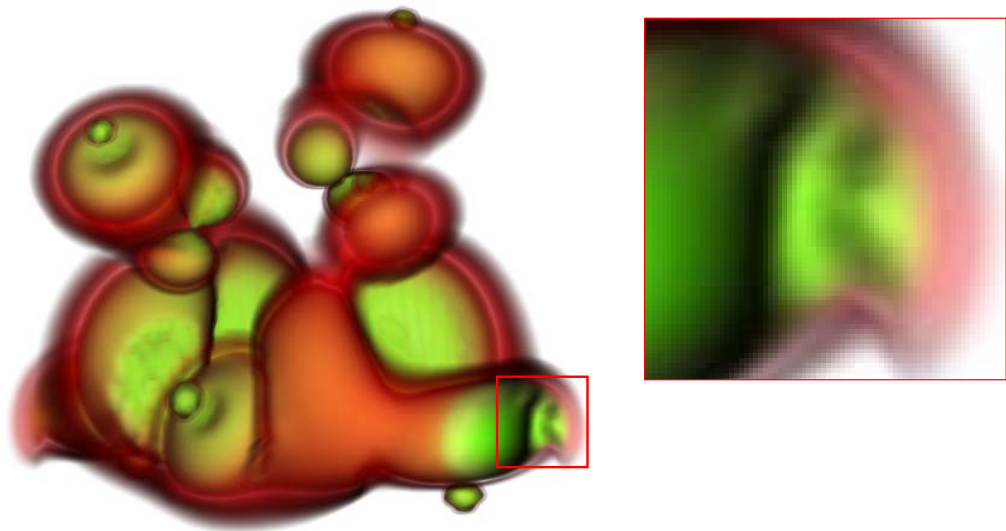


(b)

Figure 5.4: 3D vector visualization: a) the Flow Transport dataset, b) the Fuel Injection dataset. The HSV colorspace has been used for color mapping.



(a)



(b)

Figure 5.5: Renderings of Neghip dataset: a) shading is based on gradients computed from the scalar data, and b) shading is based on the reconstructed gradients from the Neghip_G dataset.

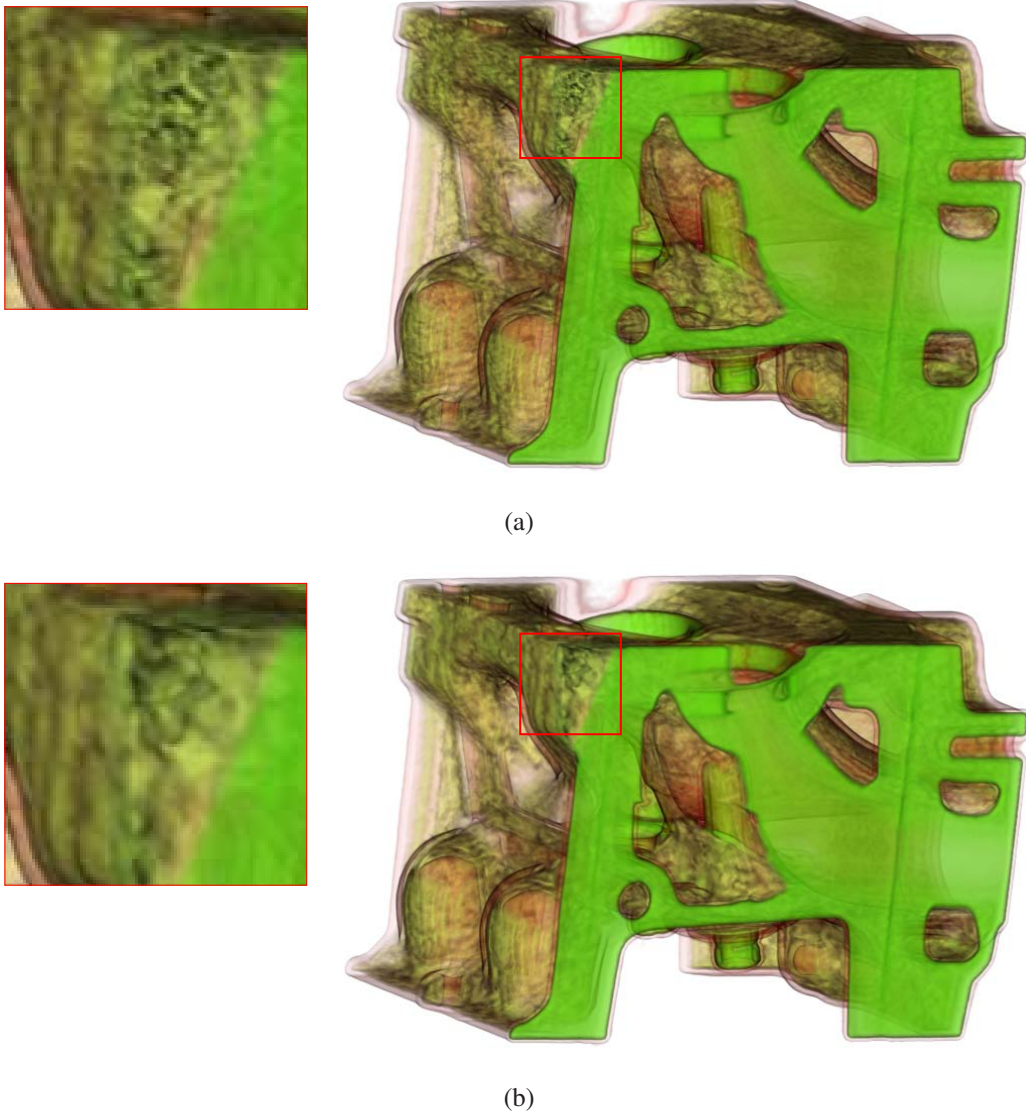
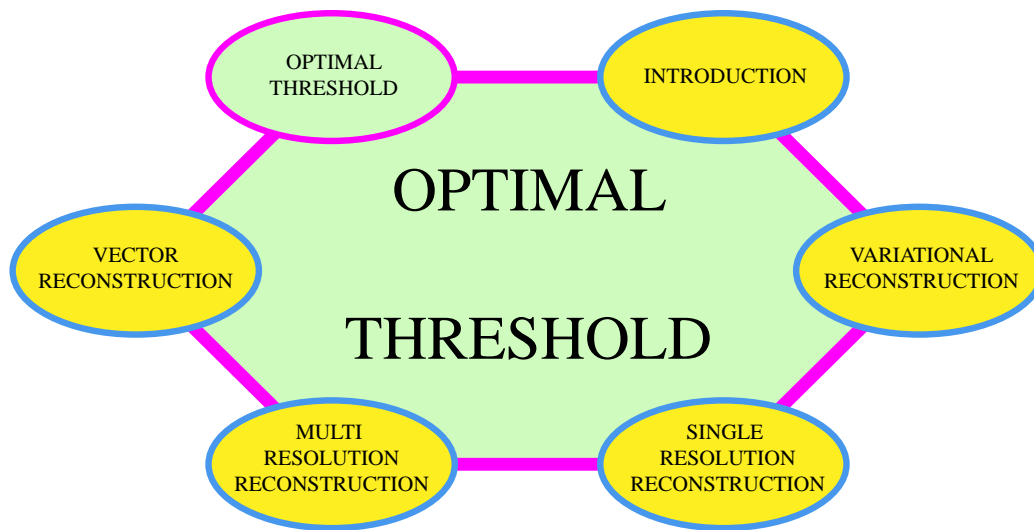


Figure 5.6: Renderings of Engine dataset: a) shading is based on gradients computed from the scalar data, and b) shading is based on the reconstructed gradients from the $Engine_G$ dataset.

*You need chaos in your soul to give birth
to a dancing star!*

Friedrich Nietzsche



In Chapter 1 we introduced the idea of using uniform datasets to produce non-uniform representations by thresholding the Laplacian. We selected the threshold in order to keep 20% of the points. In this chapter we investigate to find an optimal threshold and how to improve the selection of points in order to have lower reconstruction errors. By means of graphs we analyze the behavior of our variational scheme in the reconstruction of Laplacian datasets.

CHAPTER 6

OPTIMAL THRESHOLD

In Chapter 1 we introduced the idea of creating non-uniform datasets thresholding the Laplacian of uniform datasets. We selected 20% of the points from the uniform representation. In the chapters that followed, we showed that this threshold ensured reconstruction with a low RMS error and good visual quality. Although the selection of Laplacian points is not supposed to be a compression technique, keeping only 20% of the points of a uniform representation results in an up to 60% reduction in the storage requirements for the respective data.

6.1 Thresholding the Laplacian

In an attempt to find the optimal threshold we pursued several tests by reconstructing the Laplacian datasets with different percentages of points. The results related to some of the tested datasets are given in Figure 6.1. The results show how the RMS error depends on the number of points selected as input in the reconstruction process. We can see that for the displayed graphs the reconstruction error becomes stable in the interval [15% – 25%]. A similar behavior is observed by all the other tested datasets. From the reconstruction point of view the error does not change (significantly) when we further increase the number of points. This fact is connected with the approximative and non-interpolating property of cubic B-splines. The control points of the B-splines tend to oscillate in accordance with fast changing values of the input points (e.g., edges). In images or volumes edges represent only a small part of the whole data. If we want the further increase of number of points to influence the reconstruction error we have to lower the regularization value λ . As λ approaches zero the variational approach tends to behave as a simple least square approximation.

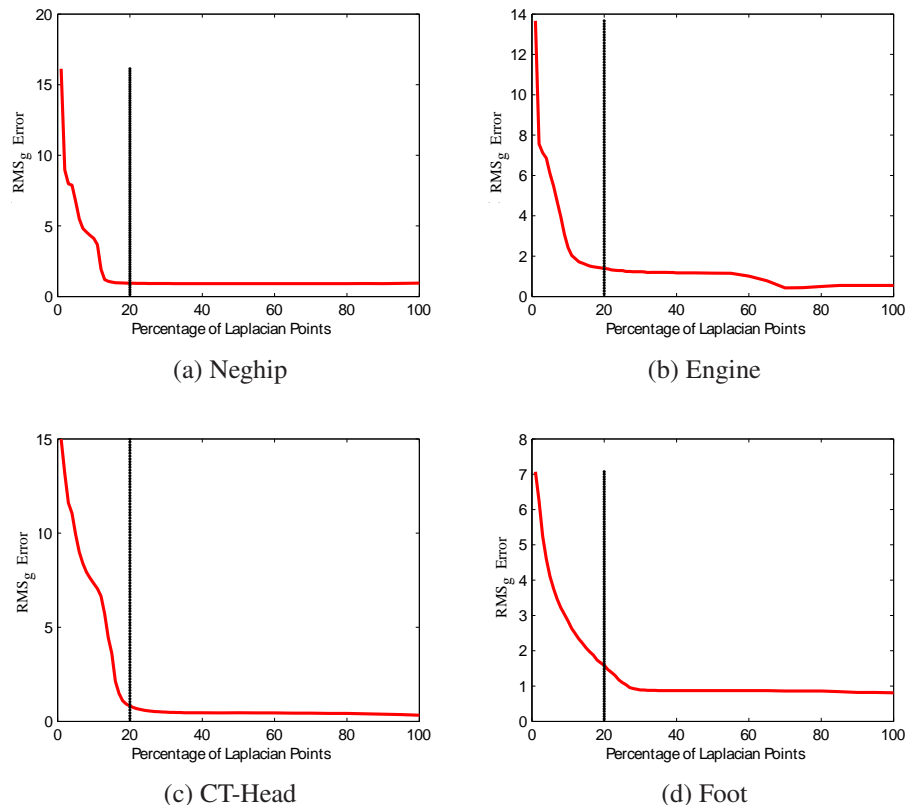


Figure 6.1: The relation of RMS_g vs. percentage of Laplacian points selected as non-uniform data. The results were obtained from our variational reconstruction method using the Laplacian regularizer (Equation 3.2) and $\lambda = 0.3$.

In Figure 6.2(a) we show a typical example from the image processing community. Figure 6.2(b) shows the image after being convolved with the Laplacian kernel and scaled to range $[0, 255]$ (for display purposes). We take the highest absolute values for a Laplacian dataset (the values close to black in the image). It is obvious that these values constitute only a small part of the image. Hence selecting the $[15\% - 25\%]$ threshold interval assures that all important points (i.e. edges) are taken into account. The increase of the threshold would include points from areas with a low variance into the reconstruction process. Hence this would not affect the B-spline coefficients and the reconstruction process.

In Figure 6.3 we show the response of the variational reconstruction error to a changing λ -regularization and percentage of Laplacian points for the Neghip dataset. Figure 6.3(a) gives the RMS_g error estimated for the uniform points of the dataset. The error is high when the percentage of the points in the Laplacian dataset is low, regardless of the λ -regularization. When the percentage of points increases

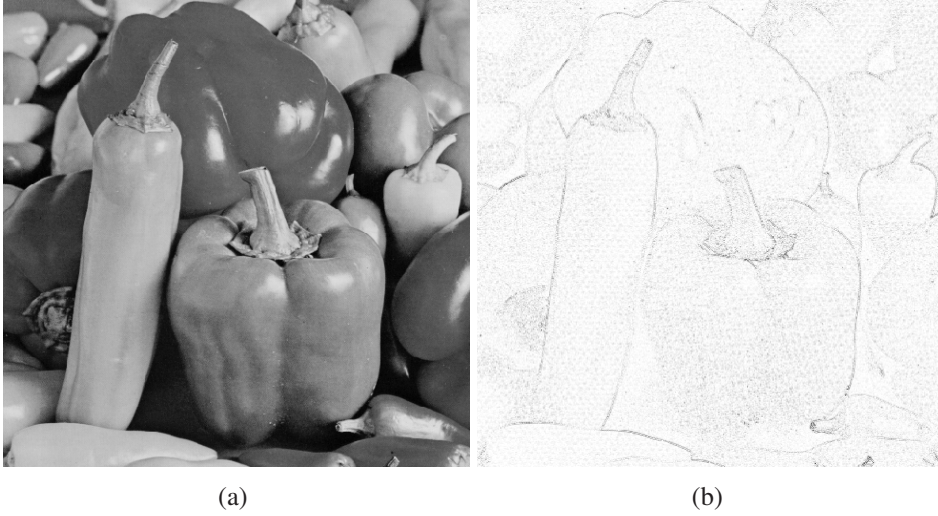
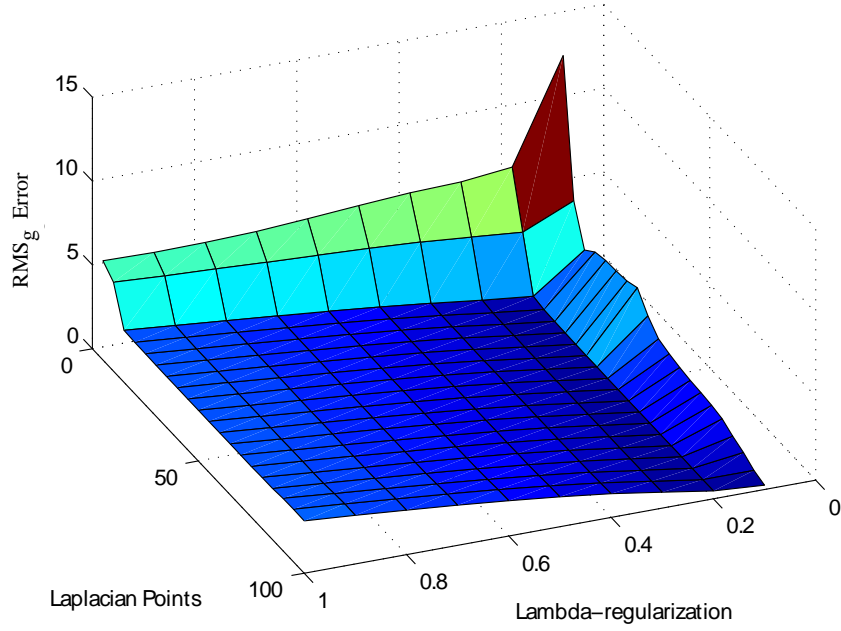


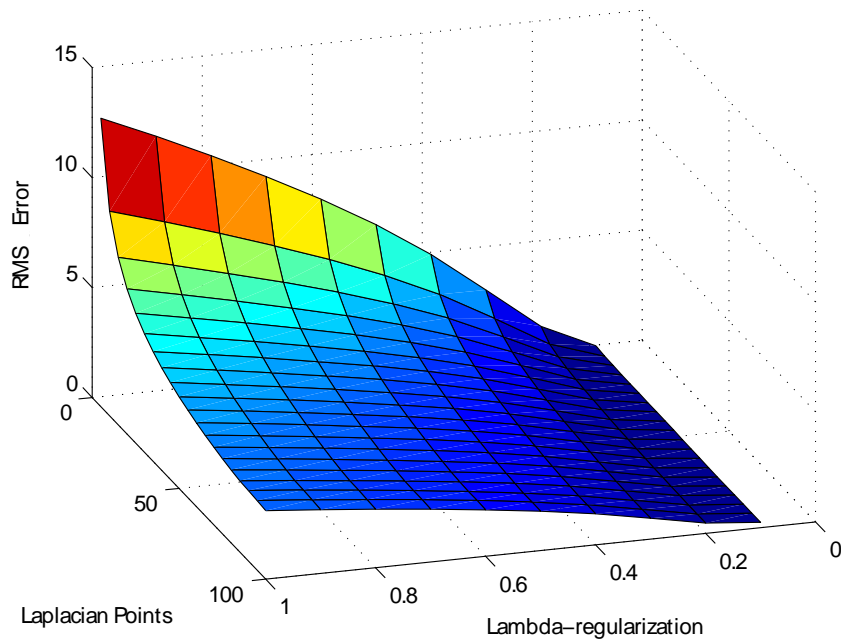
Figure 6.2: Input image (a), and the response after convolution with a Laplacian kernel and scaling (b).

the λ -regularization plays a more important role in the reconstruction. A high λ -regularization means more smoothing and better results when the percentage is low and the gaps between non-uniform points are bigger. A low λ -regularization means less smoothing and better results when the percentage increases over the 25% threshold. Tests with more than ten datasets show that the best results, regarding the reconstruction errors, can be achieved when $\lambda \in [0.2 - 0.3]$ and the percentage of points is in the interval $[15\% - 25\%]$. When λ -regularization is high then the RMS error is high even though we may have a high percentage of Laplacian points. This is due to the strong regularization and its smoothing effects. Figure 6.3(b) gives the RMS error only for the input points present in the Laplacian dataset, hence the reconstruction error is expected to be low when λ -regularization is very small. As λ -regularization goes to zero, the variational approach behaves like a simple least-squares approximation. When the percentage of Laplacian points goes towards 100%, both graphs of Figure 6.3 tend to be similar since they both give the errors over the whole points of the uniform data.

The comparison of the graphs in Figure 6.3 gives us a better insight on the selection of λ -regularization and optimal threshold. An ideal reconstruction method is required to deliver similar reconstruction error rates not only for the input points but also for the whole data domain. From the graphs in Figure 6.3 we see that the zone, where RMS and RMS_g exhibit similar behavior, is for $\lambda \in [0.2 - 0.3]$ and the percentage of points is in the interval $[15\% - 25\%]$. The selection of such a percentage threshold is also reinforced by the visual comparison of the rendered images of the Laplacian datasets reconstructed with different numbers of



(a)



(b)

Figure 6.3: The relation of RMS to the percentage of Laplacian points and λ -regularization.

non-uniform points.

6.2 Iterative Point Selection

When selecting the Laplacian points for creating non-uniform datasets, we stated that other filters could be possible candidates for the point selection. Due to the sensitivity of B-splines to high-frequency details, we advocated that convolution with a Laplacian kernel is the optimal choice. In this section we want to build upon such conclusions, in order to find a representation of points that leads to lower reconstruction errors when used with our variational approach. The idea is to select a specific low-percentage from the Laplacian points, reconstruct the data, and then increment the number of points on those positions where the RMS error is highest. The diagram of this scheme is shown in Figure 6.4.

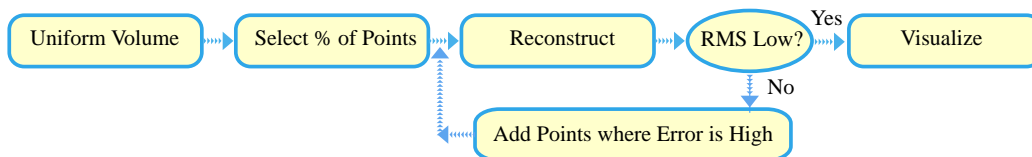


Figure 6.4: Diagram showing the proposed iterative point selection scheme.

In Table 6.1 we show results from our iterative point selection scheme. The tests were conducted for three different starting percentages and two different increment steps. For each starting percentage we measure the reconstruction errors when the number of points constitute 15%, 20% and 25% of the total points. In each case we check also the influence of the incremental step on the process (we set it either to 1% or 5%). From the results we understand that the best performance is achieved when the 1% incremental step is used. The results related to the starting percentage are very close. Taking into consideration that we have to reconstruct the dataset for each iteration step, the obvious selection would be the starting percentage which needs less iterations. Hence our iterative scheme gives best results when 15% is selected as starting percentage and in each iteration we increment the number of points by 1%. The results obtained from our iterative scheme demonstrate an up to 15% reduction of the RMS error when compared to the results shown in Chapter 3 (see Table 3.1). Computation times for each dataset are the same as in Tables 2.2 and 3.1, but multiplied by the number of iterations. In Figure 6.5 we show the behavior of the proposed iterative approach when the starting percentage is 5% and the incremental step is 1% and 5% respectively.

Table 6.1: Table showing the performance of the variational reconstruction when the non-uniform points are selected through our iterative scheme.

Starting Percentage	RMS _g					
	5%		10%		15%	
Dataset / Increment	1%	5%	1%	5%	1%	5%
Neghip (15%)	1.13	2.50	1.56	2.41	1.02	1.02
Neghip (20%)	0.99	1.31	1.04	1.42	0.99	1.01
Neghip (25%)	0.96	1.10	0.96	1.07	0.97	0.98
Engine (15%)	1.29	5.48	1.71	1.90	1.58	1.58
Engine (20%)	0.78	2.82	0.89	1.42	0.80	1.10
Engine (25%)	0.66	1.58	0.65	1.02	0.61	0.70
CT-Head (15%)	1.30	3.65	2.74	3.09	3.62	3.62
CT-Head (20%)	0.66	1.96	0.84	1.93	1.12	2.02
CT-Head (25%)	0.48	1.05	0.49	1.11	0.51	1.15

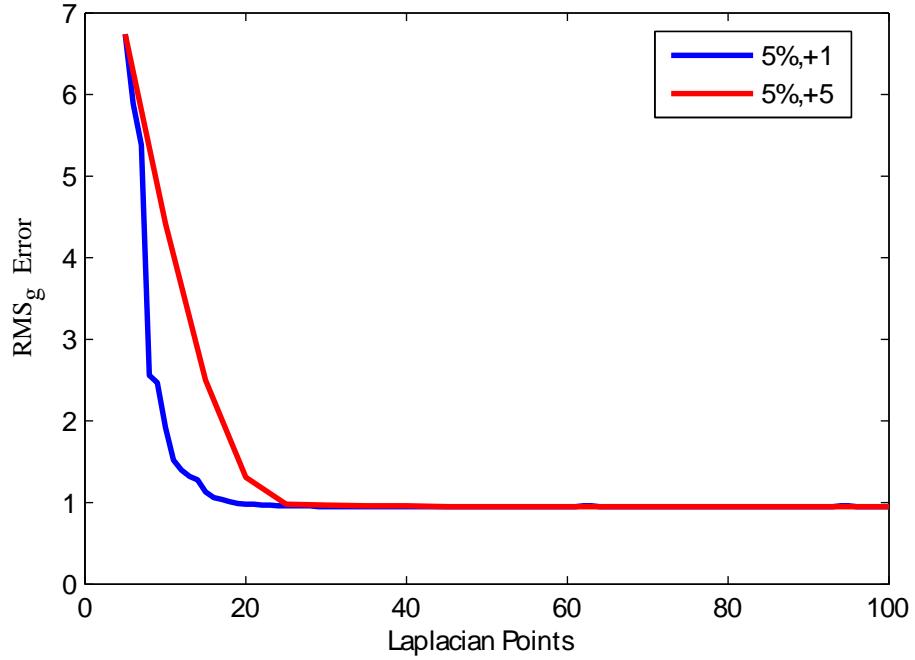
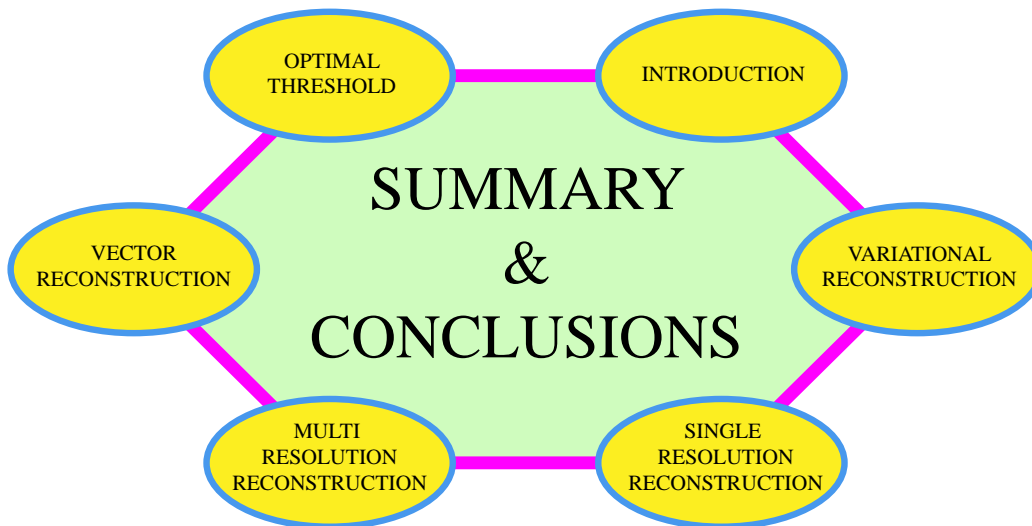


Figure 6.5: Relation of RMS_g to the percentage of Laplacian points for our iterative approach.

A scientific truth does not triumph by convincing its opponents and making them see the light, but rather because its opponents eventually die and a new generation grows up that is familiar with it.

Max Planck



In this work we presented a framework for reconstruction and visualization from non-uniform point sets on uniform grids using B-spline basis functions. We improve our reconstruction results by introducing a new regularization functional and a heuristic for selecting an optimal resolution. We introduce a new link between non-uniform representations and the interscale B-spline relation in a multi-resolution context. We show the performance and quality of our technique when compared to other competing techniques.

CHAPTER 7

SUMMARY AND CONCLUSIONS

Advances in technology are providing us every day with more and more complex data representations obtained either from real acquisition devices or simulations. Non-uniform data is a fast-spreading data type since it allows the representation of information with more samples where it is needed. Providing such a representation, which has no explicit internal structure, comes with a price. It is not trivial to be processed, analyzed and/or visualized.

In this thesis we present a general framework for reconstructing and visualizing non-uniform point sets. We approximate the data with a C^2 continuous function that uses B-splines as basis function.

We adopted a successful approach for the variational reconstruction of two-dimensional non-uniform data to the three-dimensional case. We proposed a block-based reconstruction, which does not suffer from inter-block discontinuities, in order to reconstruct 3D large datasets without being hampered by memory limits. As every variational approach is affected by the chosen regularization, we conducted several tests showing the impact of regularization on the reconstruction process. To improve the reconstruction results we introduced a Laplacian-like regularizer. This regularizer does not ensure rotational and scale invariance, but these features were traded for lower reconstruction errors and enhanced visual quality of the images rendered from the reconstructed data. Based on several tests, we proposed a logical heuristic for selecting a reconstruction resolution. Being dependent on the distribution of points across the volume and the variance of their values, this heuristic is closely correlated to the reconstruction resolution and to the reconstruction error.

Whereas selecting an optimal single resolution is advisable when the points are uniformly spread across the volume, multi-resolution comes into play for the cases where the distribution of points is highly variant across the volume. We propose a

multi-level pyramid style representation as a simple approach, but finally opt for an adaptive multi-resolution approach. The proposed scheme can represent the volume with multiple levels of details. Yet we suggest the usage of only two levels. The first level represents the coarse data details, while the second level refines the details only in the areas where the reconstruction error is high. Both levels are represented by C^2 continuous functions, and considering an appropriate spatial overlap we ensure the C^2 continuity of the multi-resolution function.

We make a first step in the reconstruction of vector data. We extend our framework to vector reconstruction by doing a component-wise reconstruction. We analyze our vector reconstruction scheme by applying to datasets obtained either from simulations or from the gradients of uniform datasets. Our component-based reconstruction gives low RMS errors. We will use such results in our future work as a starting point for developing more elaborated reconstruction techniques.

Finally, in our thesis we try to better understand the behavior of the variational approach with regard to the reconstruction of Laplacian datasets. By means of graphs and statistical analysis we arrive into the conclusion that best results, in terms of minimal reconstruction errors and good visual quality, can be achieved when $\lambda \in [0.2 - 0.3]$ and the percentage of points is in the interval $[15\% - 25\%]$.

After all what was stated above, the natural question would be: "Is everything said and done?". The straight answer is "NO!". There is no established theory that could suggest an optimal reconstruction resolution in terms of minimal reconstruction errors and good visual quality (no artifacts in the rendered images). With respect to the variational reconstruction there is no mathematical basis that would precisely state which regularization functional and what λ -value should be taken to achieve the best reconstruction for a specific data. With respect to visualization and multi-resolution there is no clear answer whether uniform or non-uniform grids are the best data representations in terms of efficiency of encoding and representation of information (signals). All these questions were offered alternative answers in this thesis. Until such answers do not become definitive, these questions will still remain the headings of our "Future Work".

BIBLIOGRAPHY

- [1] Bart Adams, Mark Pauly, Richard Keiser, and Leonidas J. Guibas. Adaptively sampled particle fluids. *ACM Transactions on Graphics*, pages 48–55, 2007.
- [2] Akram Aldroubi and Hans G. Feichtinger. Non-uniform sampling: Exact reconstruction from non-uniformly distributed weighted-averages. In *Proceedings of the international conference of computational harmonic analysis*, volume 1, pages 1–8, 2002.
- [3] Akram Aldroubi and Karlheinz Gröchenig. Beurling-Landau-type theorems for non-uniform sampling in shift invariant spline spaces. *Journal of Fourier Analysis and Applications*, 6:93–103, 2000.
- [4] Akram Aldroubi and Karlheinz Gröchenig. Nonuniform sampling and reconstruction in shift-invariant spaces. *SIAM Review*, 43(4):585–620, 2001.
- [5] Akram Aldroubi and Michael Unser. Families of multiresolution and wavelet spaces with optimal properties. *Numerical Functional Analysis and Optimization*, 14:417–446, 1993.
- [6] Mark Alexa, Johannes Behr, Daniel Cohen-Or, Shachar Fleishman, D. Levin, and Claudio T. Silva. Point set surfaces. In *Proceedings of IEEE Visualization*, pages 21–28, 2001.
- [7] Nina Amenta and Yong Kil. Defining point-set surfaces. In *Proceedings of SIGGRAPH*, pages 264–270, 2004.
- [8] Luca Amodè and Mohammed N. Benbourhim. A vector spline approximation. *Journal of Approximation Theory*, 67(1):51–79, 1991.

- [9] Muthuvel Arigovindan. *Variational Reconstruction of Vector and Scalar Images from Non-Uniform Samples*. PhD thesis, Ecole Polytechnique Federale de Lausanne, 2005.
- [10] Muthuvel Arigovindan, Michael Sühling, Patrick R. Hunziker, and Michael Unser. Variational image reconstruction from arbitrarily spaced samples: A fast multiresolution spline solution. In *IEEE Transactions on Image Processing*, volume 14, pages 450–460, 2005.
- [11] Muthuvel Arigovindan, Michael Sühling, Christian P. Jansen, Patrick R. Hunziker, and Michael Unser. Full motion and flow field recovery from echo Doppler data. *IEEE Transactions on Medical Imaging*, 26(1):31–45, 2007.
- [12] Matthew Aubury and Wayne Luk. Binomial filters. *Journal of VLSI Signal Processing*, 12:35–50, 1996.
- [13] Mohammed N. Benbourhim and Abderrahman Bouhamidi. Approximation of vectors fields by thin plate splines with tension. *Journal of Approximation Theory*, 136:198–229, 2005.
- [14] John Benedetto and Paulo J. S. G. Ferreira. *Modern Sampling Theory*. Birkhäuser, Boston, 2000.
- [15] Martin Bertram, Mark A. Duchaineau, Bernd Hamann, and Kenneth I. Joy. Generalized B-spline subdivision-surface wavelets for geometry compression. *IEEE Transactions on Visualization and Computer Graphics*, 10(3):326–338, 2004.
- [16] Martin Bertram, Xavier Tricoche, and Hans Hagen. Adaptive smooth scattered data approximation for large-scale terrain visualization. In *Proceedings of Symposium on Visualization*, pages 177–184, 2003.
- [17] Johanna Beyer, Markus Hadwiger, Torsten Möller, and Laura Fritz. Smooth mixed-resolution gpu volume rendering. In *Proceedings of IEEE/EG International Symposium on Volume and Point-Based Graphics*, pages 163–170, 2008.
- [18] Fred L. Bookstein. *Morphometric Tools for Landmark Data*. Cambridge University Press, 1991.
- [19] Stevan D. Bradley. Optimizing a scheme for run length encoding. In *Proceedings of the IEEE*, volume 57, pages 108–109, 1969.

- [20] William L. Briggs, Van Emden Henson, and Steve F. McCormick. *A Multigrid Tutorial*. SIAM, 2000.
- [21] Stefan Bruckner and M. Eduard Gröller. VolumeShop: An interactive system for direct volume illustration. In *Proceedings of IEEE Visualization*, pages 671–678, 2005.
- [22] Martin D. Buhmann. *Radial Basis Functions: Theory and Implementations*. Cambridge University Press, 2003.
- [23] Steven P. Callahan, Milan Ikits, Joao L. D. Comba, and Claudio T. Silva. Hardware-assisted visibility sorting for unstructured volume rendering. *IEEE Transactions on Visualization and Computer Graphics*, 11(3):285–295, 2005.
- [24] J. C. Carr, R. K. Beatson, J. B. Cherrie, T. J. Mitchell, W. R. Fright, B. C. McCallum, and T. R. Evans. Reconstruction and representation of 3D objects with radial basis functions. In *Proceedings of SIGGRAPH*, pages 67–76, 2001.
- [25] W. Chen, S. Itoh, and J. Shiki. Irregular sampling theorems for wavelet subspaces. In *Proceedings of IEEE International Symposium on Information Theory*, pages 244–, 1997.
- [26] Charles K. Chui and Ewald Quak. Wavelets on a bounded interval. *Numerical methods in approximation theory*, 105:53–75, 1992.
- [27] Paolo Cignoni, Claudio Montani, Enrico Puppo, and Roberto Scopigno. Multiresolution representation and visualization of volume data. *IEEE Transactions on Visualization and Computer Graphics*, 3(4):352–369, 1997.
- [28] Huong Quynh Dinh, Greg Turk, and Greg Slabaugh. Reconstructing surfaces by volumetric regularization using radial basis functions. *IEEE Transactions on Pattern Analysis and Machine Intelligence*, 24(10):1358–1371, 2002.
- [29] Fabrice Dodu and Christophe Rabut. Vector interpolation using radial-basis-like functions. *Computers and Mathematics with Applications*, 43:393–411, 2002.
- [30] Jean Duchon. Splines minimizing rotation-invariant semi-norms in Sobolev spaces. In *Multivariate Approx. Theory*, W. Schempp and K. Zeller, Eds. Birkhäuser-Verlag, pages 85–100, 1979.

- [31] Alireza Entezari, Tai Meng, Steven Bergner, and Torsten Möller. A granular three dimensional multiresolution transform. In *Proceedings of Joint Eurographics-IEEE VGTC Symposium on Visualization*, pages 267–274, 2006.
- [32] Gregory E. Fasshauer. Approximate moving least-squares approximation: A fast and accurate multivariate approximation method. In *Curve and Surface Fitting*, pages 139–148, 2002.
- [33] Hans G. Feichtinger, Karlheinz Gröchenig, and Thomas Strohmer. Efficient numerical methods in non-uniform sampling theory. *Numerische Mathematik*, 69:423–440, 1995.
- [34] Hans G. Feichtinger and Thomas Strohmer. Fast iterative reconstruction of band-limited images from non-uniform sampling values. In *Proceedings of the Computer Analysis of Images and Patterns*, pages 82–91, 1993.
- [35] Markus Fenn and Gabriele Steidl. *Geometric Properties for Incomplete data*, chapter Robust local approximation of scattered data, pages 317–334. Springer Netherlands, 2006.
- [36] Andrew Forsberg, Jian Chen, and David H. Laidlaw. Comparing 3D vector field visualization methods. In *Proceedings of IEEE Visualization*, 2009. In Press.
- [37] Richard Franke. Scattered data interpolation: Tests of some method. *Mathematics of Computation*, 38(157):181–200, 1982.
- [38] Richard Franke and Gregory M. Nielson. Scattered data interpolation and applications: A tutorial and survey. *Geometric Modelling, Methods and Applications*, Springer Verlag, pages 131–160, 1991.
- [39] Denis Grishin and Thomas Strohmer. Fast multi-dimensional scattered data approximation with Neumann boundary conditions. *Linear Algebra Applications*, 391:99–123, 2004.
- [40] Grant T. Gullberg, Michel Defrise, Vladimir Y. Panin, and Gengsheng L. Zeng. Efficient cardiac diffusion tensor mri by three-dimensional reconstruction of solenoidal tensor fields. *Magnetic Resonance Imaging*, 19:233–256, 2001.
- [41] Grant T. Gullberg, Dilip Roy, Gengsheng L. Zeng, Alexander I. Veress, and D. L. Parker. Tensor tomography. *IEEE Transactions on Nuclear Science*, 46(4):991–1000, 1999.

-
- [42] Jörg Haber, Frank Zeilfelder, Oleg Davydov, and Hans-Peter Seidel. Smooth approximation and rendering of large scattered datasets. In *Proceedings of IEEE Visualisation*, pages 341–347, 2001.
- [43] Wolfgang Hackbusch. *Iterative Solution of Large Sparse Systems of Equations*. Springer, 1993.
- [44] Wolfgang Hackbusch. *Multi-Grid Methods and Applications*. Springer, 2003.
- [45] Aijun He, Yuanqing Wang, Xinbao Ning, Ying Chen, and Qianli Ma. Vector interpolation method in three-dimensional reconstruction of tissue Doppler echocardiography. In *27th Annual International Conference of the Engineering in Medicine and Biology Society*, pages 3463–3466, 2005.
- [46] Akira Hirabayashi and Michael Unser. Consistent sampling and signal recovery. *IEEE Transactions on Signal Processing*, 55(8):4104–4115, August 2007.
- [47] Yun Jang, Ralf P. Botchen, Andreas Lauser, David S. Ebert, Kelly P. Gaither, and Thomas Ertl. Enhancing the interactive visualization of procedurally encoded multifield data with ellipsoidal basis functions. *Computer and Graphics Forum*, 25(3):587–596, 2006.
- [48] Yun Jang, Manfred Weiler, Matthias Hopf, Jingshu Huang, David S. Ebert, Kelly P. Gaither, and Thomas Ertl. Interactively visualizing procedurally encoded scalar fields. In *Proceedings of Joint EG-IEEE TCVG Symposium on Visualization*, pages 35–44, 2004.
- [49] Derek Juba and Amitabh Varshney. Modelling and rendering large volume data with gaussian radial basis functions. Technical report, University of Maryland, 2007.
- [50] Ralf Kähler. *Accelerated Volume Rendering on Structured Adaptive Meshes*. PhD thesis, Freien Universität Berlin, 2005.
- [51] Ralf Kähler, Tom Abel, and Hans-Christian Hege. Simultaneous gpu-assisted raycasting of unstructured point sets and volumetric grid data. In *Proceedings of IEEE/EG International Symposium on Volume Graphics*, pages 49–56, 2007.
- [52] Ralf Kähler, Mark Simon, and Hans-Christian Hege. Interactive volume rendering of large sparse data sets using adaptive mesh refinement hierarchies. *IEEE Transactions on Visualization and Computer Graphics*, 9(3):341–351, 2003.

- [53] Shankar Krishnan, Claudio T. Silva, and Bin Wei. A hardware-assisted visibility ordering algorithm with applications to volume rendering of unstructured grids. In *Proceedings of Joint EG-IEEE TCVG Symposium on Visualisation*, pages 27–34, 2001.
- [54] Ming-Jun Lai. Scattered data interpolation and approximation using bivariate c_1 piecewise cubic polynomials. *Computer Aided Geometry Design*, 13(1):81–88, 1996.
- [55] David H. Laidlaw, Robert M. Kirby, Cullen D. Jackson, J. Scott Davidson, Timothy S. Miller, Marco da Silva, William H. Warren, and Michael J. Tarr. Comparing 2D vector field visualization methods: A user study. *IEEE Transactions on Visualization and Computer Graphics*, 11(1):59–70, 2005.
- [56] Eric LaMar, Bernd Hamann, and Kenneth I. Joy. Multiresolution techniques for interactive texture-based volume visualization. In *Proceedings of IEEE Visualization*, pages 355–361, 1999.
- [57] Damiana Lazzaro and Laura B. Montefusco. Radial basis functions for the multivariate interpolation of large scattered data sets. *Journal of Computational and Applied Mathematics*, 140:150–165, 2002.
- [58] Christian Ledergerber, Gaël Guennebaud, Miriah D. Meyer, Moritz Bächer, and Hanspeter Pfister. Volume MLS ray casting. In *Proceedings of IEEE Visualization*, pages 1372–1379, 2008.
- [59] S. Lee, G. Wolberg, and S. Y. Shin. Scattered data interpolation with multilevel B-splines. In *IEEE Transactions on Visualization and Computer Graphics*, volume 3, pages 228–244, /1997.
- [60] Joshua Leven, Jason Corso, Jonathan Cohen, and Subodh Kumar. Interactive visualization of unstructured grids using hierarchical 3d textures. In *Proceedings of IEEE Symposium on Volume Visualization and Graphics*, pages 37–44, 2002.
- [61] Lars Linsen, Tran Van Long, Paul Rosenthal, and Stephan Rosswoeg. Surface extraction from multi-field particle volume data using multi-dimensional cluster visualization. In *IEEE Transactions on Visualization and Computer Graphics*, volume 14, pages 1483–1490, 2008.
- [62] Lars Linsen, Valerio Pascucci, Mark A. Duchaineau, Bernd Hamann, and Kenneth I. Joy. Wavelet-based multiresolution with n th-root-of-2 subdivision. *Journal on Computing, Springer-Verlag, Wien*, 71:47–54, 2004.

-
- [63] Youming Liu. Irregular sampling for spline wavelet subspaces. *IEEE Transactions on Information Theory*, 42(2):623–627, 1996.
- [64] Patric Ljung, Claes Lundström, and Anders Ynnerman. Multiresolution interblock interpolation in direct volume rendering. In *Proceedings of Joint Eurographics-IEEE VGTC Symposium of Visualization*, pages 259–266, 2006.
- [65] Michael Margaliot and Craig Gotsman. Piecewise-linear surface approximation from noisy scattered samples. In *Proceedings of IEEE Visualization*, pages 61–68, 1994.
- [66] Evgeny Margolis and Yonina C. Eldar. Nonuniform sampling of periodic bandlimited signals. *IEEE Transactions on Signal Processing*, 56(7):2728–2745, 2008.
- [67] Farokh A. Marvasti. Nonuniform sampling for multidimensional signals. In *Aachener Symposium für Signaltheorie*, pages 97–100, 1987.
- [68] Farokh A. Marvasti. *Non-uniform sampling: theory and practice*. Kluwer Academic/Plenum Publishers, 2000.
- [69] N. Max, P. Williams, C. Silva, and R. Cook. Volume rendering for curvilinear and unstructured grids. In *Proceedings of Computer Graphics International*, pages 210–217, 2003.
- [70] Miriah Meyer. *Dynamic Particles for adaptive sampling of implicit surfaces*. PhD thesis, School of Computing, University of Utah, 2009.
- [71] Miriah Meyer, Blake Nelson, Robert Kirby, and Ross Whitaker. Particle systems for efficient and accurate high-order finite element visualization. *IEEE Transactions on Visualization and Computer Graphics*, 13(5):1015–1026, 2007.
- [72] Miriah Meyer, Ross Whitaker, Robert M. Kirby, Christian Ledergerber, and Hanspeter Pfister. Particle-based sampling and meshing of surfaces in multi-material volumes. In *Proceedings of IEEE Visualisation*, volume 14, pages 1539–1546, 2008.
- [73] Charles A. Micchelli. Interpolation of scattered data: Distance matrices and conditionally positive definite functions. *Constructive Approximation*, 2(1):11–22, 1986.

- [74] Philipp Muigg, Markus Hadwiger, Helmut Doleisch, and Helwig Hauser. Scalable hybrid unstructured and structured grid raycasting. In *Proceedings of IEEE Visualization*, volume 13, pages 1592–1599, 2007.
- [75] Donald Myers, S. Iaco, D. Posa, and L. Cesare. Space-time radial basis functions. *Computers and Mathematics with Applications*, 43:539–549, 2002.
- [76] Gregory M. Nielson. Scattered data modeling. *IEEE Computer Graphics and Applications*, 13:60–70, 1993.
- [77] Gregory M. Nielson, Thomas A. Foley, Bernd Hamann, and David Lane. Visualizing and modeling scattered multivariate data. *IEEE Comput. Graph. Appl.*, 11(3):47–55, 1991.
- [78] Harry Nyquist. Certain topics in telegraph transmission theory. *Transactions of the American Institute of Electrical Engineers*, 47(2):617–644, 1928.
- [79] Yutaka Ohtake, Alexander Belyaev, Marc Alexa, Greg Turk, and Hans-Peter Seidel. Multi-level partition of unity implicits. *ACM Transactions on Graphics*, 22(3):463–470, 2003.
- [80] Yutaka Ohtake, Alexander G. Belyaev, and Hans-Peter Seidel. 3D scattered data approximation with adaptive compactly supported radial basis functions. In *International Conference on Shape Modeling and Applications*, pages 31–39, 2004.
- [81] Athanasios Papoulis. Generalized sampling expansion. *IEEE Transactions on Circuits and Systems*, 24(11):652–654, 1977.
- [82] Sung W. Park, Lars Linsen, Oliver Kreylos, and John D. Owens. Discrete Sibson interpolation. *IEEE Transactions on Visualization and Computer Graphics*, 12(2):243–253, 2006.
- [83] Arthur A. Petrosian and François G. Meyer. *Wavelets in Signal and Image Analysis: From Theory to Practice*. Springer, 2001.
- [84] Jerry L. Prince. Tomographic reconstruction of 3-d vector fields. In *Proceedings of International Conference on Acoustics, Speech, and Signal Processing*, volume 5, pages 483–486, 1993.
- [85] Sathish Ramani, Dimitri Van De Ville, Thierry Blu, and Michael Unser. Nonideal sampling and regularization theory. *IEEE Transactions on Signal Processing*, 56(4):1055–1070, 2008.

-
- [86] Kirk Riley, Yuyan Song, Martin Kraus, David S. Ebert, and Jason J. Levit. Visualization of structured nonuniform grids. *IEEE Computer Graphics and Applications*, 26(1):46–55, 2006.
- [87] Christian Rössl, Frank Zeilfelder, Günther Nürnberger, and Hans-Peter Seidel. Visualization of volume data with quadratic super splines. In *Proceedings of IEEE Visualisation*, pages 393–400, 2003.
- [88] Hanan Samet. *Foundations of Multidimensional and Metric Data Structures*. Morgan Kaufmann Publ. Inc., USA, 2005.
- [89] Ken D. Sauer and Jan P. Allebach. Iterative reconstruction of band-limited images from non-uniformly spaced samples. *IEEE Transactions on Circuits and Systems*, 34:1497–1506, 1987.
- [90] Vladimir Savchenko, Alexander A. Pasko, Oleg G. Okunev, and Toshiyasu L. Kunii. Function representation of solids reconstructed from scattered surface points and contours. *Computer Graphics Forum*, 14:181–188, 1995.
- [91] Philip Schlatter. Direct numerical simulation of laminar-turbulent transition in boundary layer subject to free-stream turbulence. Master’s thesis, Royal Institute of Technology, Stockholm, 2001.
- [92] John Schreiner, Carlos Scheidegger, and Claudio T. Silva. High-quality extraction of isosurfaces from regular and irregular grids. *IEEE Transactions on Visualization and Computer Graphics*, 12(5):1205–1212, 2006.
- [93] Claude E. Shannon. Communication in the presence of noise. *Proceedings of IRE*, 37:10–21, 1949.
- [94] Donald Shepard. A two-dimensional interpolation function for irregularly-spaced data. In *Proceedings of the 23rd ACM national conference*, pages 517–524, 1968.
- [95] P. Shirley and A. Tuchman. A polygonal approximation to direct volume rendering. In *Proceedings of the San Diego Workshop on Volume Visualisation*, pages 63–70, 1991.
- [96] Claudio T. Silva, Joseph S. Mitchell, and Arie Kaufman. Fast rendering of irregular grids. In *ACM/IEEE Volume Visualization Symposium*, pages 15–22, 1996.
- [97] Oliver G. Staadt. *Geometric Modeling for Scientific Visualization*, chapter Multiresolution surface and volume representation. Springer-Verlag, Heidelberg, Germany, 2003.

- [98] Eric J. Stollnitz, Anthony D. DeRose, and David H. Salesin. *Wavelets for Computer Graphics-Theory and Applications*. Morgan Kaufmann Publishers Inc., 1996.
- [99] Thomas Strohmer. *Efficient methods for digital signal and image reconstruction from non-uniform samples*. PhD thesis, Institute of Mathematics, Vienna University, 1993.
- [100] Thomas Strohmer. Computationally attractive reconstruction of bandlimited images from irregular samples. *IEEE Transactions on Image Processing*, 6(4):540–548, 1997.
- [101] Philippe Thévenaz, Thierry Blu, and Michael Unser. Image interpolation and resampling. In *Handbook of Medical Imaging, Processing and Analysis*, pages 393–420. Academic Press, 2000.
- [102] Philippe Thévenaz, Thierry Blu, and Michael Unser. Interpolation revisited. *IEEE Transactions on Medical Imaging*, 19(7):739–758, 2000.
- [103] Greg Turk and James F. O’Brien. Modelling with implicit surfaces that interpolate. *ACM Transactions on Graphics*, 21(4):855–873, 2002.
- [104] Michael Unser. Splines: A perfect fit for signal and image processing. *IEEE Signal Processing Magazine*, 16(6):22–38, 1999.
- [105] Michael Unser. Sampling—50 Years after Shannon. *Proceedings of the IEEE*, 88(4):569–587, 2000.
- [106] Michael Unser and Akram Aldroubi. A general sampling theory for nonideal acquisition devices. *IEEE Transactions on Signal Processing*, 42(11):2915–2925, 1994.
- [107] Michael Unser, Akram Aldroubi, and Murray Eden. B-Spline signal processing: Part I - Theory. *IEEE Transactions on Signal Processing*, 41(2):821–833, 1993.
- [108] Michael Unser, Akram Aldroubi, and Murray Eden. B-Spline signal processing: Part II - Efficient design and applications. *IEEE Transactions on Signal Processing*, 41(2):834–848, 1993.
- [109] Michael Unser and Josiane Zerubia. A generalized sampling theory without band-limiting constraints. *IEEE Transactions on Circuits and Systems—II: Analog and Digital Signal Processing*, 45(8):959–969, 1998.

-
- [110] Martin Vetterli and Jelena Kovacevic. *Wavelets and subband coding*. Prentice Hall, Englewood Cliffs, NJ, USA, 1995.
- [111] Erald Vuçini, Torsten Möller, and M. Eduard Gröller. Efficient reconstruction from non-uniform point sets. *The Visual Computer, Springer Berlin / Heidelberg*, 24(7-9):555–563, 2008.
- [112] Erald Vuçini, Torsten Möller, and M. Eduard Gröller. On visualization and reconstruction from non-uniform point sets using b-splines. In *Proceedings of Eurographics/IEEE-VGTC Symposium on Visualization*, volume 28, pages 1007–1014, 2009.
- [113] Chaoli Wang, Jinzhu Gao, Liya Li, and Han-Wei Shen. A multiresolution volume rendering framework for large-scale time-varying data visualization. In *Proceedings of Volume Graphics*, pages 11–19, 2005.
- [114] Chaoli Wang and Han-Wei Shen. LOD map - a visual interface for navigating multiresolution volume visualization. *IEEE Transactions on Visualization and Computer Graphics*, 12(5):1029–1036, 2006.
- [115] Manfred Weiler, Martin Kraus, Markus Merz, and Thomas Ertl. Hardware-based raycasting for tetrahedral meshes. In *Proceedings of IEEE Visualization*, pages 333–340, 2003.
- [116] Manfred Weiler, Rüdiger Westermann, Chuck Hansen, Kurt Zimmermann, and Thomas Ertl. Level-of-detail volume rendering via 3D textures. In *Proceedings of the IEEE Symposium on Volume Visualization*, pages 7–13, 2000.
- [117] Tomihisa Welsh and Klaus Mueller. A frequency-sensitive point hierarchy for images and volumes. In *Proceedings of IEEE Visualization*, pages 425–432, 2003.
- [118] Holger Wendland. *Scattered Data Approximation*. Cambridge University Press, 2005.
- [119] Roni Yagel, David M. Reed, Asish Law, Po-Wen Shin, and Naeem Shareef. Hardware assisted volume rendering of unstructured grids by incremental slicing. In *Proceedings of IEEE Symposium on Volume visualization*, pages 55–62, 1996.
- [120] A. Zakhor and G. Alvstad. Two-dimensional polynomial interpolation from nonuniform samples. *IEEE Transactions on Signal Processing*, 40(1):169–180, 1992.

- [121] Matthias Zwicker, Hanspeter Pfister, Jeroen van Baar, and Markus Gross. Ewa splatting. In *Proceedings of IEEE Visualisation*, pages 29–36, 2001.
- [122] Matthias Zwicker, Hanspeter Pfister, Jeroen van Baar, and Markus Gross. Surface splatting. In *Proceedings of ACM SIGGRAPH*, pages 371–378, 2001.

*Ask yourself, who am I to not want to be
brilliant, gorgeous, talented, and
fabulous?*

$\Sigma \Re \Delta$

Curriculum Vitae



Contact Information

Name	Erald Vucini
Address	Metternichgasse 7/10, 1030 Wien, Austria
Phone	+43 699 1024 0054
E-Mail	vucini@cg.tuwien.ac.at

Personal Details

Date of Birth	April 1 st , 1981
Place of Birth	Shkoder, Albania
Citizenship	Albanian
Gender	Male
Languages	Albanian (native), English (fluent), Italian (fluent), Turkish (fluent), French (intermediate), German (in- termediate)

Education

09/1987 - 06/1995	Primary School "Ismail Qemali", Shkoder, Albania
09/1995 - 06/1997	High School "28 Nentori", Shkoder, Albania
09/1997 - 06/1999	High School "Jordan Misja", Shkoder, Albania
09/1999 - 06/2000	Turkish Preparatory Class, Ankara, Turkey
10/2000 - 06/2004	Yildiz Technical University, Istanbul, Turkey B.Sc. in Computer Engineering (ranked 1 st)
10/2004 - 06/2006	Istanbul Technical University, Istanbul, Turkey M.Sc. in Computer Engineering
since 09/2006	Vienna University of Technology, Austria Doctoral studies (computer science). Working on the dissertation <i>On Visualization and Reconstruction from Non-uniform Point Sets</i> . Advisor: Prof. Eduard Gröller.

Honors and Scholarships

06/2009	2 nd Best Paper Award in Eurographics/IEEE-VGTC Symposium on Visualization, Berlin - Germany
06/2004	Undergraduated as First of Computer Engineering Department at Yildiz Technical University
06/1999	Yildiz Technical University Scholarship for undergraduate studies, offered to Albanian Students by the Turkish Government in cooperation with the Albanian Ministry of Education
06/1999	Gold Medal of Albania offered to one of the 4 best Students of Albania High Schools due to excellent results in school, National and International Olympiads
05/1999	Bronze Medal in the Balkan Mathematical Olympiad held in Ohrid, Macedonia (FYROM)
02/1999	First Prize (Gold Medal) in the Albanian National Mathematical Olympiad for High Schools
03/1998	First Prize (Gold Medal) in the Albanian National Mathematical Olympiad for High Schools

Professional Experience

- 07/2009 Universidad de las Ciencias Informaticas, Havana, Cuba
Lecturer. Teaching a Visualization Course at the 2nd Summer School at Universidad de las Ciencias Informáticas.
- 01/2008 - 04/2008 GRUVI Lab, Simon Fraser University, Canada
Research Exchange.
- since 09/2006 Vienna University of Technology, Austria
PhD Research assistant. Research and teaching at the Institute of Computer Graphics and Algorithms in the scope of the project Point-based Volume Graphics.
- 09/2005 - 06/2006 Computer Vision and Image Processing Lab, Istanbul Technical University, Turkey
M.Sc. Research Assistant. Multipurpose Robust Face Recognition Project: Research on detection and tracking of faces on video.
- 09/2004 - 06/2005 Garanti Bank, Technology Branch, Turkey
Software Developer and Researcher in Image Processing and Workflow Systems Developed algorithms for image and form processing. Developed a project for document identification used in the database systems of the Garanti Bank. Developed projects involving the implementation and improving of Optical Character Recognition Engines.
- 06/2002 - 08/2002 InfoSoft Group Tirana, Albania
Summer Intern. Server administration support of the InfoSoft Group clients. Managing with Linux and SQL Servers.

Scientific Activities

Talks

- | | |
|---------|--|
| 03/2006 | Face Recognition under Varying Illumination. Vienna University of Technology, Vienna, Austria |
| 03/2008 | Compressed Sensing: A General Overview. GRUVI Lab, Simon Fraser University, BC, Canada |
| 06/2008 | Efficient Reconstruction from Non-uniform Point Sets. CGI Conference, Istanbul, Turkey |
| 06/2009 | On Visualization and Reconstruction from Non-uniform Point Sets using B-splines. IEEE-VGTC Symposium on Visualization, Berlin, Germany |

Reviewing

- | | |
|-------------|---|
| Journals | Journal of Virtual Reality and Broadcasting, Neurocomputing Journal (Elsevier) |
| Conferences | Eurographics, EuroVis, Pacific Graphics, IEEE/EG International Symposium on Volume Graphics, International Conference on Computer Graphics Theory and Applications, Central European Seminar on Computer Graphics, Vision, Modeling, and Visualization Workshop |

Social Activities

- | | |
|-------------------|---|
| 02/2007 - 12/2007 | General Secretary of Rinia, Albanian Student and Youth Society in Austria |
| 12/2007 - 03/2009 | Head of Rinia, Albanian Student and Youth Society in Austria |
| 06/2007 - ... | Coordinator of AlbStudent, International Network of Albanian Student Associations |

Publications

Journal and Reviewed Conference Publications:

- Erald Vuçini, Muhittin Gökmen, and M. Eduard Gröller: Face Recognition under Varying Illumination. In Proceedings of WSCG, pages 57-64, 2007.
- Erald Vuçini, Torsten Möller, and M. Eduard Gröller: Efficient Reconstruction from Non-uniform Point Sets. *The Visual Computer*, Springer Berlin / Heidelberg, 24(7-9):555-563, 2008.
- Erald Vuçini, Torsten Möller, and M. Eduard Gröller: On Visualization and Reconstruction from Non-uniform Point Sets using B-splines. In Proceedings of Eurographics/ IEEE-VGTC Symposium on Visualization, volume 28, pages 1007-1014, 2009.

Other Publications:

- Jasper van de Gronde and Erald Vuçini: Compressed Sensing Overview. Technical Report, Vienna University of Technology, Institute of Computer Graphics and Algorithms, December 2008.
- Erald Vuçini and M. Eduard Gröller: Enhancing Visualization with Frequency-based Transfer Functions. Technical Report, Vienna University of Technology, Institute of Computer Graphics and Algorithms, May 2009.